UNIVERSITY OF HELSINKI REPORT SERIES IN PHYSICS

N:o D266 (2019)

MAGNETIC STRUCTURE AND GEOEFFECTIVENESS OF CORONAL MASS EJECTIONS

ERIKA PALMERIO

Department of Physics
Faculty of Science
University of Helsinki
Helsinki, Finland

ACADEMIC DISSERTATION

To be presented, with the permission of the Faculty of Science of the University of Helsinki, for public criticism in auditorium D101 of the Department of Physics (Physicum), Gustaf Hällströmin katu 2a, on September 20th, 2019, at 12 o'clock noon.

Helsinki 2019

Author's Address: Department of Physics
P.O. Box 64
FI-00014 University of Helsinki
erika.palmerio@helsinki.fi

Supervisor: Assoc. Prof. Emilia K. J. Kilpua
Department of Physics
University of Helsinki

Pre-examiners: Prof. Anita T. Aikio
Department of Physics
University of Oulu

Prof. Mathew J. Owens
Department of Meteorology
University of Reading

Opponent: Dr. Jon A. Linker
Predictive Science Inc.

ISBN (printed version) 978-951-51-2803-4
ISSN 0356-0961
Helsinki 2019
Helsinki University Printing House Unigrafia Oy

ISBN (PDF version) 978-951-51-2804-1
http://ethesis.helsinki.fi
Helsinki 2019
Electronic Publications @ University of Helsinki

Kuu saa valtansa Auringolta
Ja vaikka näyttääkin hohtavalta
Ei valoaan se yksin jaa
Saa vallan Auringolta
Auringolta jolta
Kuu vain lainaa valoaan

Marko Annala [Mokoma]

Erika Palmerio
University of Helsinki, 2019

Abstract

The Sun, besides being fundamental for life on Earth, is also characterised by intense activity and magnetism. Such activity manifests often in the form of eruptions, that can either be confined to the solar atmosphere or consist of large amounts of plasma and magnetic flux that are ejected into interplanetary space. The latter phenomena are known as coronal mass ejections (CMEs). CMEs travelling through interplanetary space may impact Earth and harm the performance and reliability of space- and ground-based technological systems, such as satellites in orbit, high-voltage power and natural gas pipeline networks, and systems utilising navigation and positioning applications. Moreover, the increased radiation that follows a CME eruption can endanger the health of astronauts involved in space missions. The effects of solar activity on Earth are called collectively "space weather". The ability of a CME to drive space weather effects on Earth (or "geoeffectiveness") depends on its internal magnetic structure, morphology, and speed. The magnetic structure of a CME is often described with a flux rope morphology, that is a helical magnetic tube whose magnetic field can be divided into two main components: the axial field, which runs through the centre of the tube, and the helical field, which wraps around the tube.

In this thesis, the magnetic structure of CMEs and their geoeffectiveness at 1 AU are investigated using a combination of observational and modelling techniques. The magnetic structure of flux ropes at the time of eruption can be inferred from multiwavelength remote-sensing observations of the CME source region, by taking into account features as coronal loops, filaments, flare ribbons, and photospheric structures. However, the results of the analysis show that the magnetic structure of such flux ropes may differ significantly when measured at 1 AU, i.e. around Earth's orbit. This is because CMEs can experience dramatic evolution after lifting off from the Sun, e.g. through deflections, rotations, and deformations. The results presented in this thesis highlight that CME evolution is an important factor to take into account in numerical models and, more generally, in space weather forecasting. Furthermore, the turbulent sheath regions that often travel ahead of CMEs may contain geoeffective components. Another aspect that contributes to making CME forecasting a challenging task is represented by those CMEs whose impact is less "obvious," e.g., because they are not entirely Earth-directed or because their signatures are unclear in remote-sensing data. During periods of significant solar activity there can be multiple CMEs launched from the same or nearby source regions.

This thesis utilises recent multi-instrument observations from different vantage points to anal-

yse periods of successive CME eruptions and their possible interactions in the corona and inner heliosphere. Magnetohydrodynamic modelling of CME propagation is also used, especially for problematic CMEs and multi-eruption periods, to provide a global heliospheric context necessary to interpret the multi-spacecraft observations. This thesis thus contributes to the improvement of our current understanding of CME evolution and space weather forecasting. Its results can be used as inputs, validation, and refinement for space weather forecasting tools and their modelling results. Finally, its comprehensive Sun–to–1 AU approach to analyse periods of enhanced eruptive activity and the subsequent heliospheric evolution of multiple CME events emphasises the importance of combining observations from multiple vantage points and heliospheric modelling for making progress in space weather forecasting.

Keywords: Solar Physics, Space Physics, Coronal Mass Ejections, Solar Wind, Space Weather

Contents

Preface

The years that led to this thesis have been one hell of a ride, filled with exciting science, dramas, many many flights, and so much more. Initially, I was not planning to dedicate my career to our Sun, but a series of events led me here (more on that in the next paragraph), and I could not be happier of where I am now. Interestingly enough, right after obtaining my MSc diploma and just before starting my PhD studies, I had the privilege to witness one of the strongest geomagnetic storms of the last decade, now known in the space weather circles as *the St. Patrick's storm* (you can see a picture of the related breathtaking aurora somewhere in Chapter 2 of this thesis). Being under that bright green sky in that cold but magical night (yes, I was exactly under that sky right in the picture!) was the final confirmation for me that I had chosen the right path, and that space physics was truly what I wanted to research.

First of all, I wish to thank Hannu Koskinen and Rami Vainio for suggesting me taking a few courses in space physics during my Master's studies. I did not know at that time how spectacular our solar system is, and it is thanks to them that I got introduced to the magical wonders of our Sun. I am of course deeply grateful to my MSc and PhD supervisor, Emilia Kilpua, for welcoming me into the team and for offering me such a challenging yet inspiring PhD project after my Master's graduation.

I am grateful to my pre-examiners, Anita Aikio and Mathew Owens, for taking the time to read and evaluate this thesis. I would also like to thank in advance Jon Linker, who has accepted to travel to Finland (hopefully the weather will still be nice in September!) to be the opponent of this thesis.

A huge amount of thanks goes to our crazy group of space people ("the farting Sun worshippers") who have made these years enjoyable and awesome, including my office mates and bros Matti Ala-Lahti and Simon Good, our radio queen Diana Morosan, the ultra-british Daniel Price, and our pastry chef Maxime Grandin. The atmosphere in the space physics group has always been so friendly and relaxed, and I could not have asked for a better environment to work in.

Moving now away from our solar system and going farther out to distant galaxies and black holes, I thank the club of the present and future "postdoctoral students" (yes, we all knew this was coming) for all the fun and support throughout the years: Antti Rantala, Natalia Lahén, and Pauli Pihajoki. A huge thanks to my dear *gatta*

Elisabetta Micelotta, who spent an uncountable number of cigarette breaks with me (sorry for the passive smoke!) and who has been a true friend in so many occasions.

As I said, these years have been filled with numerous travels, so I want to thank all the great researchers around the world who have hosted me and/or made my visits memorable. To name a few, Lucie Green and Alex James from UCL/MSSL; Luciano Rodriguez, Marilena Mierla, Andrei Zhukov, and Jasmina Magdalenić from ROB; Camilla Scolini and Stefaan Poedts from KU Leuven; Neel Savani, Christina Kay, Barbara Thompson, and Raphael Attie from NASA/Goddard. Special mention to David Barnes who has never hosted me at RAL but who has been (and I hope will continue to be!) the best conference mate one could wish for. I also wish to thank Christian Möstl and Volker Bothmer for the fruitful collaborations over these years.

A huge thanks to Nariaki Nitta and Tamitha Mulligan for inviting me to be part of the legendary "stealthy" ISSI team, and of course a huge shoutout to all the team members for the great fun and the interesting science: Ian Richardson, Jens Pomoell, Ben Lynch, Steph Yardley, Paolo Pagano, Nandita Srivastava, Dana Talpeanu, Jennifer O'Kane, Alexis Rouillard, and again Emilia, Luciano, Marilena, and Andrei.

Scicomm has been a big part of the final half of my PhD studies, so I would like to thank the awesome young scientists that are part of The Science Basement and in particular Ekaterina Baibuz, Stephany Mazon, Lea Urpa, Chiara Facciotto, and Katja Kaurinkoski.

Thanks to my family for constantly supporting me and cheering for me even if I am so far from them. *Grazie madre & padre (& fratello)* ♥

A very special and huge thanks filled with hugs and unicorns to Paul Menczel, who has always been there for me. Remember, wherever in the world we may be in the future, we will always be best friends (but we will need to travel to Finland regularly to enjoy some Fafa's pitas)!

Last but not least, lucky Ben gets a double thanks (earlier up as a colleague, now as a partner). Thank you so much for putting up with my shenanigans and for pushing me to believe in myself. I am truly excited to start the next chapter of my life with you.

Erika Palmerio
Helsinki, August 2019

List of Acronyms

ACE	Advanced Composition Explorer
AIA	Atmospheric Imaging Assembly
CIR	Corotating interaction region
CME	Coronal Mass Ejection
DSCOVR	Deep Space Climate Observatory
Dst	Disturbance storm time
ESP	Energetic storm particle
EUHFORIA	EUropean Heliospheric FORecasting Information Asset
EUV	Extreme UltraViolet
Hα	Hydrogen-alpha
HI	Heliospheric Imager
HMI	Helioseismic and Magnetic Imager
ICME	Interplanetary Coronal Mass Ejection
IMF	Interplanetary Magnetic Field
LASCO	Large Angle and Spectrometric COronagraph
LOS	Line of sight
MDI	Michelson Doppler Imager
MESSENGER	MErcury Surface, Space ENvironment, GEochemistry, and Ranging
MHD	Magnetohydrodynamic(s)
PEA	Post-eruption arcade
PIL	Polarity inversion line
PSP	Parker Solar Probe
SDO	Solar Dynamics Observatory
SECCHI	Sun Earth Connection Coronal and Heliospheric Investigation
SEP	Solar energetic particle
SIR	Stream interaction region
SMEI	Solar Mass Ejection Imager
SOHO	SOlar and Heliospheric Observatory
SolO	Solar Orbiter
(S)SSE	(Stereoscopic) Self-Similar Expansion
STEREO	Solar TErrestrial RElations Observatory
VEX	Venus EXpress
XRT	X-Ray Telescope

List of Publications

This thesis consists of an introductory review, followed by five research articles. They have not been included in prior theses and are published in international peer-reviewed journals. The articles will be mentioned throughout the thesis according to their roman numerals.

I **Palmerio, E.**, Kilpua, E. K. J., and Savani, N. P.: Planar magnetic structures in coronal mass ejection-driven sheath regions, *Annales Geophysicae*, 34, 313–322, doi:10.5194/angeo-34-313-2016, 2016.

II **Palmerio, E.**, Kilpua, E. K. J., James A. W., Green, L. M., Pomoell, J., Isavnin, A., and Valori, G.: Determining the intrinsic CME flux rope type using remote-sensing solar disk observations, *Solar Physics*, 292:39, doi:10.1007/s11207-017-1063-x, 2017.

III **Palmerio, E.**, Kilpua, E. K. J., Möstl, C., Bothmer, V., James, A. W., Green, L. M., Isavnin, A., Davies, J. A., and Harrison, R. A.: Coronal magnetic structure of earthbound CMEs and in situ comparison, *Space Weather*, 16, 442–460, doi:10.1002/2017SW001767, 2018.

IV **Palmerio, E.**, Scolini, C., Barnes, D., Magdalenić, J., West, M. J., Zhukov, A. N., Rodriguez, L., Mierla, M., Good, S. W., Morosan, D. E., Kilpua, E. K. J., Pomoell, J., and Poedts, S.: Multipoint study of successive coronal mass ejections driving moderate disturbances at 1 au, *The Astrophysical Journal*, 878:37, doi:10.3847/1538-4357/ab1850, 2019.

V Kilpua, E. K. J., Good, S. W., **Palmerio, E.**, Asvestari, E., Lumme, E., Ala-Lahti, M., Kalliokoski, M. M. H., Morosan, D. E., Pomoell, J., Price, D. J., Magdalenić, J., Poedts, S., and Futaana, Y.: Multipoint observations of the June 2012 interacting interplanetary flux ropes, *Frontiers in Astronomy and Space Sciences*, 6:50, doi:10.3389/fspas.2019.00050, 2019.

1 Introduction

♪ *Here comes the Sun* – The Beatles

Since the beginning of the *Space Age* with the launch of the *Sputnik 1* satellite in 1957, modern society has become increasingly dependent on space-based technology. Nowadays, space technology includes, but is not limited to, satellites dedicated to communication, navigation, Earth observation, space exploration, and national security. All these systems, however, are vulnerable to *space weather* effects. The term space weather refers to the physical processes driven by solar activity that manifest as disturbances in Earth's environment. It came into popular use in the 1990s, but its origins can be traced back to the middle to late 1800s (Cade and Chan-Park, 2015). Space weather phenomena can damage and harm the performance of satellites in Earth orbit and spacecraft in interplanetary space, but such effects are not limited to space-based technology. A notorious example is the geomagnetic storm of 1859 (Carrington, 1859; Hodgson, 1859), known as the *Carrington Event*, which took place well before the Space Age. The Carrington Event was a storm of such great magnitude that it caused the failure of telegraph systems across Europe and North America and bright auroral displays down to low latitudes (e.g., Green and Boardsen, 2006; Moreno Cárdenas et al., 2016; González-Esparza and Cuevas-Cardona, 2018; Hayakawa et al., 2018). More recent prominent geomagnetic storms include the storm of 1972 (Knipp et al., 2018), which caused electric- and communication-grid disturbances in North America and the simultaneous detonation of dozens of sea mines in North Vietnam, the storm of 1989 (Allen et al., 1989) that caused a massive power-grid outage in Québec, the "*Bastille Day*" storm of 2000 (Andrews, 2001; Raeder et al., 2001; Török et al., 2018) that caused electrical breakdowns and satellite malfunctions, and the "*Halloween*" storms of 2003 (Lopez et al., 2004; Manchester et al., 2008; Cid et al., 2015) that disrupted space-based navigation systems. The increased radiation during periods of enhanced solar activity may also endanger the health of long-haul aircraft crews and, in particular, of astronauts participating in space missions. Whilst this holds today for astronauts on board the *International Space Station* in low Earth orbit, the major concerns are related to future manned missions to the Moon or Mars (e.g., Musk, 2017, 2018), where the crews would be exposed to an harsh radiation environment outside of Earth's protective atmosphere and magnetosphere for an extended amount of time. In light of these issues,

it is clear that space weather can affect human life and technology in multiple ways and that, as such, it must be predicted accurately and well in advance in order to mitigate its effects.

In order to be able to forecast space weather effects efficiently and with sufficient lead times, it is important to understand their origin and evolution in the framework of the Sun–Earth system. One of the major drivers of space weather effects are known as *coronal mass ejections* (CMEs, e.g., Webb and Howard, 2012). CMEs are spectacular, massive blasts of plasma and magnetic fields that are regularly ejected from the Sun into interplanetary space. When reaching Earth's orbit, CMEs can cause magnetic reconnection at the dayside magnetopause (i.e., the outer boundary of Earth's magnetosphere), allowing access of energy, momentum, and plasma in the magnetosphere, enhancement of the ionospheric electric currents, and precipitation of energetic particles in the ionosphere (e.g., Pulkkinen, 2007). The ability of CMEs to cause geomagnetic storms at Earth is known as *geoeffectiveness*. In order for this to happen, it is necessary that a CME's magnetic field is oppositely directed to Earth's magnetic field. Since Earth's quasi-dipolar field is roughly perpendicular to the ecliptic plane and directed towards the North in the ecliptic plane, the most geoeffective solar wind structures are the ones containing southward magnetic field. Other solar wind parameters that are important for the geoeffectiveness of a CME are speed and dynamic pressure (e.g., Crooker, 2000; Boudouridis et al., 2005).

CMEs are known to erupt from the solar atmosphere as helical magnetic structures called *flux ropes* (e.g., Forbes, 2000; Chen, 2011; Green et al., 2018), which are bundles of magnetic field lines that wind about a common central axis. The evolution of CME flux ropes as they propagate through the corona and interplanetary space is a critical aspect that will determine their ability to trigger space weather disturbances at Earth; CMEs can experience dramatic evolution through deflections and/or rotations (e.g., Vourlidas et al., 2011; Isavnin et al., 2013; Kay et al., 2015; Manchester et al., 2017) or through interaction with solar wind streams and other CMEs (e.g., Lugaz et al., 2012, 2017). Furthermore, CMEs often drive shock waves ahead of them in the corona and interplanetary space. The *sheath region* that develops between the shock and the CME leading edge is composed of compressed and turbulent plasma (e.g., Kilpua et al., 2017), and is capable of causing significant geomagnetic disturbances regardless of the magnetic structure of their corresponding CMEs (e.g., Tsurutani et al., 1988; Gonzalez et al., 1999, 2011; Huttunen et al., 2002; Huttunen and Koskinen, 2004; Lugaz et al.,

2016). All these aspects make forecasting space weather disturbances related to CMEs a particularly challenging task. At present, the space weather effects of CMEs cannot be reliably predicted until they reach the Lagrange L1 point, which is located along the Sun–Earth line (about 1.5 million kilometres ahead of Earth) and where the solar wind monitoring spacecraft are operating (such as the *Advanced Composition Explorer* or ACE, Stone et al., 1998; *Wind*, Ogilvie and Desch, 1997; and the *Deep Space Climate Observatory* or DSCOVR). The L1 point, however, is so close to Earth with respect to the Sun–Earth distance that in-situ measurements made from there can provide a warning time of 30–60 minutes only.

This thesis is centred on the magnetic structure and geoeffectiveness of CMEs and CME-related structures, and on how the geoeffective parameters of solar eruptions can be studied and monitored from the Sun throughout interplanetary propagation. In particular, the major issues that this thesis addresses are:

- How can the magnetic structure of CMEs at the time of their eruption be estimated from remote-sensing observations? (Paper II and Paper III)
- How does the magnetic structure of CMEs change during interplanetary propagation? (Paper III and Paper V)
- How do CME-driven sheath regions and their substructures cause disturbances at Earth's orbit? (Paper I and Paper IV)
- Can CME and sheath evolution be captured through multipoint observations coupled with heliospheric modelling? (Paper IV and Paper V)

This thesis is composed of two main sections, namely an introductory part and a collection of five original research articles referred to as Papers I–V. The introductory part is organised as follows. Chapter 2 provides an overview of the structure of the Sun and solar activity, with an emphasis on space weather drivers and their effects on the near-Earth space environment. Chapter 3 reviews general CME properties and describes how CMEs can be observed from their pre-eruptive state until their in-situ detection in interplanetary space. Chapter 4 assesses the current status of CME forecasting and addresses the challenges in predicting CME-driven disturbances at Earth. Chapter 5 provides some concluding remarks, followed by a brief review of the future breakthroughs expected in understanding and forecasting CMEs. Finally, Chapter 6 summarises the scientific articles included in this thesis and the author's contribution in the preparation of each.

2 The Sun and space weather

♪ *Waiting for the Sun* – The Doors

Space weather depends directly on solar magnetic activity. The Sun is a very dynamic star, with changes in its magnetism that evolve on time scales that range from minutes up to billions of years. The Sun's magnetic field is generated by electrical currents in its interior acting as a magnetic dynamo and is shaped by a multitude of processes. In order to understand how the Sun drives space weather, it is important to know how the solar magnetic field originates, how it is shaped, and how it behaves. In order to understand how CMEs erupt from the Sun and how their magnetic field is structured, it is important to understand how features on the Sun are linked to the instrinsic structure of CMEs. Accordingly, this chapter will first focus on solar magnetism and on features visible on the solar surface and through the different layers of its atmosphere. Finally, the major space weather-driving phenomena and their effects on Earth are discussed.

2.1 Solar magnetism and activity

Before discussing how the Sun's magnetic field shapes and modulates solar activity, it is important to review how the Sun is structured. Figure 2.1 shows how the solar interior and atmosphere can be divided into zones or layers.

The solar interior is composed of three layers, namely the *core*, the *radiative zone*, and the *convective zone* (e.g., see review by Ambastha, 2010). The Sun's energy is produced in the hot, central core through nuclear reactions. The core's radius equals approximately one-quarter of the solar radius, and its temperature is around 15×10^6 K. The processes through which the solar energy is transported from the core up to the outer layers are mainly two, from which the two remaining layers of the solar interior take their names. The radiative zone is a spherical shell that extends about three-quarters of the way to the surface and where energy is carried outwards by radiation. In this zone, however, the plasma is so dense that photons are continuously absorbed and re-emitted in random directions, taking about two hundred thousand years to reach the outer boundary of the radiative zone, called the *tachocline* (Mitalas and Sills, 1992). This is where energy transport becomes convective, since the plasma in

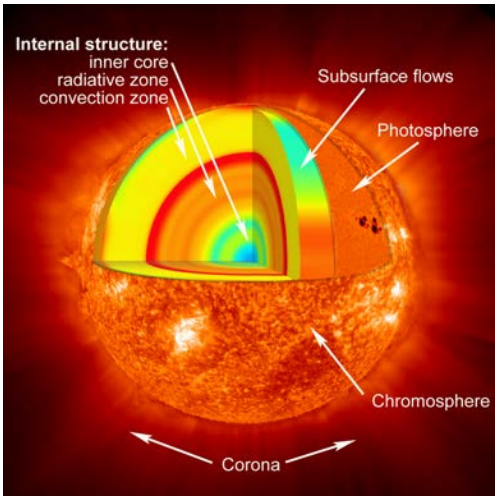

Figure 2.1: The layers of the Sun. Image credit: NASA.

the convection zone is too cool and opaque to allow radiation to go through. In this layer, in fact, the Sun's temperature drops to about 2×10^6 K. Since convective motions allow photons to "ride" hot blobs of plasma through the solar interior, it takes them only a couple of days to reach the surface of the convection zone.

After exiting the convection zone, photons encounter the solar atmosphere, which is itself composed of several layers. The *photosphere* is considered as the surface of the Sun and it is the deepest layer that can be observed directly. In this layer, the temperature has decreased to about 5×10^3 K and the densities are so low that photons can finally escape, allowing observations of the photosphere in white light. Furthermore, the photosphere is characterised by a continuously "boiling" appearance, being composed of convection cells, called granules, that have averages sizes of 1000–2000 kilometres and lifespans of the order of tens of minutes. Above the photosphere lies the *chromosphere*, which can be detected in red hydrogen-alpha (Hα) light. The chromosphere is the first solar layer where the temperature increases with increasing height, from about 4×10^3 to 8×10^3 K. On top of the chromosphere there is a very thin layer called the *transition region*, where the temperature rises abruptly from about 8×10^3 to about 500×10^3 K. Finally, the outermost layer of the Sun is known as the *corona*, which extends for millions of kilometres into outer space. Since the corona is much fainter than the bright solar disc, it can be observed only through an eclipse, which can be

either "real" or "fake" (i.e., created through a coronagraph, see Section 2.1.4). The temperature of the corona reaches up to a few million Kelvins, which means that it is several orders of magnitude hotter than the solar surface. Why the solar atmosphere is so hot is still in large part an unresolved question, and this mystery is now known as the *coronal heating problem* (e.g., Parnell and De Moortel, 2012; Klimchuk, 2015; Downs et al., 2016).

2.1.1 The Sun's magnetic field

The Sun's magnetic field is generated in its interior by a process, called the *solar dynamo*, that finds its energy sources from the non-uniform rotation and the heat produced in the core. The basic idea of the solar dynamo was first introduced by Larmor (1919). According to his theory, the solar magnetic field is maintained by the motion of that electrically conducting ionised plasma that is found in the convection zone. The motion of the fluid induces electric currents and, as a consequence, a self-sustaining magnetic field. If the Sun was rotating as a rigid body, this magnetic field would simply come out of the north pole, curl out through space, and re-enter at the south pole. This is what happens in the case of a bar magnet or Earth, but for the Sun the situation is considerably more complicated.

The principles of the current understanding of the solar dynamo theory will be briefly described below. Comprehensive reviews can be found in Charbonneau (2010, 2014). The Sun spins at different speeds at different latitudes, phenomenon that is known as *differential rotation*; at the equator one rotation takes about 25 days, whilst the poles complete one rotation in about 33 days (Thompson et al., 1996). The reason for this behaviour is that the Sun is not a solid object, but can instead be considered as a fluid composed of hot and dense plasma. Let us consider the initial configuration of a magnetic field with field lines that run parallel to the solar meridians, similarly to Earth's intrinsic magnetic field. This configuration is known as *poloidal* magnetic field. Because of differential rotation, the plasma in the tachocline drags the magnetic field with the flow, distorting and stretching it about the equator (where it rotates faster). Rotation after rotation, the magnetic field wraps around the Sun more and more until it reaches a configuration known as *toroidal* magnetic field, where the field lines are aligned with the solar parallels. This process also amplifies the magnetic field every time a field line wraps around the Sun more than once. The toroidal field keeps building

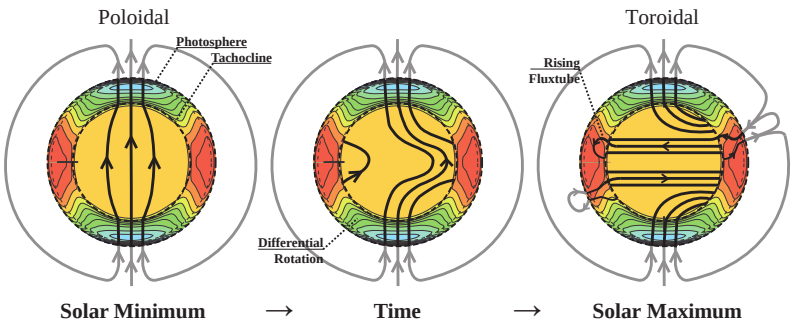

Figure 2.2: Schematic of the solar dynamo, with the magnetic field evolving from poloidal and dipolar to toroidal and multipolar through the solar cycle. Adapted from Higgins (2012), doi:10.6084/m9.figshare.102094.v1.

up until it reaches an unstable state and buoyant forces begin to act, letting magnetic loops float towards the solar surface (see Section 2.1.2). Every time a new loop emerges, its trailing part is slightly closer to the nearby solar pole because of the twisting Coriolis force. The trailing part of the tube, however, has an opposite magnetic polarity than the pole, meaning that when its magnetic field diffuses through the photosphere the pole receives a certain amount of field of the opposite polarity. Eventually, the buildup of magnetic field of opposite polarity at each pole leads to a global reconfiguration of the Sun's magnetic field, which returns to a poloidal state but with a reversed polarity. This is the famous *solar cycle*, sketched in Figure 2.2, which has a duration of about 11 years (Schwabe, 1843; Hathaway, 2015). The purely poloidal state is known as *solar minimum*, where the solar magnetic field is dipolar, whilst the purely toroidal state is called *solar maximum*, where the field becomes multipolar because of the amount of emerging flux loops. The solar cycle has crucial implications on solar activity, as will be discussed in the following sections.

2.1.2 Photospheric features

When unstable toroidal flux tubes float towards the solar surface (see Section 2.1.1), the magnetic field is carried up with the plasma and stretched to form a shape that resembles the Greek letter Ω. When these Ω-shaped loops rise, the first surface they cross is the photosphere. This is how *active regions* form on the Sun, i.e., they are

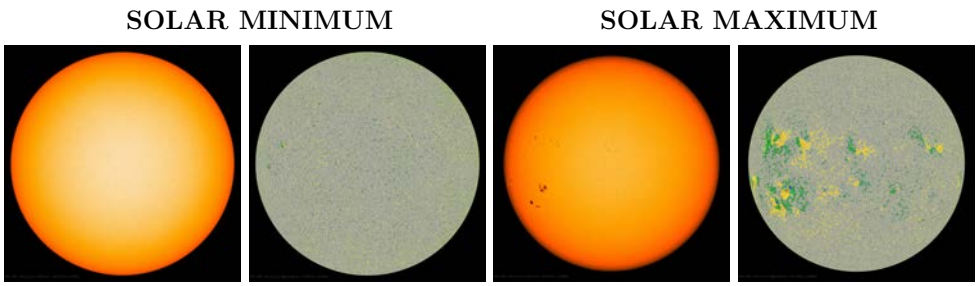

Figure 2.3: The photosphere during solar minimum (in January 2019) versus the photosphere during solar maximum (in July 2014). For each of the two periods, both the white-light photosphere and the corresponding magnetogram are shown. In the magnetograms, green/blue areas indicate positive magnetic field (directed anti-Sunwards) and yellow/red areas indicate negative magnetic field (directed Sunwards). Image credit: NASA—SDO/HMI.

regions where strong magnetic fields are concentrated. When observed in white light, footpoints of the strongest Ω flux systems may appear on the photosphere as dark spots known as *sunspots* (their temperatures are lower than the ambient photosphere, as the strong magnetic field inhibits upward motion of the hot plasma).

Photospheric magnetic fields are generally presented as maps of the magnetic field known as *magnetograms* that are measured through space- or ground-based magnetographs. Magnetographs measure either the line-of-sight (LOS) magnetic field only (e.g., with the *Michelson Doppler Imager* or MDI, Scherrer et al., 1995, onboard the *Solar and Heliospheric Observatory* or SOHO, Domingo et al., 1995) or the full 3D magnetic field components (e.g., with the *Helioseismic and Magnetic Imager* or HMI, Scherrer et al., 2012, onboard the *Solar Dynamics Observatory* or SDO, Pesnell et al., 2012), in which case the magnetogram is known as a vector magnetogram. Measurement techniques exploit the Zeeman effect, referring to the splitting of the energy levels of an atom in an external magnetic field (e.g., Lagg et al., 2017).

Since active regions and sunspots are generated by the emergence of buoyant Ω-loops, the photosphere looks dramatically different at solar minimum versus solar maximum, as shown in Figure 2.3. The lifetime of an active region (and of its related sunspots) ranges from a few hours to several months, depending on its size and magnetic flux content, and is characterised by a relatively fast emergence phase, when new magnetic

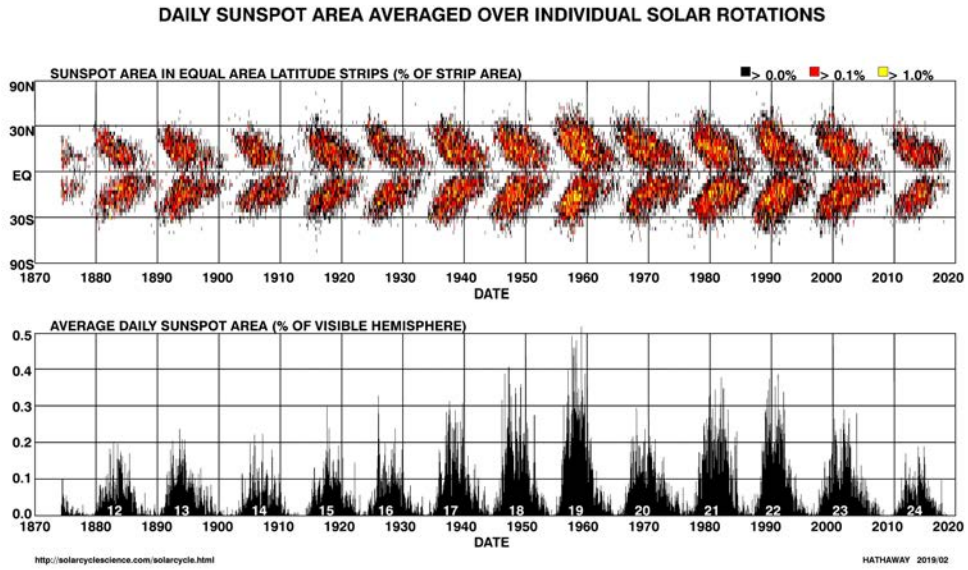

Figure 2.4: Top panel: The butterfly diagram, showing how the latitude of sunspots evolves with the solar cycle. Bottom panel: the average daily sunspot area through solar cycles 12–24. Image credit: solarcyclescience.com.

fields can be seen forming in the photosphere, and a long decay phase, when the magnetic fields slowly disperse through the photosphere. A comprehensive review on the evolution of active regions can be found in van Driel-Gesztelyi and Green (2015).

Sunspots, and in particular their occurrence rate and position on the solar photosphere, can give a large amount of information about the solar cycle. Some examples are presented in Figure 2.4. The top panel of Figure 2.4 shows the famous *butterfly diagram*, first reported by Maunder (1904). By plotting the latitude of sunspot occurrence versus time, Annie and Edward Maunder noticed that sunspots tend to develop within an equatorial belt located between $\pm 35°$ latitude. Furthermore, they realised that at the beginning of each solar cycle sunspots tend to form at higher latitudes, and migrate towards lower latitudes with time until a new cycle starts. This recurrent behaviour gives rise to the butterfly pattern. Sunspots can also be analysed quantitatively, e.g. by counting their occurrence (this quantity is called the *sunspot number*) or their area (this quantity is called the *sunspot area*) on the solar disc. The sunspot area through several solar cycles is plotted in the bottom panel of Figure 2.4. The figure clearly

shows that solar activity varies approximate with 11-year periodicity and the amplitude of the cycle (i.e., the maximum sunspot area) varies significantly. Nowadays, each solar cycle has its own number, with solar cycle 1 starting in 1755, when extensive recordings of sunspots began. At the time of writing this thesis, we are at the very transition phase between solar cycle 24 and the following cycle 25.

2.1.3 Chromospheric features

After crossing the photosphere, emerging flux tubes from the solar interior (see Section 2.1.1) encounter the second layer of the Sun's atmosphere, the chromosphere. When observed in the Hα line at 6562.8 Å (or in general at chromospheric temperatures), active regions appear as bright spots against the "quiet" regions. In addition to active regions, Hα observations of the chromosphere reveal structures known as *filaments* (e.g., Parenti, 2014; Gibson et al., 2018). Filaments appear as dark curves against the solar disc and are composed of large amounts of dense material. They appear dark (i.e., in absorption) because they are much cooler than the solar surface beneath them. When seen off the solar limb, instead, filaments appear bright (i.e., in emission) and are called *prominences*. The double nomenclature arises from the fact that the existence of both filaments and prominences was known before they were identified as the same phenomenon seen against different backgrounds. Figure 2.5 shows examples of filaments and prominences. It is clear from Figure 2.5 that filaments can be located both in active regions and away from them. In light of this aspect, a common classification divides filaments into *quiescent*, *intermediate*, and *active region* filaments (e.g., Engvold, 2015). In general, filaments occurring in the vicinity of active regions are more dynamic, smaller, and shorter-lived than filaments associated with the quiet Sun (e.g., Martin, 1998a). The lifespan of a filament can range between several days (mostly active region filaments) to a few months (mostly quiescent filaments). The majority of filaments eventually undergo instabilities and erupt, and many of them are associated with CMEs. A few filaments, however, can disappear simply draining back their mass towards the chromosphere.

The low-coronal environments where filaments may form are known as *filament channels*. Filament channels lie along the boundaries between oppositely directed LOS magnetic fields, called *polarity inversion lines* (PILs). A filament channel may live longer than the lifespan of a single filament, and be replenished of new material after

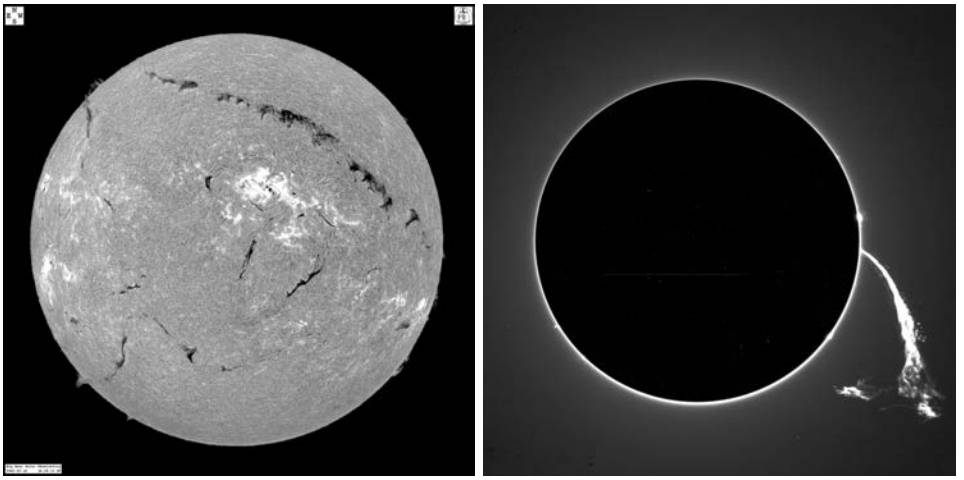

Figure 2.5: Left panel: Hα image from 2012, showing several active regions (bright regions) and filaments (dark thread-like structures). Image credit: Big Bear Solar Observatory. Right panel: Off-limb prominence eruption from 1992. Image credit: Norikura Solar Observatory.

a filament disappearance. Lower down on the chromosphere, filaments are associated with *fibrils* (called *spicules* when viewed off limb; Foukal, 1971b,a), visible as dark, elongated structures that trace the orientation of the surrounding magnetic fields. Fibrils are usually shorter-lived than filaments (their lifespan is of the order of tens of minutes), and considerably smaller in size. Fibrils have also been found to be asymmetric near filaments, with their apparent direction being opposite on the two sides of a filament (Martin et al., 1992). This feature has been proven useful when determining the direction of the magnetic field along a filament axis.

2.1.4 Coronal features

Finally, magnetic bundles that start their emergence from the Sun's interior (see Section 2.1.1) arrive to the outer layer of the solar atmosphere, the corona. Despite lacking a definite outer boundary, the corona is usually roughly divided into lower (close to the chromosphere), middle (up to a few solar radii), and outer (up to tens of solar radii) corona. The lower corona can be explored through images of the solar disc at different wavelengths—although these measurements are constrained by significant projection effects. The outer layers of the corona, on the other hand, cannot be observed through

simple photographs, because the solar disc is much brighter than its surroundings. The middle corona could be observed only during solar eclipses until 1931, when Lyot (1931) introduced an instrument that is widely used nowadays and that is called *coronagraph*. A coronagraph is an instrument that permits to image the solar corona through the creation of an "artificial eclipse", i.e. by covering the bright solar disc with the aid of an occulter, thus revealing the relatively faint surrounding corona. The off-limb prominence shown in the right panel of Figure 2.5 was, as a matter of fact, captured through a coronagraph. Coronagraphs can take images either at extreme ultra-violet (EUV) wavelengths or in white light, i.e. through the photospheric light that is scattered in the corona. White-light measurements of the corona detect two main components of scattered sunlight (e.g., Calbert and Beard, 1972). One is known as the K-corona (from *Kontinuerlich*) and arises from photospheric light that is Thomson-scattered by free electrons (for a review on the principles of Thomson scattering, see Howard and Tappin, 2009). The second is called the F-corona (from *Fraunhofer*) and is related to the photospheric light that is diffracted and reflected by dust particles distributed through interplanetary space along the LOS. In order to study solar transients in the corona, e.g. CMEs, the K- and F-components have to be separated and the F-component discarded.

The corona is also the place where the *solar wind* originates—a stream of charged particles that is continuously flowing from the Sun through interplanetary space. Due to a very high electric conductivity, the coronal magnetic field is "frozen-in" to the plasma flow. As a consequence, the solar wind carries the magnetic field with it throughout the heliosphere, forming thus the so-called interplanetary magnetic field (IMF; e.g., Owens and Forsyth, 2013). Due to corotation with the Sun, the IMF lines and, as a result, the solar wind that streams along those lines assume the shape of an Archimedean spiral, known as the *Parker spiral* (from Parker, 1958, that first predicted the existence of the solar wind). The solar wind is observed in two basic states, *slow* and *fast*. The slow solar wind is dense, has typical speeds around 300–400 $\mathrm{km \cdot s^{-1}}$, and its composition is close to the solar corona's. The fast solar wind, in turn, is less dense but faster (its speed is around 700–800 $\mathrm{km \cdot s^{-1}}$) and its composition resembles rather the one of the photosphere.

The study of the solar disc at EUV and X-ray wavelengths (see Del Zanna and Mason, 2018) has revealed a significant amount of features in the lower corona. Active regions appear as bright, dynamic regions on the disc, characterised by magnetic loops (known

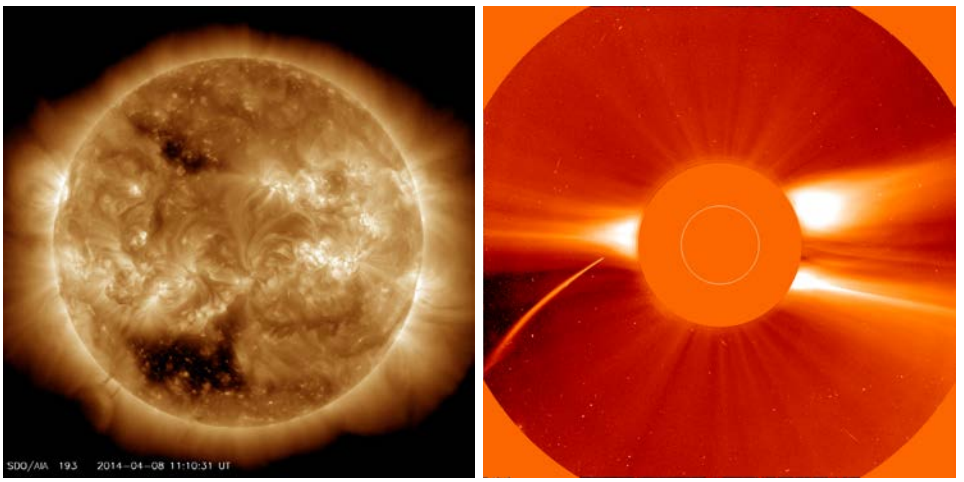

Figure 2.6: Left panel: EUV image of the solar disc at 193 Å taken in April 2014, showing bright active regions and dark coronal holes. Image credit: NASA—SDO/AIA. Right panel: White-light coronagraph image taken in December 1996, showing several streamers and a bonus sungrazing comet. The extent of the solar disc is indicated by the white circle. Image credit: ESA–NASA SOHO/LASCO.

as *coronal loops*) that evolve and reconfigure on short timescales through interaction with the surrounding magnetic fields (e.g., Reale, 2014). EUV observations of the solar disc also reveal dark, extended regions that are called *coronal holes*—regions of open field lines where the solar magnetic field reaches into space (e.g., Cranmer, 2009). Coronal holes are also the sources of the fast solar wind (Zirker, 1977), whilst the origin of the slow solar wind is still under debate, although it is believed to be related to the so-called *streamer belt regions* (e.g., McComas et al., 2008). The streamer belt extends around the whole Sun and runs between the large-scale regions of opposite polarity of magnetic field lines. The structure of the streamer belt changes dramatically with the solar cycle, being confined near the solar equatorial plane during solar minimum and widening towards higher latitudes at solar maximum. *Helmet streamers* appear between coronal holes of opposite polarity (e.g., Wang et al., 2000), whereas *pseudostreamers* separate coronal holes of the same magnetic polarity (e.g., Wang et al., 2007). Figure 2.6 shows examples of the features introduced in this section, with active regions and coronal holes visible in the low corona (left panel) and streamers visible in the middle-to-outer corona (right panel).

2.2 Space weather drivers

It is clear from Section 2.1 that the Sun is a highly complex star, with its atmosphere and activity shaped by the ever-evolving magnetic field that is generated and maintained in the solar interior. Thus, the plasma and magnetic field in the convective zone are also ultimately the origin of space weather phenomena. The "disturbances" or "transients" in the solar wind that are able to drive space weather effects can originate and take place on very different temporal and spatial scales. This section provides a brief summary of the main space weather drivers.

2.2.1 Coronal mass ejections

Coronal mass ejections (CMEs; e.g., Webb and Howard, 2012) are possibly the most spectacular phenomena related to solar activity. They are also the drivers of the most extreme space weather effects at Earth and throughout the heliosphere (i.e., the region of space that is under the influence of the Sun). Their masses can reach up to $\sim 10^{13}$ kg, their kinetic energies up to $\sim 10^{25}$ J, and their speeds close to the Sun up to $\sim$3000 km$\cdot$s^{-1}, with average values being $\sim 10^{12}$ kg for mass, $\sim 10^{23}$ J for energy, and $\sim$500 km$\cdot$s^{-1} for speed (e.g., Yashiro et al., 2004; Yurchyshyn et al., 2005; Vourlidas et al., 2010; Webb and Howard, 2012). Since the whole Chapter 3 of this thesis is centred on CMEs, only a brief review is presented here.

As mentioned in the Introduction, CMEs are huge releases of plasma and magnetic flux from the solar atmosphere into interplanetary space, usually with the structure of a magnetic flux rope. Plasma material from the corona, and in part from the chromosphere and photosphere, is entrained on such helical magnetic field. There is no unanimous consensus on the actual onset mechanism, but it is generally accepted that CMEs result from a catastrophic, runaway disruption of an energised and stressed pre-eruptive field configuration resulting in the rapid conversion of free magnetic energy stored in the corona to kinetic energy, radiation, bulk heating, and particle acceleration. Since several different types of CMEs have been observed through remote-sensing imaging (e.g., regarding their size, speed, initial acceleration, and morphology as observed in coronagraphs), it is likely that not all eruptions are triggered in the same way and different onset mechanisms may explain different CMEs.

After erupting, CMEs undergo rapid acceleration in the lower corona and then expand

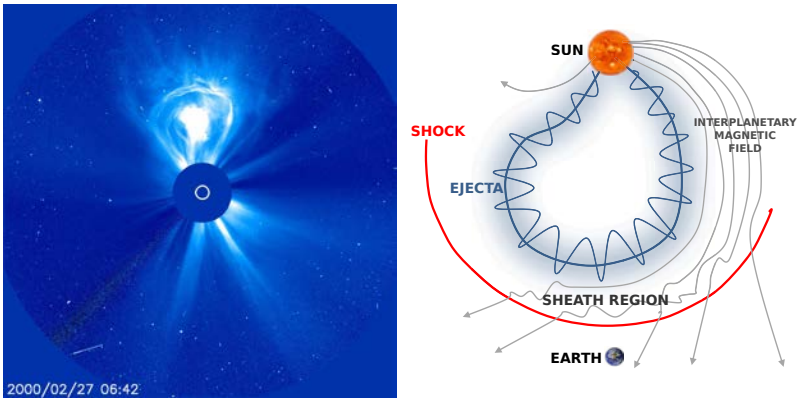

Figure 2.7: Left panel: The famous "light bulb" CME from February 2000, showing the classic three-part structure, seen in a white-light coronagraph image. Image credit: ESA–NASA SOHO/LASCO. Right panel: Sketch of an ICME as seen from above. The ICME is composed of a shock, a sheath region, and an ejecta. Adapted from Kilpua et al. (2017).

throughout interplanetary space. Studies of CMEs in the outer heliosphere have shown that expansion ceases around 15 AU, when CMEs finally reach pressure balance with the ambient wind (Richardson et al., 2006). As magnetic fields are space-filling, the solar wind outflow drags the CME field with it to fill the heliosphere. When observed in coronagraph images, CMEs may exhibit what is now known as the classic *three-part* structure (Illing and Hundhausen, 1985, see left panel of Figure 2.7), i.e. composed of a bright rim, a dark cavity, and a bright core (see Section 3.2.1 for a discussion on the three-part structure of CMEs).

Depending on the initial speed of the CME and the ambient solar wind speed, it takes between 1–5 days for a CME to reach Earth. When the relative speed of a CME with respect to the preceding solar wind exceeds the local magnetosonic speed, a fast-forward shock wave forms ahead of the CME. In such cases, a turbulent region of piled-up magnetic field and compressed plasma develops between the shock and the CME itself, known as a *sheath region* (e.g., Kaymaz and Siscoe, 2006; Siscoe and Odstrcil, 2008; Kilpua et al., 2017). Throughout this thesis, the term *interplanetary coronal mass ejection* (ICME; e.g., Kilpua et al., 2017) will indicate the interplanetary structure in its entirety, i.e. composed of a shock, a sheath, and an ICME *ejecta*. A schematic representation of an ICME on its way towards Earth is shown in the right panel of Figure 2.7.

2.2.2 Solar energetic particles

Another important source of space weather effects on Earth and other planets is represented by the so-called *solar energetic particles* (SEPs; e.g., Klein and Dalla, 2017; Malandraki and Crosby, 2018). SEPs consist of electrons, protons, and heavier nuclei that are accelerated to high energies and travel through interplanetary space largely along IMF lines. There are two main locations where energetic particles may be accelerated, namely *solar flares* and *CME-driven interplanetary shocks*. Particles accelerated at flares are known as *impulsive SEP* events, whilst those accelerated by shocks are called *gradual SEP* events. When gradual SEPs event are detected near Earth, they are also known as *energetic storm particle* (ESP) events (Desai and Giacalone, 2016). Figure 2.8 shows a schematic representation of impulsive and gradual SEP events.

Solar flares (e.g., Benz, 2017) are localised, short-lived brightenings on the Sun over a vast range of wavelengths interpreted as the impulsive release of magnetic energy through a process called *magnetic reconnection* (see Section 3.1.1). They may or may not be associated to a CME eruption. Magnetic reconnection at the flare location is believed to heat the plasma and accelerate electrons along the IMF lines. Since flares are short-lived phenomena, impulsive SEP events last a few hours only. CME shocks, on the other hand, accelerate particles over larger temporal and spatial scales, therefore gradual SEP events usually last several days and are believed to drive stronger space weather effects. The peak intensities and spectral shapes for a gradual SEP event are usually related to the strength of the CME shock (Kahler, 2001; Rice et al., 2003). In some cases, SEPs driven by very strong shocks associated with large and fast CMEs can be detected over a wide range of heliolongitudes (e.g., Dresing et al., 2012; Guo et al., 2018; Lee et al., 2018).

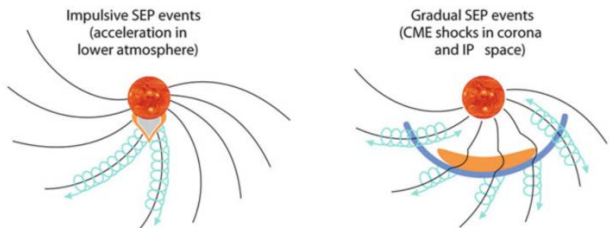

Figure 2.8: Schematic representation of (left) impulsive and (right) gradual SEP events. Adapted from Desai and Giacalone (2016).

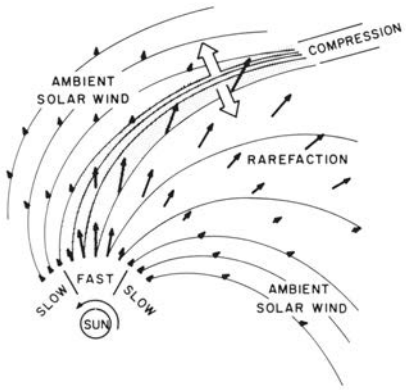

Figure 2.9: Schematic representation of a SIR. Reproduced from Pizzo (1978).

2.2.3 Stream interaction regions

Finally, the last drivers of space weather disturbances to be reviewed in this section are known as *stream interaction regions* (SIRs; e.g., Richardson, 2018). As their name suggests, SIRs arise from the interaction of two solar wind streams, namely a high-speed wind originating from a coronal hole (see Section 2.1.4) with the preceding slower wind. Such interaction results in a compressed interface between the two streams, shown in a schematic representation in Figure 2.9.

As mentioned in Section 2.1.4, the solar wind that flows away from the Sun is organised into an Archimedean spiral structure. However, higher speed streams are less tightly wound in the Parker spiral compared to slower ones, thus the faster wind can overtake the slower wind ahead of it. Since the coronal holes from where the fast wind originates tend to last several months, the same SIRs persist over several solar rotations and corotate with the Sun. Hence, SIRs that are associated to long-lasting coronal holes are referred to also as *corotating interaction regions* (CIRs). Due to symmetry about the pressure enhancement caused by the compression of the slow wind ahead of the fast stream, a so-called *Forward–Reverse shock pair* may form at the leading and trailing edges of an expanding SIR (e.g., Jian et al., 2006b). In such a configuration, the forward shock propagates away from the Sun, whilst the reverse shock propagates towards the Sun, but is nevertheless carried away with the solar wind flow.

2.3 Space weather at Earth

The space weather effects resulting from the impact at Earth of a CME, a SIR, or a flux of SEPs are not uniform, but instead vary from case to case. Some events pass past Earth without causing any significant effect, some are able to drive moderate space weather storms, and some others major disturbances. In order to provide a complete overview of terrestrial space weather, this section begins with a brief review of the structure of Earth's magnetosphere, followed by a description of how solar transients cause geomagnetic disturbances, and finally by a description of some indices that can be used to quantify a geomagnetic storm.

2.3.1 Earth's magnetosphere

A magnetosphere is a cavity in the solar wind flow caused by the interaction of the solar wind itself with the intrinsic magnetic field or the ionised atmosphere of a planetary body. In Earth's case, the magnetosphere is mainly the result of the solar wind interaction with Earth's quasi-dipolar magnetic field.

An artistic representation of Earth's magnetosphere is shown in the right panel of Figure 2.10. The shape of the magnetosphere is a direct consequence of the continuous stream of plasma and magnetic field from the solar wind. The solar wind compresses the magnetosphere at the *dayside* (i.e., the side that is facing towards the Sun) and stretches is out at the *nightside* (i.e., the side that is facing away from the Sun). Ahead of Earth, a shock wave forms as a result of the abrupt drop of the solar wind speed, called *bow shock*. The actual boundary of Earth's intrinsic magnetic field, in pressure balance with the IMF, is called *magnetopause*. The turbulent region between the bow shock and the magnetopause is known as *magnetosheath*, which is formed of mainly shocked solar wind, albeit with some material from the magnetosphere itself. The night-side magnetosphere is called *magnetotail*, formed of two *lobes* (northern and southern) and a *plasma sheet* between them. The distance between Earth's centre and the magnetopause nose is variable and depends on the ram pressure exerted by the solar wind, but its nominal position is estimated around 10 Earth radii (R_E) in the sunward direction (e.g., Cahill and Amazeen, 1963). The exact length of the magnetotail, on the other hand, is unknown, but it is believed to extend out to about 1000 R_E (e.g., Ness et al., 1967).

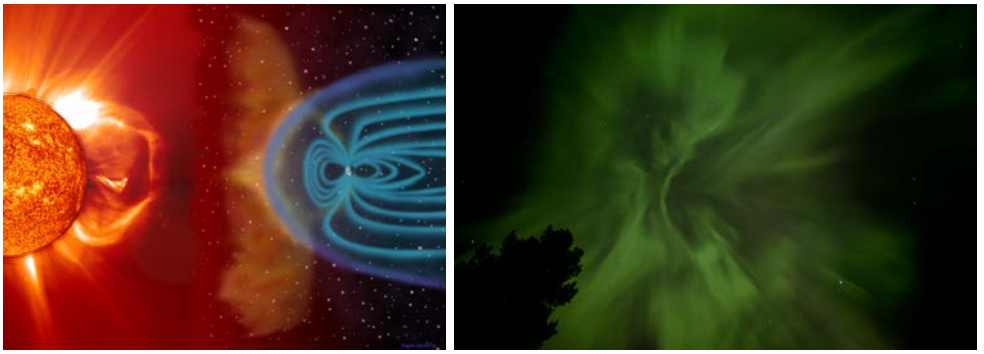

Figure 2.10: Left panel: Artistic view of a CME interacting with Earth's magnetosphere. Image credit: Steele Hill – NASA. Right panel: Aurora in Loppi, Finland, on 17 March 2015. Image credit: Juhana Lankinen.

2.3.2 Geoeffective solar transients

Even if Earth is in large part protected from hazardous structures coming from the Sun, solar transients are usually able to "penetrate" the magnetosphere and expose the near-Earth environment to increased radiation and electric currents. At the dayside nose of the magnetosphere, Earth's intrinsic quasi-dipolar magnetic field is directed northwards, i.e., its field lines escape from the magnetic pole in the Southern hemisphere and re-enter at the magnetic pole in the Northern hemisphere, reaching again the South pole in the planet's interior. Solar transients may cause substantial deviations from the nominal Parker spiral structure, mostly in terms of strong, out-of-ecliptic components.

When antiparallel magnetic fields come into contact, *magnetic reconnection* occurs resulting in the topological reconfiguration of magnetic field lines. This reconfiguration transfers magnetic flux and plasma through the current sheet and between interacting flux systems. Because of these aspects, solar wind structures (as a CME or a SIR) can be *geoeffective* when they contain southward-directed magnetic fields. In the artistic representation shown in the left panel of Figure 2.10, a CME is interacting with Earth's magnetosphere. When the IMF reconnects at the dayside magnetopause, the newly connected field lines (having one footpoint at Earth and one at the Sun) get dragged from the dayside towards the magnetotail, exposing Earth's polar regions to the solar wind. At the same time, the pileup of magnetic field at the lobes in the nightside

initiates reconnection at the magnetotail as well, bringing magnetic field and plasma towards Earth on one side and expelling the reconnected fieldlines on the other side (away from the Sun). This pattern is known as the *Dungey cycle* (Dungey, 1961).

The magnetospheric plasma flow that occurs during the Dungey cycle generates a dawn–to–dusk electric field, which is responsible for convective motions within the magnetosphere and transport of charged particles from the tail plasma sheet into the inner magnetosphere. The effects of geoeffective solar transients are also manifest through the strong auroral activity that is observed around the auroral ovals at both poles. An impressive auroral display is shown the right panel of Figure 2.10. The increased ram pressure associated with interplanetary shock and fast streams can compress the magnetopause, in which case the compression effects travel tailward at the solar wind speed (e.g., Pulkkinen, 2007).

In addition to solar wind structures interacting with the magnetosphere, SEPs can have sufficient energies to break through the magnetosphere, exposing the environment around Earth to an increased flux of high energy protons (e.g., Malandraki and Crosby, 2018).

2.3.3 Geomagnetic indices

In order to quantify how the geomagnetic field and the magnetosphere respond to a space weather event, a series of *geomagnetic indices* based on ground-based observatory data have been developed. Each of the many existing indices characterise a different aspect or time scale of the dynamic geomagnetic field. The four most widely used indices nowadays are *Kp*, *ap*, *AE*, and *Dst* (Rostoker, 1972).

The *Kp* index is a measure of geomagnetic activity worldwide, with contributions from both the *auroral electrojets* and the *ring current*. It is computed every 3 hours from ground-based magnetometers around the world. Each station is calibrated according to its latitudinal position and the measurements—of the deviation of the horizontal component of the magnetic field—taken at each station are computed together into a semi-logarithmic scale that ranges from 0 to 9. The *ap* index is derived directly from the *Kp*, with the difference of being based on a linear scale (from 0 to 400). The *AE* (Auroral Electrojet) index is used to estimate activity in the auroral zone. For this reason, only ground stations that are located along the auroral zone are included in

the calculation of the index. The *AE*, like the *Kp*, is also based on variations in the horizontal component of the magnetic field, with the five international quietest days for each month being used as a reference baseline. Each minute, data from all the stations are collected and the largest and smallest values are selected. The difference between these values forms the *AE* index.

Of all the existing indices, the most widely used in the CME research community is perhaps the *Dst* (Disturbance storm time) index, which is based on magnetometer measurements from four ground stations located near Earth's equator. The *Dst* index is calculated every hour and is a measure of the magnetic perturbation at the centre of Earth's dipole due to currents in space around Earth (i.e., the ring current). It is measured in nanoteslas and depends on the average value of the horizontal component of Earth's magnetic field near the equator. A value of $Dst \simeq 0$ nT means that the ring current is at quiet times. During a classic geomagnetic storm, the *Dst* shows first a sudden rise (the *storm sudden commencement*, when the IMF turns southwards) and then a sharp decrease (the *storm main phase*, when the ring current intensifies), before slowly returning to quiet time values (the *storm recovery phase*, when the IMF turns northwards and the ring current starts to recover). Usually, a geomagnetic storm is defined as *minor* when $0 \text{ nT} > Dst_{\min} > -50$ nT, *moderate* when $-50 \text{ nT} \geq Dst_{\min} > -100$ nT, and *major* when $Dst_{\min} \leq -100$ nT (e.g., Zhang et al., 2007). Furthermore, the *Dst* index can be modelled fairly well using solar wind parameters as input (e.g., Burton et al., 1975; O'Brien and McPherron, 2000; Temerin and Li, 2002), which is a useful property when estimating the geoeffectiveness of CMEs detected at other locations than Earth (e.g., Liu et al., 2014; Paper IV). The *Dst* index has been used to quantify the geomagnetic impact of ICMEs in Paper III and Paper IV.

3 Coronal mass ejections from the Sun to Earth

♪ *Children of the Sun* – Billy Thorpe

The previous chapter has provided an overview of the solar–heliospheric connection of the Sun–Earth system. It has been briefly discussed that CMEs are the most dynamic large-scale transients that are capable of driving significant geomagnetic responses. The importance of studying CMEs is thus tightly related to space weather forecasting, and involves knowledge of how CMEs erupt from the Sun and how their morphology and internal structure changes before they impact Earth. Accordingly, this chapter is centred on CMEs and their journey, from their eruption at the Sun through their interplanetary evolution up to their arrival at Earth.

3.1 CME onset and eruption

To date, the exact onset mechanism of CMEs has not been observed directly. A common consensus, nevertheless, is that CMEs erupt as a result of instabilities arising in the solar corona and that the erupting structures often have a helical magnetic configuration that is known as a flux rope. This section reviews the main theories that aim to explain what instabilities trigger CME eruptions and then focusses on the flux rope nature of CMEs from an observational viewpoint.

3.1.1 Possible onset mechanisms

Since the issue of CME onset has not been resolved observationally yet, various initiation mechanisms have been explored with theory and numerical simulations, and increasingly these are combined with detailed analyses of both remote and in-situ observations of CMEs and their resulting flux ropes. Since the plasma beta (β; i.e., the ratio of the plasma pressure to the magnetic pressure) is low in the solar corona, then it must follow that the CME onset and eruption mechanisms are magnetically dominated phenomena. Forbes (2000) has shown that the coronal magnetic field is the only quantity that contains sufficient energy density to drive an eruption. Therefore, CME

modelling and numerical simulations have focussed on the gradual energy accumulation and the (more) rapid energy release associated with quasi-static stressed coronal magnetic field configurations suddenly going unstable and erupting.

Magnetic flux emergence, its evolution, and cancellation all occur during the lifetime of active regions. Photospheric motions associated with each of these phases, including shearing, rotational, and granulation flows, all impart stress into the overlying coronal magnetic fields. The stressed field configurations may take the form of a *sheared arcade*, which connects directly two opposite magnetic polarities over the local neutral line, or a *flux rope*, where the connection is made via helical field lines. Additionally, sheared arcade magnetic configurations can become twisted flux ropes during flux cancellation, where converging flows drive reconnection at the polarity inversion line (e.g., van Ballegooijen and Martens, 1989; Moore et al., 2001; Linker et al., 2001, 2003; Amari et al., 2011; Aulanier et al., 2012; Török et al., 2018). Linker and Mikic (1995) showed that an energised bipolar helmet streamer configuration expands outwards to create an extended radial current sheet. Magnetic reconnection at this current sheet rapidly forms a twisted flux rope that is ejected out of the simulation domain. This generic eruption scenario—in which the evolution of solar flares and the eruption of a CME are linked through the magnetic reconnection process—is often referred to as the CSHKP model (Carmichael, 1964; Sturrock, 1966; Hirayama, 1974; Kopp and Pneuman, 1976). A consequence of this scenario is that the erupting CME almost always contains a flux rope or flux rope-like structure regardless of the specific pre-eruption magnetic configuration (e.g., Gosling et al., 1995; Forbes, 2000; Klimchuk, 2001; Chen, 2011; Green et al., 2018; Welsch, 2018).

Several CME eruption models have been developed and they have been used to simulate a number of CMEs through the past few decades, but no model has been able yet to reproduce the variety of different eruptions that can be observed on the Sun. Hence, it is possible that a unified (or unifying) model has to yet be theoritised, or that different models are needed to describe different types of CMEs. If the stressed, pre-eruptive active region field structure is a magnetic flux rope, then ideal magnetohydrodynamic (MHD) instabilities may cause the rapid loss of equilibrium if certain criteria are met. For example, a highly twisted flux rope can go *kink unstable* if it accumulates too much twisted flux (i.e., 2–3 full turns over the length of the flux rope axis; e.g., Hood and Priest, 1979; Gibson et al., 2004; Török et al., 2004; Török and Kliem, 2005). Alternatively, the hoop-force associated with a magnetic flux rope geometry can cause

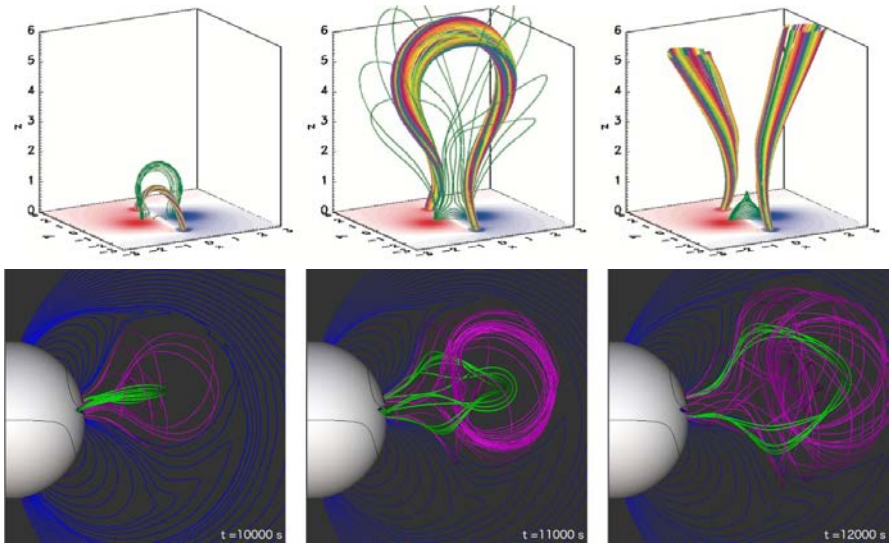

Figure 3.1: Top panels: Snapshots of the simulation of a kink-unstable erupting flux rope. Adapted from Török and Kliem (2005). Bottom panels: Snapshots of the simulation of a flux rope forming by flare reconnection during a magnetic breakout eruption. Adapted from Lynch et al. (2009).

runaway expansion leading to eruption if the overlying field strength impeding this expansion falls off sufficiently fast. This scenario is known as *torus instability* and is usually described in terms of a critical decay index of the overlying field strength (e.g., Kliem and Török, 2006; Kliem et al., 2014). In other words, once the flux rope has expanded to a height where the decay index is met, the eruption is inevitable. An alternative class of instabilities that can disrupt the system are known as resistive MHD instabilities. Largely, these describe magnetic reconnection occurring somewhere in the system that leads to runaway expansion and CME eruption. The *tether-cutting* (Moore et al., 2001) and *flux cancellation* (Linker et al., 2003) scenarios remove the overlying restraining flux via reconnection to build the twisted flux structure and create the conditions favourable for the CSHKP scenario to proceed. The *breakout* model requires a stressed coronal null point above the stressed filament channel fields which forms a current sheet and allows magnetic reconnection to remove the overlying restraining flux via reconnection from above (e.g., Antiochos et al., 1999; Lynch et al., 2004, 2008).

Figure 3.1 shows modelling results of CME initiation from two example instability

mechanisms: a flux rope undergoing *kink instability* (ideal instability, top row) and a flux rope forming during a *magnetic breakout* eruption (resistive instability, bottom row). In both models, the resulting erupting flux rope can be considered as the close-to-the-Sun counterpart of the ICME ejecta depicted in the left panel of Figure 2.7.

3.1.2 The flux rope structure of CMEs

CME flux ropes are easily identified in models (see Figure 3.1), but observing the magnetic structure of erupting flux ropes in the solar atmosphere is a more complicated issue. This is because the coronal magnetic fields cannot be observed and measured directly. Nevertheless, a number of indirect proxies can be used and combined in order to estimate the magnetic configuration of flux ropes at the time of their eruption. A "simplified" version of a flux rope can be thought of as a magnetic tube consisting of two main magnetic field contributions: the *axial field*, which runs through the centre of the tube, and the *helical field*, which winds about the axis of the tube. Based on interplanetary observations, different *flux rope types* have been suggested that reflect different combinations of the axial and helical fields (Bothmer and Schwenn, 1998; Mulligan et al., 1998). Figure 3.2 displays the main flux rope types classified with respect to the inclination of their axis to the ecliptic plane (low-inclination or high-inclination) and their chirality (or handedness, i.e., the sense of twist in the flux rope). The letters under each sketch in Figure 3.2 indicate the four directions (North, West, South, and East) and describe the magnetic field directions that a spacecraft crossing the flux rope would progressively encounter. For example, in the case of an NES-type flux rope, a spacecraft would first detect the outer helical field (directed towards the North), then the axial field (directed towards the East), and finally the inner helical field (directed towards the South).

Remote-sensing observations of the coronal structures that participate in the CME eruption process on the solar disc can be used as indirect proxies for determining the flux rope type during the CME initiation. Specifically, the information that is necessary to obtain from remote-sensing observations in order to determine the flux rope type at the Sun (or *intrinsic flux rope type*) is: *helicity sign* (also known as chirality or handedness), *tilt of the axis*, and *magnetic field direction* at the axis. The indirect proxies that can be used to estimate these parameters may involve photospheric, chromospheric, and coronal observations and are reviewed thoroughly in Paper II, hence a

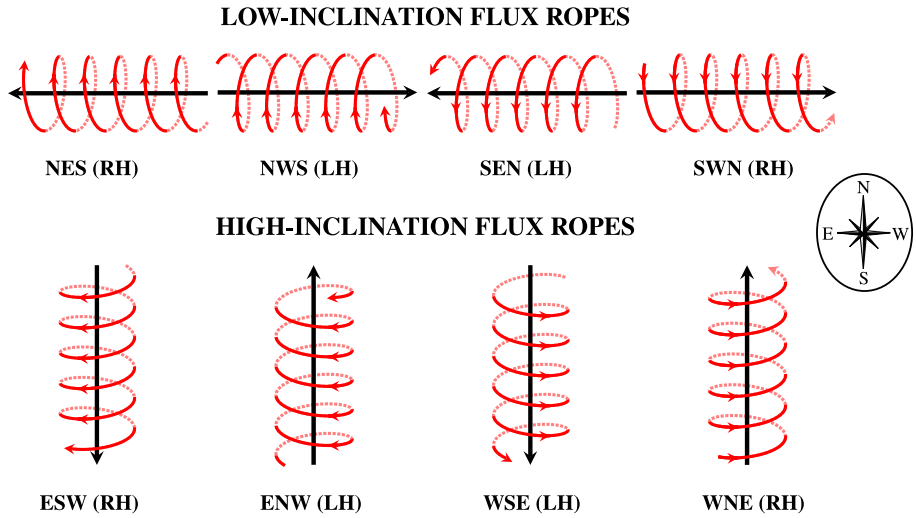

Figure 3.2: Schematic representation of the eight main flux rope types, divided according to their inclination with respect to the ecliptic plane and following the classification from Bothmer and Schwenn (1998) and Mulligan et al. (1998). The axial and the helical fields are shown in black and in red, respectively. The letters under each flux rope represent the four directions (North, West, South, and East, shown in the insert on the right), whilst RH indicates right-handed and LH indicates left-handed helicity. In the sketches, it is assumed that the flux ropes are moving towards the observer. Adapted from Paper III.

brief summary is provided here.

Observations of the pre-eruptive CME source region can give information on the flux rope chirality after the eruption and also through interplanetary propagation, since magnetic helicity is believed to be a conserved quantity (Berger, 2005). Statistical studies (e.g., Pevtsov and Balasubramaniam, 2003) have found a tendency for CME flux ropes erupting from the Northern (Southern) hemisphere to be associated with a left-handed (right-handed) twist (i.e., the sense in which the magnetic fields are bending in their helical pattern), property that is known as the *hemispheric helicity rule*. However, this rule holds only for about 60–75% of the cases (Pevtsov et al., 2014). Hence, chirality is a parameter that should be determined case by case and that can be estimated from:

- **Magnetic tongues** (e.g., López Fuentes et al., 2000; Luoni et al., 2011), which

are visible on the photosphere during the emergence phase of active regions (or Ω-loops, see Section 2.1.2) as asymmetries in the elongation of the emerging magnetic polarities. A positive (negative) twist is represented by the leading polarity extending under (above) the trailing one.

- **Filament details** (e.g., Martin and McAllister, 1996; Martin, 1998b; Chae, 2000), which can be observed both in Hα and in EUV. Several patterns can be studied in Hα to deduce the chirality of the filament and, as a consequence, of the erupting flux rope; e.g., the bearing of the filament legs and the orientation of the filament barbs (i.e., the fine structure of filaments). In EUV, filaments are often observed as a combination of emission and absorption threads, and the geometry of the thread crossings can be used to study the associated helicity sign. Furthermore, erupting filaments are often observed to rotate clockwise (anticlockwise) upon eruption when they are right- (left-) handed (e.g., Green et al., 2007; Lynch et al., 2009).
- **S-shaped structures** (e.g., Rust and Kumar, 1996; Green et al., 2007), which can be associated with either multi-loop sheared coronal arcades or single-loop sigmoids. Forward (reverse) S-shapes form in regions dominated by right- (left-) handed chirality.
- **Coronal loops' skew** (e.g., McAllister et al., 1998; Martin, 1998b), which can be estimated in soft X-rays and/or EUV and is represented by the acute angle that the overlying coronal loops make with the local PIL or (if present) the filament axis. Right- (left-) skewed loops are associated with positive (negative) helicity flux ropes.
- **Flare ribbons** (e.g., Démoulin et al., 1996), which are two J-shaped emission structures that are often associated with CME eruptions and that are believed to track the footpoints of newly-reconnected magnetic field lines during a flare on the photosphere and chromosphere. Forward (reverse) J-shapes are associated with positive (negative) helicity of the corresponding flux rope.

CMEs always erupt above PILs, since the shear and twist necessary to stress the pre-eruptive magnetic fields builds along the line between two polarities, i.e., perpendicular to the original potential field. Hence, the direction of the PIL can be used as an indicator of the erupting flux rope inclination with respect to the ecliptic plane (e.g., Marubashi et al., 2015). Furthermore, the elongated coronal loops that are often visible on the Sun and that originate from either side of the PIL after an eruption as a result of magnetic reconnection, known as *post-eruption arcades* (PEAs), can also be used

as an indicator of the orientation of the flux rope axis (e.g., Yurchyshyn, 2008). When PEAs are visible well enough, the average between the orientations of the PIL and the PEAs is considered a valid approximation for the flux rope tilt (Paper III).

The direction of the axial magnetic field of a flux rope can be estimated if the locations where its footpoints are rooted are known. The footpoints of a CME can be traced on the corona through dark features known as *coronal dimmings* (e.g., Thompson et al., 2000), which correspond to the evacuation of coronal material that is fed into the rising CME (e.g., Hudson and Webb, 1997). Thus, when the CME footpoints are located, magnetogram data can be used to associate each footpoint to its corresponding magnetic polarity. Then, the flux rope axial magnetic field is directed from the positive to the negative polarity.

It was shown in Paper III that the combination of the methods described above allow determination of the intrinsic flux rope type for various kinds of eruptions, e.g., for CMEs erupting from an active region, from filaments lying on the quiet Sun, or from between two active regions. Figure 3.3 shows examples of intrinsic flux rope type determination for two CMEs that are used as showcase events in Paper III. The CME shown in the left panels erupted as an NES-type flux rope, as can be estimated from the right-handed magnetic tongues of its source region, the presence of forward S-shaped loops, and the eastward-directed axial field at a low inclination to the ecliptic plane. The CME shown in the right panels, on the other hand, erupted as an intermediate type between WSE and NWS, as can be seen from the reverse S-shaped loops, the left-handed crossings of its filament threads, and its axial field directed towards the Southwest.

3.2 Coronal and heliospheric evolution of CMEs

After erupting from the Sun, CMEs commence their journey through the solar corona and interplanetary space, being carried away with the solar wind. Since CME magnetic fields are higher than the ones found in the surrounding environment, the internal magnetic pressure always results in an expansion of the CME body during propagation. The speed profiles, on the other hand, depend on the relationship between the speed of the CME and that of the ambient solar wind. The coronal and heliospheric evolution of CMEs after eruption is reviewed in this section.

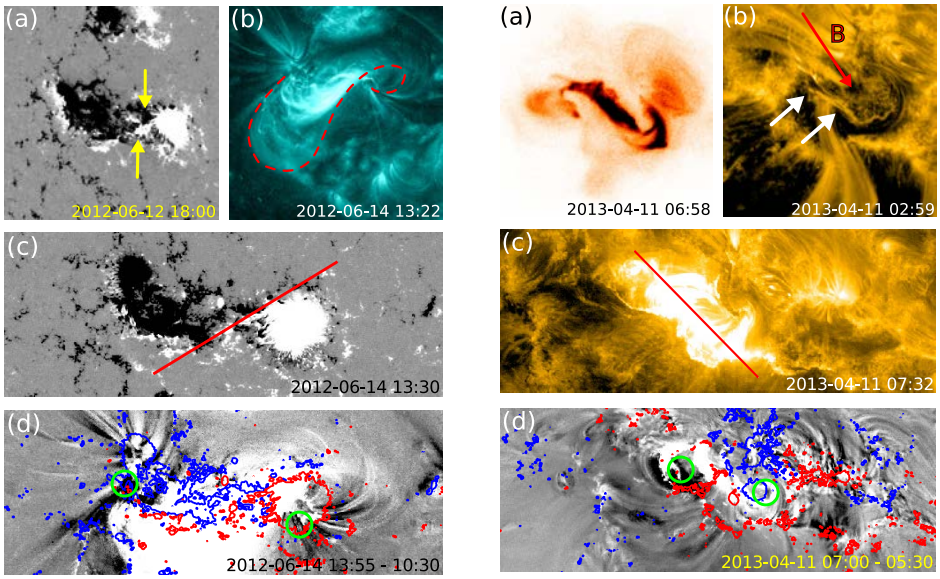

Figure 3.3: Examples of determination of the intrinsic flux rope type for two case studies. Left panels: Observations of the source region of the 14 June 2012 CME. (a) Right-handed magnetic tongues; (b) Right-handed sigmoid; (c) Axis orientation determined from the PIL; and (d) Flux rope footpoints (circled in green) overlaid with magnetogram data (red = positive polarity, blue = negative polarity). Right panels: Observations of the source region of the 11 April 2013 CME. (a) Left-handed sigmoid; (b) Left-handed filament threads crossings; (c) Axis orientation determined from the PEAs; and (d) Flux rope footpoints (circled in green) overlaid with magnetogram data (red = positive polarity, blue = negative polarity). These observations are made using the *Atmospheric Imaging Assembly* (AIA; Lemen et al., 2012) and HMI instruments onboard SDO and the *X-Ray Telescope* (XRT; Golub et al., 2007) onboard *Hinode* (Solar-B; Kosugi et al., 2007). Adapted from Paper III.

3.2.1 Propagation in the corona

The propagation of CMEs in the solar corona can be followed through coronagraph imaging (an example of a CME as observed by a coronagraph is shown in Figure 2.7). CMEs that are seen in white-light coronagraph images can present a variety of shapes and features. The first aspect to note is the morphology of the CME body. The classic three-part CME structure (Illing and Hundhausen, 1985) introduced in Section 2.2.1

is interpreted such that the dark cavity represents the flux rope, the bright outer rim the piled-up plasma at the leading edge of the outward moving flux rope, and the bright core the filament/prominence material (e.g., Dere et al., 1999; Vourlidas et al., 2013). A three-part CME, however, is usually identified in about a third of the cases (Munro et al., 1979; Vourlidas et al., 2017). In the majority of the events, CMEs may appear in white light as bright loops or even as irregular clouds or jets with no clear structure. It is still unclear whether different CME morphologies seen in white light are due to projection effects (e.g., Howard et al., 2017) or to intrinsically different structures, although recent studies have proven that the bright external loop can be interpreted as the pileup of material at the outer edge of the flux rope regardless of the three-part appearance and that most of the white-light shapes can be explained by helical structures (Vourlidas et al., 2013, 2017).

When looked at in coronagraph imagery, fast CMEs may appear surrounded by a fainter bright emission. These features have been identified as the density compression behind the shock wave front driven by the CME that moves faster than the characteristic speed of the ambient medium (e.g., Vourlidas et al., 2003, 2013). The turbulent and compressed material that piles up between a CME and the shock wave that it drives is representative of the sheath region (see Section 2.2.1) that starts to build up already during the early phases of the CME propagation. Some CME-driven shocks can be dected from the low corona outwards also at radio wavelengths through the emission from electrons accelerated at the shock wave front, known as *type II radio bursts* (e.g., Vršnak and Cliver, 2008; Magdalenić et al., 2010).

One of the major goals when studying CMEs in the solar corona is the determination of their 3D structure and properties (e.g., Cremades and Bothmer, 2004; Bosman et al., 2012). Long-term uninterrupted coronagraph observations have been available since 1996, when the SOHO spacecraft, equipped with the *Large Angle and Spectrometric Coronagraph* (LASCO; Brueckner et al., 1995), began its operations from Earth's Lagrange L1 point. However, stereoscopic studies of CMEs in white light began about a decade later, thanks to the *Sun Earth Connection Coronal and Heliospheric Investigation* (SECCHI; Howard et al., 2008) suite onboard the twin *Solar Terrestrial Relations Observatory* (STEREO; Kaiser et al., 2008) spacecraft that were launched in 2006 to orbit the Sun at a heliocentric distance of about 1 AU. Simultaneous observations of CMEs from two or more viewpoints have enabled reconstructions of the 3D morphology, position, and kinematics of CMEs using simplified shapes, e.g. the cone (Fisher

and Munro, 1984) or the graduated cylindrical shell (GCS; Thernisien et al., 2006, 2009) models. The GCS model can be described as a "hollow croissant" (Thernisien, 2011), consisting of a torus-like front that is connected to two conical legs. The electron density is placed on the shell boundary only and the whole inner structure is hollow. The cone model model can be described as an "ice cream", consisting of a single cone with a spherical top, i.e., it is the limit of the GSC model where the angle between the legs of the CME becomes zero. Figure 3.4 shows an example of a CME (top row) reconstructed with the cone model (middle row) and with the GCS model (bottom row). The bright feature that encompasses the CME bubble represents the white-light shock discussed above. One limitation of such stereoscopic reconstruction methods is that they do not provide information about the flux rope internal magnetic field, as the envelopes used to perform the fittings are hollow and lack a magnetic structure. In the case of the GCS morphology, the axis along which the shell elongates can be assumed to correspond to the flux rope axis; however, the direction of the magnetic field along such axis is characterised by a 180° ambiguity.

3.2.2 Interplanetary transit

After CMEs leave the coronagraphic field of view, their journey through interplanetary space cannot be followed routinely anymore. Nevertheless, two main observational approaches have been used to study how CMEs evolve between the outer corona and 1 AU. Firstly, CME evolution can be studied using in-situ data from the spacecraft that have ventured through the inner heliosphere closer to the Sun than Earth's orbit. These spacecraft include missions dedicated to the study the solar wind (e.g., Helios; Musmann et al., 1975; Schwenn et al., 1975) and planetary missions to Mercury (e.g., *Mercury Surface, Space Environment, Geochemistry, and Ranging* or MESSENGER; Solomon et al., 2007) or Venus (e.g., *Venus Express* or VEX; Svedhem et al., 2007). Planetary orbiters usually spend some part of their orbit outside of the planet's magnetic obstacle, exposing their instruments to the solar wind. Data from Helios have been used to study the properties of ICMEs between 0.3 and 1 AU (e.g., Bothmer and Schwenn, 1994, 1998), and data from MESSENGER and/or VEX during opposition periods with spacecraft at 1 AU have been used to study how ICMEs evolve in the inner heliosphere (e.g., Good et al., 2018; Janvier et al., 2019; Paper V).

The second approach consists of so-called *heliospheric imaging*, i.e. of white-light

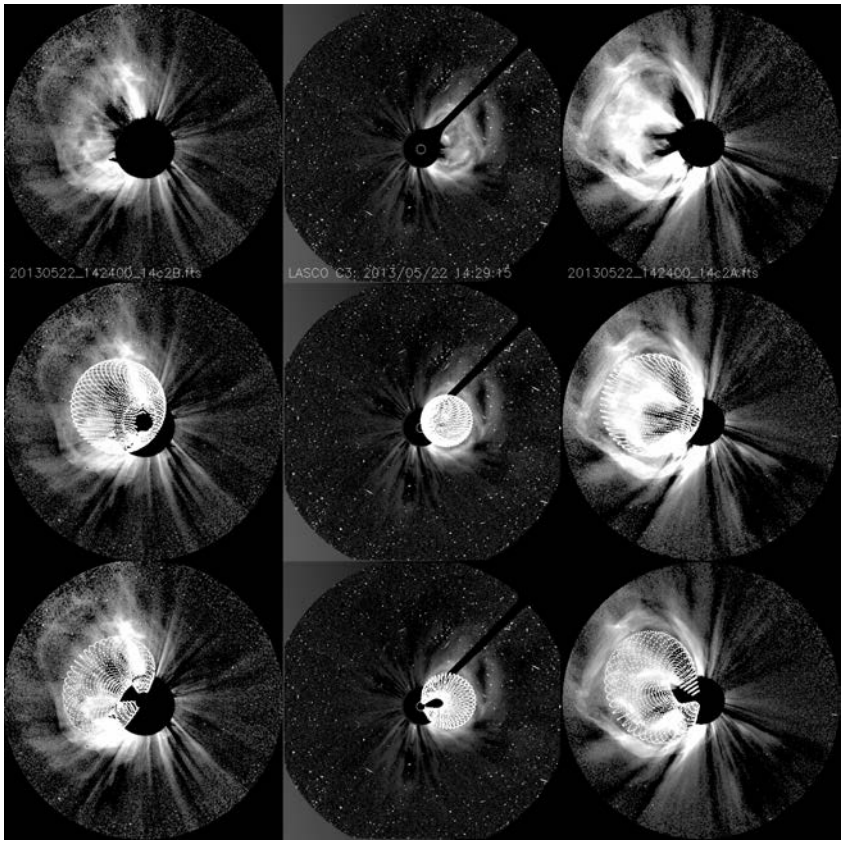

Figure 3.4: Stereoscopic reconstructions of a CME that erupted on 22 May 2013 from three viewpoints: STEREO/SECCHI/COR2-B (left column), SOHO/LASCO/C3 (middle column), and STEREO/SECCHI/COR2-A (right column). The top row shows plain base-difference images, the middle row shows the ice-cream/cone model overlaid, and the bottom row shows the GCS model overlaid. Adapted from Paper IV.

imaging of the heliosphere. The first such images were taken in the early 2000s with the *Solar Mass Ejection Imager* (SMEI; Eyles et al., 2003), which observed interplanetary space from Earth's orbit. It was through the *Heliospheric Imager* (HI; Eyles et al., 2009) instruments onboard the STEREO spacecraft, however, that the first white-light images taken away from the Sun–Earth line were possible. HI imaging techniques detect photospheric light scattered by electrons (K-corona) and dust (F-corona), with further contributions from starlight and other sources. Similarly to CME observations

in white light with coronagraphs, CMEs are observed in HI cameras by separating the contribution coming from electrons only. The top panels of Figure 3.5 show a series of Earth-directed CMEs observed by HI in running-difference images that are created by subtracting from each image its previous image. The lower panels present the same CMEs tracked in time–elongation maps (Sheeley et al., 2008; Davies et al., 2009) produced from running-difference HI images. Elongation here means the angle between the line from the observer to centre of the Sun and the LOS, and time–elongation maps are created by stacking intensity slices at a fixed position angle. In such maps, a propagating structure such as a CME appears as bright front followed by a dark front, due to the increase and subsequent decrease in density. This allows features to be tracked in elongation as a function of time and to determine their speed and propagation direction. After the launch of the STEREO spacecraft, many studies have focussed on connecting Earthbound CME–ICME pairs through HI (e.g., Savani et al., 2012; Möstl et al., 2014; Srivastava et al., 2018; Paper IV).

However, when studying features observed in the HI cameras, it is worth to keep in mind that, usually, the sheath region ahead of the CME is being tracked rather than the CME front itself (e.g., Paper IV). This is because plasma accumulates at the CME front with distance from the Sun, and consequently, sheath regions usually appear considerably denser than the driving CMEs by the time they are detected in the HI cameras (e.g., Lugaz et al., 2005; DeForest et al., 2013). Finally, another limitation is given by the fact that HI observations can provide information about the CME kinematics, but not about their magnetic field structure or magnitude.

3.3 CME arrival at 1 AU

During their journey through the heliosphere, CMEs eventually reach Earth's orbit at 1 AU. When detected by in-situ spacecraft, ICMEs can present a variety of properties and features, both in the sheath region and in the following ICME ejecta.

3.3.1 Sheath regions

When a CME is detected in situ, the first features that appear in the spacecraft data are the CME-driven interplanetary shock (if the CME is driving one) and the following sheath region. Interplanetary shocks driven by CMEs are fast-forward shocks, meaning

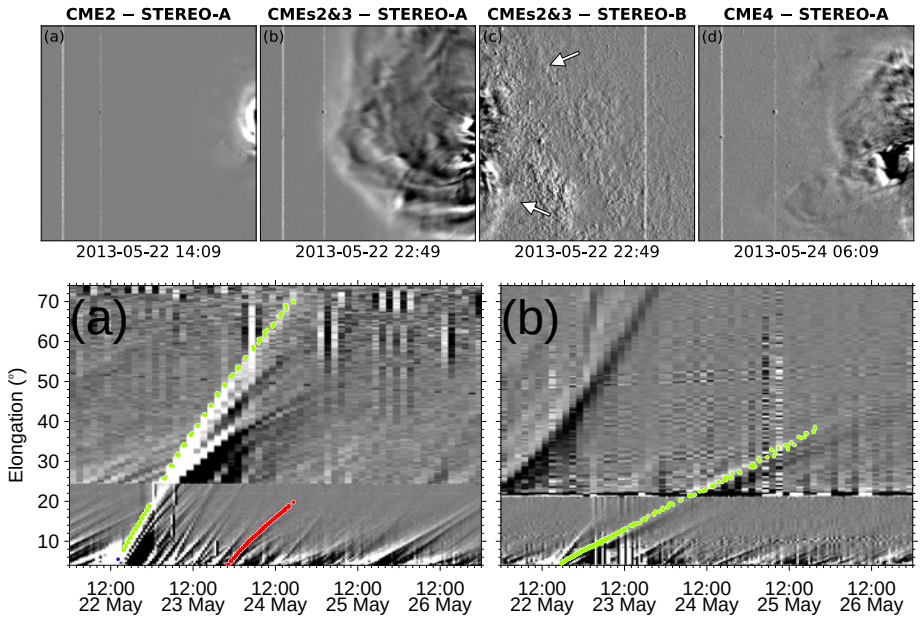

Figure 3.5: Top panels: A series of CMEs observed with STEREO/SECCHI/HI1-A and -B, shown in running-difference images. Bottom panels: The same CMEs (CME2 = blue, CMEs2&3 = green, and CME4 = red) tracked in time–elongation maps using the HI1 and HI2 cameras from STEREO-A (left) and STEREO-B (right). The elongation of Earth is about 20° in both spacecraft. Adapted from Paper IV.

that they can be recognised by a sharp and simultaneous increase in the magnetic field magnitude, solar wind speed, density, and temperature. Figure 3.6 presents a sheath region observed in May 2002 as an example, showing the major characteristics of a classic CME-driven sheath: shocked and piled-up (compressed) plasma and magnetic field ahead of an ejecta, enhanced and turbulent magnetic field, and high plasma density and temperature in comparison to the ambient solar wind.

At a first glance, the magnetic field in sheath regions may appear highly chaotic and unorganised as a result of the turbulence formed in shocked plasma, but some organised structures have been observed. Such structures are known as *planar magnetic structures* (PMSs; e.g., Jones et al., 2002; Kataoka et al., 2005; Savani et al., 2011; Paper I) and they correspond to periods in the solar wind in which the IMF vectors are nearly parallel to a single plane, but highly variable in both magnitude and direction within

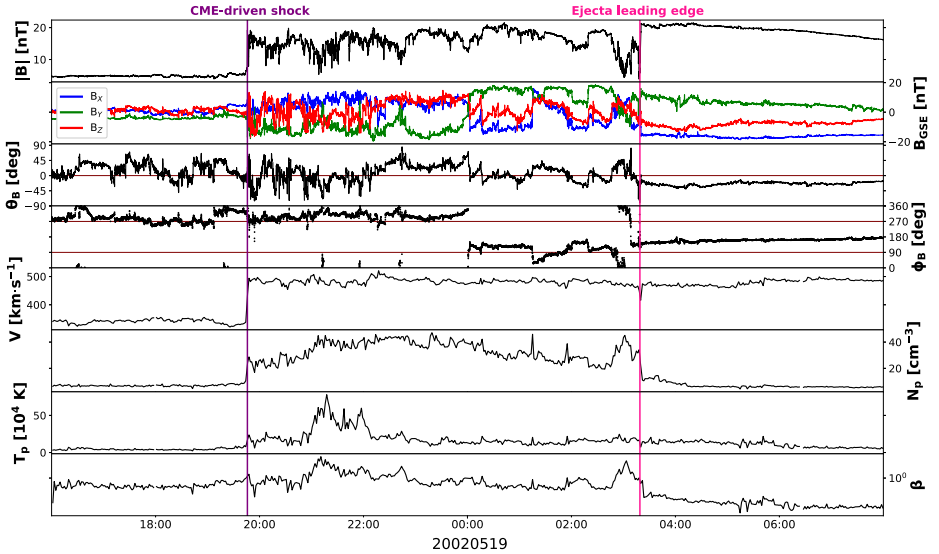

Figure 3.6: Example of a sheath region observed by *Wind* during May 2002. The parameters shown are, from top to bottom: magnetic field magnitude, magnetic field components in cartesian coordinates, θ and ϕ angles of the magnetic field, solar wind speed, proton density, proton temperature, and plasma beta. The sheath region lies between the two vertical lines that mark the CME-driven shock (in purple) and the ejecta leading edge (in pink). This plot is an updated version from a figure shown in Paper I.

that plane (e.g., Nakagawa et al., 1989; Nakagawa, 1993). Paper I showed that PMSs are a common phenomena in CME-driven sheath regions, being present in 85% of the sheaths and often spanning over two-thirds of the whole sheath duration.

The left panel of Figure 3.7 shows a schematic representation of how PMSs are organised in a sheath region. Possible mechanisms leading to the formation of PMSs in CME-driven sheaths are the alignment of discontinuities at the CME shock resulting from compression (Jones et al., 2002) and the draping of the IMF ahead of an ejecta as it propagates through the solar wind (Farrugia et al., 1990). Paper I showed that, in most cases, it is likely that both processes contribute to the formation of PMSs, the first favouring planarity close to the shock and the second close to the ejecta leading edge. The right panel of Figure 3.7 (from Paper I) shows how PMSs can be visualised in so-called θ–ϕ diagrams, where the IMF latitudinal (θ) and longitudinal (ϕ) angles

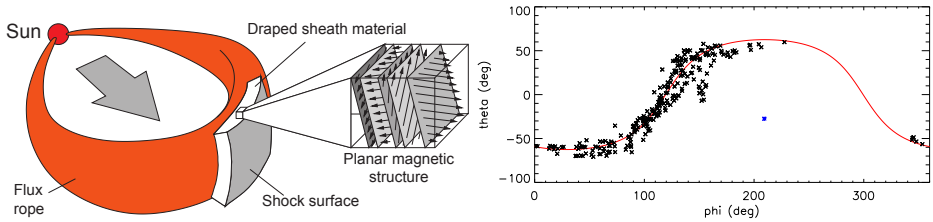

Figure 3.7: Left panel: Idealised representation of the formation of PMSs in the sheaths ahead of CMEs as a result of magnetic field draping. Adapted from Jones et al. (2002). Right panel: Example of a PMS visualised in a θ–ϕ diagram. The direction normal to the PMS plane (indicated by the red curve) is displayed by the blue star symbol. The black scatter points are the magnetic field vectors observed by *Wind* within the sheath region following an interplanetary shock in January 1997. Reproduced from Paper I.

are distributed in close proximity to a specific curve representing the PMS plane.

3.3.2 ICME ejecta

After a spacecraft has encountered a CME-driven shock and the following sheath region, there are two possible scenarios. In some cases, the spacecraft will find itself back into the ambient solar wind because most or all of the CME is missed. This may happen because interplanetary shocks and the following disturbed fields and plasma occupy a larger spatial extent than the driving CME (e.g., Wood et al., 2012). It has been in fact suggested that a majority, if not all *driverless interplanetary shocks* (i.e., whose driver cannot be identified from in-situ measurements) are related to CMEs (Gopalswamy et al., 2010; Janvier et al., 2014). In the rest of the cases, the sheath will be followed by the actual ICME ejecta.

Although CMEs are known to erupt as flux ropes from the Sun, not all ICME ejecta detected in situ present a flux rope structure (flux ropes are seen in about one-third of the cases; e.g., Gosling, 1990; Richardson and Cane, 2004; Huttunen et al., 2005). Flux rope ejecta are also known as *magnetic clouds* and they were first introduced by Burlaga et al. (1981). Magnetic clouds are characterised by enhanced magnetic field magnitudes, a smooth rotation of the magnetic field direction over a large angle, and low temperatures (e.g., Burlaga et al., 1981; Rodriguez et al., 2016). Having in mind the simplified flux rope representation shown in Figure 3.2, the magnetic field

direction that exhibits a smooth rotation (and a change of sign) would correspond to the helical field, whilst the direction that does not change sign would represent the axial field. As a first-order approximation, flux ropes in interplanetary space can be considered as cylindrically symmetric and force-free structures, where the electric current density depends linearly on the magnetic field, i.e., $\nabla \times \mathbf{B} = \alpha \mathbf{B}$, where $\mathbf{B}$ is the magnetic field and α is a constant (Goldstein, 1983; Burlaga, 1988). It has become a standard practice to fit the large-scale helical magnetic field variations observed by a spacecraft during a flux rope passage using analytical flux rope models (e.g., Lepping et al., 1990; Farrugia et al., 1999; Owens et al., 2006; Isavnin et al., 2011; Hidalgo and Nieves-Chinchilla, 2012; Nieves-Chinchilla et al., 2018), many of them considering also non-force-free effects and non-cylindrical cross-sections. These models give information on flux rope properties such as their chirality, axis orientation, and crossing distance from the flux rope axis.

On the other hand, ICME ejecta that do not contain a flux rope are known as *complex ejecta* and are characterised by more complicated magnetic field configurations and a lack of internal field rotation. The current consensus is that all CMEs contain in principle a flux rope, but a flux rope may not be detected in situ because of interactions with the ambient solar wind (e.g., Odstrcil and Pizzo, 1999; Savani et al., 2010; Manchester et al., 2017) or with other CMEs (e.g., Burlaga et al., 2002; Manchester et al., 2017), erosion of the magnetic flux (e.g., Dasso et al., 2007; Ruffenach et al., 2012), and/or the particular spacecraft path through the CME body (e.g., Cane et al., 1997; Jian et al., 2006a; Kilpua et al., 2011).

Figure 3.8 shows examples of a magnetic cloud (left panel) and a complex ejecta (right panel). The flux rope type of magnetic clouds can be estimated from visual inspection of magnetic field data, if the helical and axial components are clear enough to be discerned, and/or by applying in-situ flux rope reconstruction techniques such as the ones listed above. In the case of the magnetic cloud shown in Figure 3.8, the helical component rotates from North to South and the axial component points towards the West, making the flux rope a NWS-type. Since complex ejecta are not seen to contain a flux rope, it is usually not possible to associate them to a flux rope type. The complex ejecta shown in Figure 3.8 is likely the result of the interaction of at least three separate CMEs (see Section 4.4.2 for a discussion on CME–CME interaction).

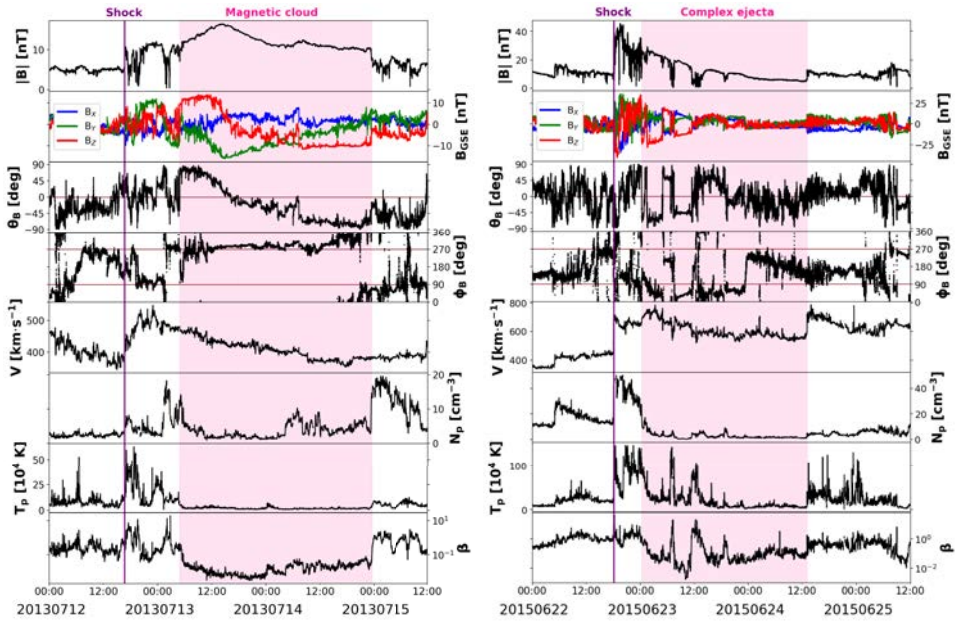

Figure 3.8: Two ICMEs observed at Earth's Lagrange L1 point by *Wind*. Left panel: A magnetic cloud observed during July 2013. Right panel: A complex ejecta observed during June 2015. The parameters shown are, from top to bottom: magnetic field magnitude, magnetic field components in cartesian coordinates, θ and ϕ angles of the magnetic field, solar wind speed, proton density, proton temperature, and plasma beta. The CME-driven shock is marked with a purple vertical line and the ICME ejecta is shaded in pink in both panels.

4 Forecasting CME-driven disturbances

♪ *We touched the Sun* – Gary Allan

Despite decades of research through theoretical, observational, and modelling efforts, the ability to forecast reliably the geoeffectiveness of CMEs and their properties in the near-Earth solar wind is still rather modest. The first problem is related to the *hit/miss* issue, i.e. wheter an ICME will encounter Earth at all (e.g., Möstl et al., 2014; Mays et al., 2015; Wold et al., 2018) and whether the hit will be a central one or a skimming encounter. Once established that a CME will result in an impact, the main challenges are related to determining *when* and *at which speed* the impact will take place (e.g., Odstrcil, 2003; Vršnak et al., 2013) and the duration and magnitude of *southward-directed magnetic field* periods following the impact (e.g., Savani et al., 2015, 2017; Kay et al., 2017). This chapter reviews the major issues and challenges regarding CME forecasting and the related results presented in the papers that form this thesis.

4.1 Shock arrival time

Since CMEs often drive interplanetary shocks during their journey from the Sun to 1 AU, a major goal in space weather forecasting is to establish if, when, and at which speed a shock will reach Earth. These parameters are important because fast shocks are associated with high ram pressure that can abruptly compress the magnetopause (see Section 2.3.2) and because the turbulent magnetic fields following the shock may carry sustained and strong southward components. The methods used in the papers that form this thesis to study and forecast the arrival of interplanetary shocks are briefly reviewed here.

4.1.1 HI reconstructions

As introduced in Section 3.2.2, HI data can be used to track shock fronts preceding dense sheath regions as they propagate through the heliosphere. Structures that appear in HI, however, are subject to strong projection effects that arise when making

observations out to large elongation angles via Thomson scattering (e.g., Howard and DeForest, 2012; Harrison et al., 2017). Hence, techniques have to be used to resolve the shock front in 2D from tracks made using time–elongation maps (e.g., see Figure 3.5). One such technique is the Self-Similar Expansion (SSE; Davies et al., 2012) model, which represents the CME (or shock) front as a circle with a constant half-width that propagates radially and with a constant speed. The STEREO mission has provided simultanous HI observations from two viewpoints, which have enabled stereoscopic observations. The two-spacecraft version of the SSE model, called Stereoscopic Self-Similar Expansion (SSSE; Davies et al., 2013) model, allows to derive the position of the apex of the tracked feature as a function of time from stereoscopic observations and to interpolate its propagation, obtaining therefore an arrival time and speed at Earth. Figure 4.1 shows an example of a shock front that was tracked in Paper IV resolved in 2D using the SSSE model.

The half-width that is inserted in the (S)SSE model can be obtained from remote-sensing observations, e.g. from stereoscopic reconstructions of the CME or the CME-driven shock using the GCS fitting technique on coronagraph data (e.g., Paper IV). However, it is important to note that in HI imagery the shock front ahead of the sheath is being tracked rather than the ejecta leading edge; therefore, a half-width that is larger than the CME half-width should be used (e.g., Paper IV). A limitation of (S)SSE reconstructions is given by the rigid, circular front that is assumed in the model, which may result in large errors associated with the shock parameters at Earth. CMEs and their associated shocks tend to flatten their front during interplanetary propagation due to solar wind drag (e.g., Vršnak et al., 2013), hence HI-based reconstructions based on an elliptical front would be more suitable (e.g., Rollett et al., 2016).

4.1.2 Heliospheric modelling

Another useful means to forecast the arrival of CME-driven shocks at Earth is given by 3D heliospheric modelling. Models such as Enlil (Odstrcil, 2003) or European Heliospheric Forecasting Information Asset (EUHFORIA; Pomoell and Poedts, 2018) are based on the ideal MHD equations that are solved for plasma mass, momentum, energy density, and magnetic field. Both models are composed of a coronal part, which is usually driven by a Wang–Sheeley–Arge (Arge et al., 2004) empirical model that feeds the background wind parameters and extends up to 21.5 $R_\odot$, and a heliospheric part,

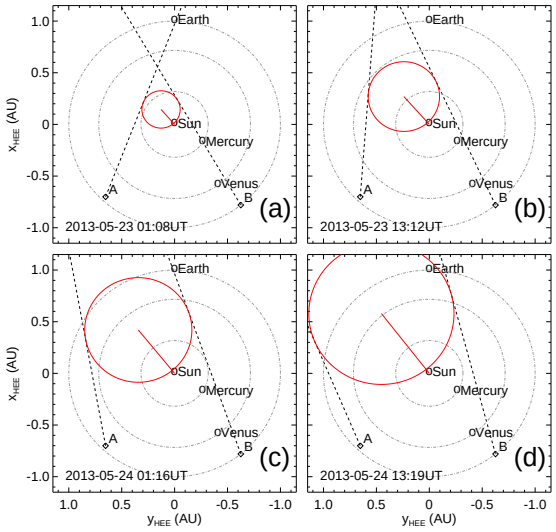

Figure 4.1: Schematic representation of SSSE fitting applied to the front associated with a CME analysed in Paper IV using HI. (a–d) The position of the front within the ecliptic plane (red) is triangulated from the observed leading edge in the HI cameras (dashed lines). The position of the CME at 12 hour intervals is shown in the successive panels (a) to (d). The half-width of the shock front is here assumed to be 69°. The labels 'A' and 'B' represent the STEREO-A and STEREO-B spacecraft, respectively.

which allows to propagate CMEs through solar wind from 21.5 $R_\odot$ onwards. Because the EUHFORIA model has been used in the work performed for this thesis, the rest of this section will mainly focus on EUHFORIA. In the simplest version of EUHFORIA, CMEs are launched employing the cone model described in Section 3.2.1, i.e. as spherical homogeneous structures without any internal magnetic field (e.g., Pomoell and Poedts, 2018; Scolini et al., 2018; Paper IV; Paper V). Under these assumptions and under certain conditions, a shock wave may form ahead of a CME during its propagation. Due to the magnetic field being that of the ambient wind, the cone model is not suitable to study the magnetic structure of ICMEs, but it can be applied to evaluate how CMEs propagate and their arrival times. Figure 4.2 shows an example of four CMEs modelled with EUHFORIA and studied in detail in Paper IV. The EUHFORIA time series (depicted in blue) show a number of peaks that correspond to the shock

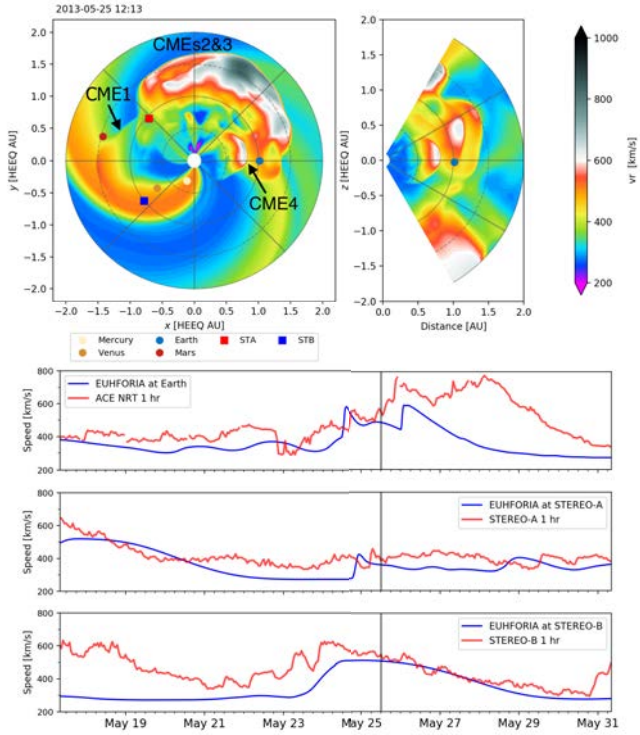

Figure 4.2: Example of four CMEs modelled with EUHFORIA using the cone model. Top panels: snapshot of the heliographic equatorial plane (left) and the meridional plane that contains Earth (right). Bottom panels: comparison of the EUHFORIA time series (blue) with in-situ measurements (red) from ACE, STEREO-A, and STEREO-B, during the computational domain. Adapted from Paper IV.

arrivals at 1 AU. The CME parameters needed for the cone model, i.e. latitude, longitude, half-angle, and speed, can be estimated from coronagraph observations and from reconstructions such as the GCS fitting introduced in Section 3.2.1 (e.g., Lee et al., 2013; Paper IV; Paper V).

Typical uncertainties associated with heliospheric models are of the order of a few hours (e.g., Riley et al., 2018; Wold et al., 2018), mostly attributable to the modelled background wind and to the initial CME parameters derived from remote-sensing observations. Indeed, the ambient wind depends highly on the initial magnetogram

used to drive the coronal model, and the resulting background is evolved to a steady state. This means that the heliospheric background structure cannot account for the time-dependent evolution of the sources of the solar wind (e.g., coronal holes or helmet streamers). Nevertheless, 3D MHD heliospheric models remain a valid and useful tool in space weather forecasting, especially because of their global coverage of the heliosphere that allows to evaluate relatively quickly the impact of CMEs at any heliolongitude (e.g., Witasse et al., 2017; Lee et al., 2018; Paper IV).

4.2 Sheath magnetic fields

The magnetic fields embedded in CME-driven sheath regions are of high importance for space weather forecasting, since they are able to cause significant disturbances in the geomagnetic field (e.g., Tsurutani et al., 1988; Gonzalez et al., 1999, 2011; Huttunen et al., 2002; Huttunen and Koskinen, 2004; Lugaz et al., 2016). However, the properties of sheath regions when they impact Earth and their geoeffectiveness are even more challenging to predict than properties of ICME ejecta. This is because sheaths do not begin their interplanetary journey as coherent structures and because the solar wind tends to both deflect sideways away from the CME nose and to pile up ahead of the driving CME (Siscoe and Odstrcil, 2008). As a result, sheath magnetic fields are usually highly variable and turbulent. A critical aspect of their geoeffectiveness, however, is their ability to carry strongly southward fields. Two mechanisms have been proposed to generate out-of-ecliptic fields in sheath regions: compression of pre-existing southward IMF fields at the CME-driven shock and draping of the magnetic field ahead of the CME ejecta (e.g., Gonzalez et al., 1994; Kataoka et al., 2005; Liu et al., 2008). As discussed in Section 3.3.1, Paper I demonstrated that these are also the mechanisms that result in the formation of PMSs in sheath regions. It is thus natural to assume that PMSs would be suitable regions for out-of-ecliptic fields. Figure 4.3 from Paper I shows the fraction of southward B_Z in three different sheath sub-regions (near the shock, in the middle of the sheath, and near the ejecta leading edge, each spanning 33% of the sheath) for planar and non-planar parts of the sheath.

It is clear from Figure 4.3 that planar parts of the sheath tend to contain a higher amount of southward fields, and that the difference between planar and non-planar parts is more pronounced for strongly southward fields, i.e. $B_z < -10$ nT. Paper I thus demonstrated that regions of the sheath that contain PMSs tend to exhibit a

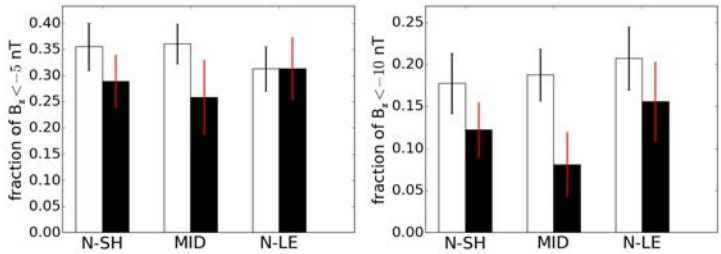

Figure 4.3: Relationship between PMS occurrence and negative B_z, i.e. southward periods of the north–south IMF component, in different sheath sub-regions (N-SH = near shock, MID = middle of the sheath, and N-LE = near ejecta leading edge) for a sample of 95 sheaths. The white bars represent planar regions, the black bars represent non-planar regions, and the error bars show the extent of one standard deviation. Left panel: Fraction of sub-region covered by $B_z < -5$ nT. Right panel: Fraction of sub-region covered by $B_z < -10$ nT. Reproduced from Paper I.

higher amount of out-of-ecliptic fields and are thus expected to be more geoeffective.

However, CME-driven sheath regions have been studied significantly less than ICME ejecta, and their real-time prediction remains very little explored in space weather forecasting. Recent developments regarding this issue involve modelling magnetised CMEs in heliospheric simulations (see Section 4.3.2 for additional details).

4.3 Flux rope type

The flux rope structure of CMEs is a key parameter that determines their ability to drive geomagnetic storms (e.g., Huttunen et al., 2005; Zhang et al., 2007; Richardson and Cane, 2012; Paper III). In order to be able to forecast the magnetic fields embedded in an interplanetary flux rope (or magnetic cloud, see Section 3.3.2), it is important to know what is the initial (or intrinsic) flux rope type, how the CME flux rope will evolve in interplanetary space, and what section of the flux rope will intersect Earth. This section summarises the main findings and implications reported in the articles that form this thesis and how such information can be used to improve current forecasting capabilities.

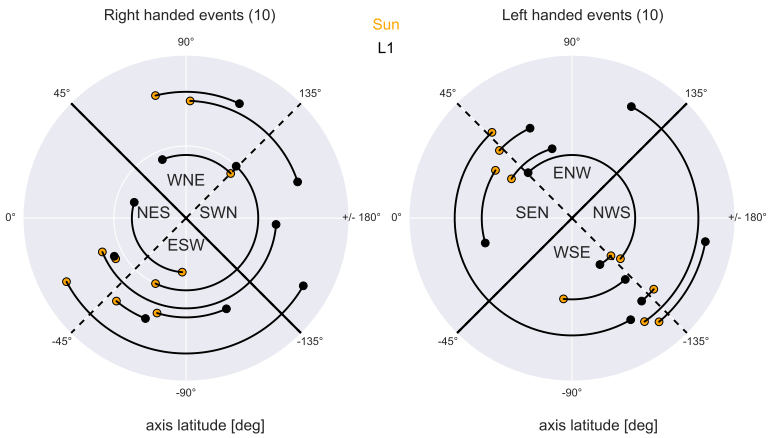

Figure 4.4: Change in the flux rope axis direction (shown as a clock angle) from the Sun to L1, divided into right- and left-handed events. The clock angle at the Sun is shown in yellow, whilst the angle at L1 is shown in black. The curve connecting the clock angles is taken as the shortest path between solar and in-situ axis directions, i.e., clockwise and counterclockwise rotations depending on chirality are not considered. Reproduced from Paper III.

4.3.1 Solar versus in-situ flux rope type

In Paper II, the intrinsic flux rope type of CMEs was determined using the indirect methods summarised in Section 3.1.2 and compared to the magnetic structure of the corresponding flux rope detected in situ near Earth. This was done in Paper III for 20 CME events that could be uniquely linked to their in-situ counterparts from the Sun to Earth using heliospheric imaging (using time–elongation maps described in Section 3.2.2). Whilst the chirality of all the CME–ICME pairs was conserved, as expected for a force-free magnetic field configuration (Woltjer, 1958), this was not always true for the flux rope type. Figure 4.4 shows how the magnetic field direction at the flux rope axis, and as a consequence the flux rope type, changed from the Sun to Earth for the 20 CMEs investigated in Paper III. It is evident from Figure 4.4 that the knowledge of the intrinsic flux rope type alone is not sufficient for predicting the flux rope magnetic fields in situ, since 35% of the events were reported to change their orientation by more than 90°.

Differences between the flux rope type estimated at the Sun and the one observed

in situ can arise from several mechanisms that are related to CME evolution in the corona and in the heliosphere. CMEs may experience deflections (e.g., Wang et al., 2014; Kay et al., 2015, 2016), rotations (e.g., Möstl et al., 2008; Vourlidas et al., 2011; Isavnin et al., 2014), and/or deformations (e.g., Owens, 2008; Savani et al., 2010) after leaving the Sun. The most dramatic evolution is expected to take place close to the Sun (below $30\,R_{\odot}$), but there are cases where significant deflection and rotation happens between $30\,R_{\odot}$ and 1 AU (Isavnin et al., 2014). Another factor that may contribute to discrepancies between solar and in-situ structures is given by local deformations that deviate from the ideal flux rope configuration. It was shown by Owens et al. (2017) that CMEs cease do be coherent MHD structures beyond 0.3 AU, thus local deformations would not be able to propagate through the whole CME body. Observational studies also support the view that not all flux ropes are coherent structures and that their properties may change considerably over relatively small longitudinal separations (e.g., Möstl et al., 2012; Lugaz et al., 2018). Furthermore, Bothmer and Mrotzek (2017) demonstrated that pre-existing kinks in the CME source region are maintained in the flux rope structure during its eruption and propagation.

Nevertheless, knowledge of the intrinsic flux rope type is an important aspect to take into account in space weather forecasting, as the magnetic structure at the Sun can be used as input for CME evolution models. An example showing the utility of remote-sensing observations of the solar disc is presented in Section 4.3.2, where magnetised CMEs in heliospheric modelling are briefly discussed.

4.3.2 Modelling magnetised CMEs

Recent efforts in 3D heliospheric modelling have focussed on the introduction of magnetised structures within CMEs, in order to enable analysis and prediction of the magnetic field components (and in particular B_Z) embedded in a CME. EUHFORIA has implemented a spheromak (e.g., Shiota and Kataoka, 2016) CME model, where CMEs exhibit a toroidal-like flux rope structure (Scolini et al., 2019; Verbeke et al., 2019). In addition to the cone model input parameters described in Section 4.1.2, the spheromak model requires as additional parameters chirality, tilt of the CME axis, and magnetic flux.

The chirality of CMEs can be determined from observations of their solar source using the methods described in Paper II (see Section 3.1.2), since magnetic helicity is a

conserved quantity. The axis tilt can be estimated as a first-order approximation from solar observations using the orientation of the PIL and PEAs (Paper II; Paper III). Solar observations, however, are not sufficient to describe the early evolution of CMEs (as demonstrated in Paper III); hence, the tilt angle can be alternatively determined from coronagraph data taken as close as possible to the model's heliospheric inner boundary at 21.5 $R_\odot$ and using fitting procedures as the GCS reconstruction described in Section 3.2.1. Finally, the magnetic flux embedded in the erupting CME can be estimated from the magnetic field that lies under the PEAs (Gopalswamy et al., 2017) or the flare ribbons (Kazachenko et al., 2017), which are believed to mark the area where magnetic reconnection has occurred during an eruption.

Figure 4.5 shows as an example a CME that was analysed at the Sun and in situ near Earth in Paper III and that was modelled using both the cone and the spheromak models in EUHFORIA by Scolini et al. (2019). It is possible to note in the right panel of Figure 4.5 that the simulations that use a spheromak model (in yellow and red) are able to reproduce both a sheath region and a flux rope ejecta, in contrast with the cone model simulation (in blue) that is able to reproduce the CME-driven shock only.

4.4 Multiple CMEs

Section 4.3 has focussed on single-CME events, but cases in which two or more CMEs are directed towards Earth more or less at the same time are not infrequent, especially during solar maximum when several CMEs per day are launched (e.g., Webb and Howard, 1994). The eruption of a series of CMEs may result from *sympathetic eruptions* (e.g., Török et al., 2011; Lynch and Edmondson, 2013), where one eruption triggers another, from *homologous CMEs* (e.g., Paper V), where several CMEs erupt from the same source region, or from two or more unrelated eruptions. Such multiple-CME events can be distinguished into *successive CMEs*, where several CMEs are launched close in time without reaching each other, and *interacting CMEs*, where two or more CMEs interact during their interplanetary journey. This section provides a brief overview of both phenomena.

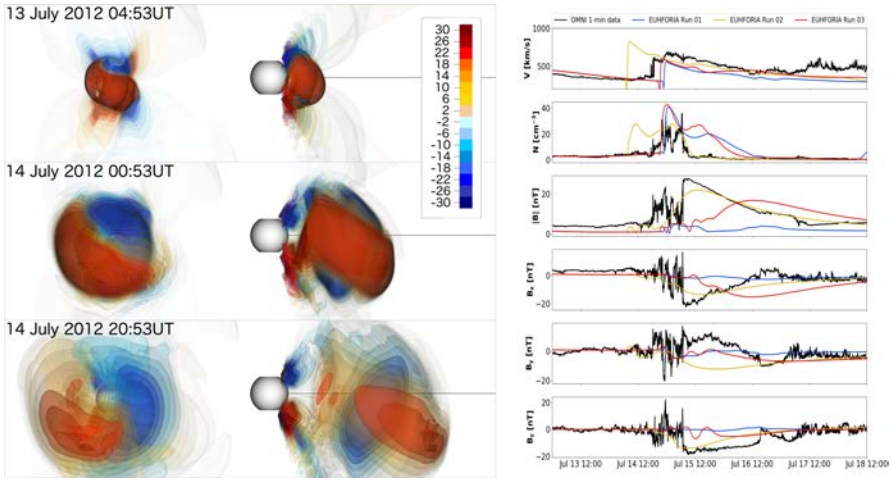

Figure 4.5: Heliospheric modelling of one of the CMEs analysed in Paper III using EUHFORIA with a spheromak flux rope. Left panel: Visualisation of the CME B_Z for EUHFORIA Run #3, shown in the right panel in red, at three different times. Each row shows Earth and quadrature perspectives. Right panel: EUHFORIA time series at Earth compared with OMNI data for three different runs (Run #1 = cone, Run #2 and Run #3 = spheromak). From top to bottom: solar wind speed, number density, magnetic field magnitude, and magnetic field cartesian components. Adapted from Scolini et al. (2019).

4.4.1 Successive CMEs

When a series of CMEs are launched from the Sun close in time but without ever reaching each other, the presence of multiple CMEs does not affect the magnetic structure (in terms of direction of the embedded magnetic fields) that will be observed in situ. The preceding CMEs, however, affect significantly the arrival time and the magnetic field magnitudes of the following CMEs. The *solar wind preconditioning* phenomenon has been reported in several studies (e.g., Liu et al., 2014; Temmer and Nitta, 2015), meaning that the solar wind where the following CME is propagating through is "swept up" by the previous CME. A preconditioned solar wind appears more rarefied, allowing a trailing CME to propagate faster because of its weaker drag. Furthermore, Liu et al. (2014) have demonstrated that solar wind preconditioning is a favourable phenomenon for the formation of "perfect storms" near 1 AU, especially because a fast CME moving through a rarefied and stretched ambient wind would result in an enhanced magnetic

field as fast propagation inhibits expansion.

An example of CME propagating through a preconditioned solar wind was reported in Paper IV (i.e., the structure marked as CME4 in the EUHFORIA simulation shown in Figure 4.2). Such CME arrived at Earth before one would expect in the case of a single CME because of the presence of a large and relatively fast CME preceding it (i.e., the structure marked as CMEs2&3 in the EUHFORIA simulation shown in Figure 4.2).

4.4.2 Interacting CMEs

The eruption of a series of CMEs close in time may result, in some cases, in CME–CME interaction in interplanetary space (e.g., Lugaz et al., 2017). The nature of each CME–CME interaction depends strongly on the kinematic and magnetic parameters of the interacting CMEs as well as their relative propagation directions (e.g., Schmidt and Cargill, 2004; Lugaz et al., 2013; Paper V). Possible outcomes are the formation of a complex merged structure where the interacting CMEs have lost their identities (Burlaga et al., 2002, see Section 3.3.2), compression of the preceding CME by the following one (Liu et al., 2014; Paper V), and/or coalescing of two or more CMEs into a single flux rope structure (Lugaz et al., 2013, 2017; Paper V). The corresponding CME-driven shocks may also interact in different ways, e.g. through two or more shocks interacting with each other or a shock interacting with an ejecta (e.g., Lugaz et al., 2017). In some cases (e.g., Lugaz et al., 2013; Paper V), the shock driven by the trailing CME may propagate all the way through the preceding ejecta and finally merge with the shock driven by the leading CME. In light of these aspects, it is clear that CME–CME interaction is an important issue in space weather forecasting, since it always leads to changes in general CME properties such as size, speed, magnetic field strength, and expansion rate and, thus, to higher degrees of unpredictability regarding CME evolution.

An example (from Paper V) of two CMEs interacting and merging in interplanetary space (between the orbits of Venus and Earth) is shown in Figure 4.6. In the plots, two flux ropes (marked as FR2, in blue, and FR3, in green) are seen to arrive at Venus as two mostly separate structures, whilst at Earth several interaction signatures can be observed. The shock driven by FR3 (marked as S3) has propagated through FR2, generating a double-shock signature ahead of it and likely accelerating the first ejecta (e.g., Lugaz et al., 2005). It is also possible to note that FR3 has compressed FR2

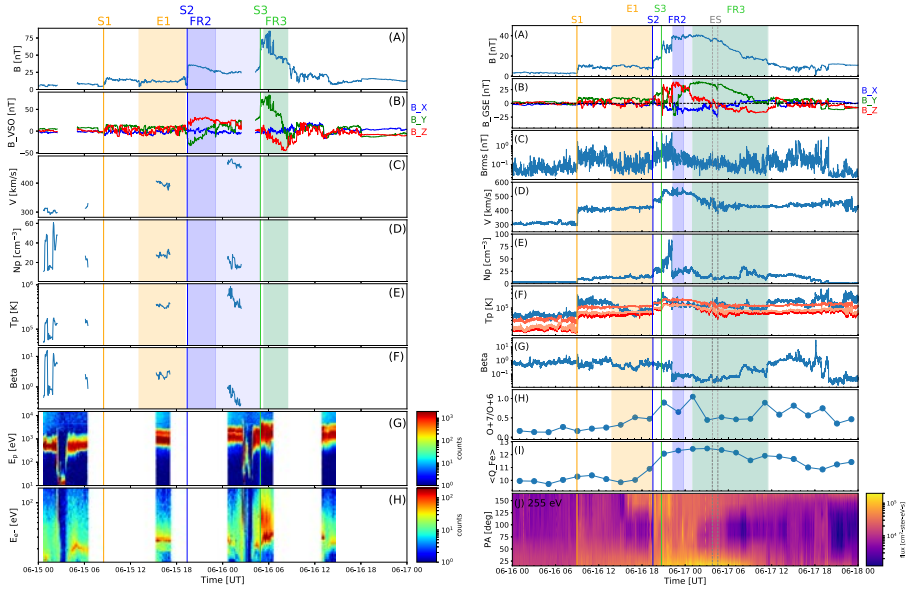

Figure 4.6: Example of successive/interacting CMEs (CME1 = orange, CME2 = blue, and CME3 = green) observed by VEX around Venus (left panel) and by *Wind* and ACE at Earth's Lagrange L1 point (right panel). The parameters shown in the left panel are, from top to bottom: magnetic field magnitude, cartesian components of the magnetic field, solar wind speed, proton density, proton temperature, plasma beta, proton counts, and electron counts. The parameters shown in the right panel are, from top to bottom: magnetic field magnitude, cartesian components of the magnetic field, root-mean-square magnetic field vector, solar wind speed, proton density, proton temperature, plasma beta, oxygen charge state ratio, average iron charge state, and pitch-angle spectrogram of suprathermal 255 eV electrons. The various interplanetary shocks are marked with a vertical line and an "S", the ejecta with an "E", and the flux ropes with the notation "FR". The interaction between FR2 and FR3 between Venus and Earth leading to the compression of FR2 and the formation of a single flux rope structure is evident in the two plots. Adapted from Paper V.

and enhanced its magnetic field, which does not appear to have declined during the journey from Venus to Earth (the leading edge magnetic field for FR2 is ∼35 nT at Venus and ∼39 nT at Earth). Finally, the interaction of FR2 and FR3 have created a single, merged flux rope structure near Earth, composed of a compressed FR2 and a relaxed FR3.

5 Concluding remarks and future challenges

♪ *Let the Sunshine in* – H.A.I.R.

In this thesis, the magnetic structure of CMEs and their related interplanetary structures has been studied in a space weather context. The overall goal of the project was to advance the current understanding of evolution of CMEs during their journey from the Sun to Earth. This thesis makes significant contributions to space weather forecasting through remote-sensing observations and in-situ measurements together with heliospheric modelling.

5.1 Main conclusions of the included papers

In Paper I, the magnetic structure of CME-driven sheath regions has been analysed in terms of their planarity. The paper shows that planar magnetic structures (PMSs) tend to form because of the alignment of the discontinuities downstream of the CME-driven shock and/or because of the draping of the magnetic field lines about the ICME ejecta. It was found that PMSs are more likely to produce long-lasting out-of-ecliptic magnetic fields that, as a consequence, increase sheath geoeffectiveness. These findings suggest that prior knowledge of the properties of the shock and ICME ejecta, e.g., from remote-sensing observations, provides paramount information for forecasting the geoeffectiveness of CME-driven sheath regions.

In Paper II, a combination of several indirect proxies from remote-sensing observations of the solar disc was used to determine the intrinsic flux rope type (i.e., the configuration of the axial and helical components of the magnetic field) of CMEs at the time of their eruption. The application of such methods to two case studies revealed that the flux rope type at the Sun matched well with the structures observed in situ near Earth. These conclusions suggest that solar observations are a good first-order approximation for what to expect in situ when forecasting CMEs.

In Paper III, the methods described in Paper II for determination of the intrinsic flux rope type were applied to 20 case studies, in order to determine the rate of "matches" between intrinsic and in-situ flux rope types. In agreement with Paper II, this paper

also implies that solar observations are an important first step for predicting the magnetic structure of in-situ flux ropes, but in some cases (35%) the orientations of the in-situ flux ropes disagreed with the corresponding solar estimates by over 90°, thus affecting significantly direct estimation of the geoeffectiveness of ICME ejecta. These findings suggest that the intrinsic flux rope type is a useful parameter to be used as input in CME modelling, and that CME evolution in the corona and heliosphere have to be taken into account for predicting reliably magnetic fields in Earth-impacting CMEs.

In Paper IV, a series of four CMEs were studied in terms of their impact at 1 AU. The events were selected because they were all relevant to the issue of forecasting "problematic CMEs", since they either erupted from the solar limb or because they were faint and ambiguous in coronagraph imagery. The CMEs were analysed remotely in the corona using multiwavelength (extreme ultraviolet, white light, and radio) observations from multiple vantage points and their impact at 1 AU was evaluated using heliospheric 3D modelling and imaging as well as in-situ measurements. In particular, the paper demonstrates the importance of heliospheric imaging for evaluating the Earth-directed components of CMEs that are propagating far from the Sun–Earth line or that are faint in the solar corona. The results presented in the paper highlight the importance of having a complete understanding of the whole heliospheric context when forecasting problematic events.

In Paper V, a series of three CMEs were studied in terms of their mutual interactions on their way from Sun to Earth. The presence of the *Venus Express* spacecraft orbiting Venus (that was almost radially aligned with Earth) was crucial for getting insights into the mechanism of CME–CME interactions. In particular, the second and third CMEs analysed in this study were just about to interact at the heliocentric distance of Venus (i.e., 0.72 AU), and their interaction had fully taken place when the merged structure reached Earth. The most interesting features reported in the paper are the fact that the merged CME was preceded by a double shock, suggesting that the shock driven by the following CME had propagated through the preceding one, and that the merged CME appeared as a single magnetic cloud by the time it impacted Earth. The results presented in the paper emphasise the complexity of interpreting interplanetary observations for CME–CME interaction events and suggest that considerable interaction can take place over relatively short distances ($\sim$0.3 AU in this case).

5.2 What to expect from the future

Although the field of space weather has progressed enormously during the last few decades, many aspects are still not fully understood and significant further advancements have to be made to achieve reliable predictions with sufficient lead times.

First of all, as emphasised in Paper IV and Paper V, continuous observations of the Sun, the corona, and the inner heliosphere away from the Sun–Earth line, e.g. from the Lagrange L5 point located $\sim 60^\circ$ to the east from Earth and/or the solar poles (e.g., Vourlidas, 2015; Gibson et al., 2018), would be hugely beneficial for space weather forecasting. Observations from such vantage points provide off-angle views of Earth-directed disturbances and allow following earthbound CMEs with higher accuracy than from Earth (i.e., with minimal projection effects). When coupled to remote-sensing observations from the L1 point, they also allow triangulation of the three-dimensional geometric and kinematic parameters of CMEs. Indeed, the potential of these aspects has been proven through the STEREO mission but, as the longitudinal separation of the STEREO spacecraft changes on their orbit around the Sun (by $\sim 22^\circ$ every year and, moreover, contact with STEREO-B was lost in 2014), they cannot be used for continuous space weather monitoring. Furthermore, solar disc measurements from L5 would allow observations of active regions, filaments, and other structures in the solar atmosphere well before they turn into Earth's view.

As remarked in Paper II and Paper III, current remote-sensing observation techniques do not allow direct measurement of coronal magnetic fields in a consistent manner that would enable regular utilisation for space weather forecasting. As discussed in Section 2.1.4, the biggest challenges in this regard are given by the fact that the corona is optically thin and relatively dim compared to the bright solar disc. As a consequence, quantitative information on the coronal magnetic field is currently derived from coronal models that are extrapolated from measurements of the lower atmospheric layers (Wiegelmann et al., 2017). A significant further improvement in forecasting CME magnetic fields would be given by continuous magnetic field measurements in the corona, in order to determine how the internal magnetic structure of CME flux ropes evolves due to interactions with the ambient corona and solar wind. The current and planned coronal polarimetric measurements are expected to shed a new light on this issue (Gibson et al., 2017b). For example, it has been shown that linear-polarisation observations of the off-limb corona can be used to quantify the magnetic topology and the open-field

radial expansion in the low corona (Gibson et al., 2017a). Alternatively, the magnetic field in the corona could be determined through measurements of the Faraday rotation of distant radio sources, e.g. pulsars (Howard et al., 2016). Both methods, however, are not currently used for systematic space weather forecasting. Coronal polarimetric measurements need larger and more precise telescopes in order to capture the weak signals coming from the corona, and Faraday rotation measurements need a well-known radio source constantly located behind the Sun in order to apply the technique.

Furthermore, as emphasised in Paper V, in-situ measurements taken in the inner heliosphere between the Sun and 1 AU are essential for understanding how CMEs evolve with radial distance. Excitingly, new measurements of the solar wind plasma and the IMF from various locations in the inner heliosphere will be available to the community in the near future, from e.g. Parker Solar Probe (PSP; Fox et al., 2016, launched in August 2018 to venture up to $\sim 9\,R_\odot$ distance from the Sun in a heliocentric orbit), BepiColombo (Benkhoff et al., 2010, launched in October 2018 towards Mercury), and Solar Orbiter (SolO; Müller et al., 2013, expected to be launched in February 2020 in a heliocentric orbit as close as $\sim 60\,R_\odot$ and with an orbital inclination up to $\sim 25°$). PSP and SolO are also equipped with solar disc and/or white-light imagers, thus observational data of the Sun and/or its atmosphere taken from up close (PSP) and from a significant inclination to the ecliptic plane (SolO) will bring new, valuable information and new perspectives on the early evolution of CMEs.

Finally, there are two main directions towards which future heliospheric modelling efforts shall be focussed. The first regards modelling of the solar wind background, which is currently treated as a static structure that corotates with the Sun. This assumption works as a first approximation to model the solar wind to relatively short heliocentric distances (e.g., 1 AU) and for short temporal domains, where no significant large-scale changes are expected to occur. A time-dependent solar wind, in turn, would take into account how the global structure of the solar magnetic field evolves with time, allowing to model CME propagation with higher accuracy and to larger heliocentric distances. The second aspect, on the other hand, regards modelling of the magnetic structure of CMEs. The spheromak model (see Section 4.3.2 and Figure 4.5) assumes the initial morphology of CMEs to consist of a cone with a spherical front, whereas the introduction of, e.g., a GCS-like (or croissant-like) morphology with an internal magnetic field (e.g., Gibson and Low, 1998; Titov and Démoulin, 1999; Isenberg and Forbes, 2007) would allow to model with higher accuracy a larger amount of

CMEs. In any case, magnetised CMEs in 3D heliospheric modelling need to be injected with realistic parameters that describe the initial flux rope structure and the early coronal evolution (i.e., how the CME is structured and oriented at the inner heliospheric boundary of the models). The observational methods described and used throughout this thesis can be used to constrain the intrinsic flux rope structure. Other techniques may involve, e.g., data-driven modelling (e.g., Wiegelmann, 2008; Fisher et al., 2015; James et al., 2018; Kilpua et al., 2019; Pomoell et al., 2019).

In conclusion, this is an exciting time in the fields of solar physics and space weather. The data that will be provided by the newest missions, coupled with innovative and refined forecasting models, have great potential to bring improvements and new knowledge on this fascinating topic.

6 Summary of papers and the author's contribution

♪ *Beyond the dark Sun* – Wintersun

This chapter consists of a summary of the articles included in this thesis, followed by a description of the author's contribution for each of them.

6.1 Paper I

Palmerio, E., Kilpua, E. K. J., and Savani, N. P.: Planar magnetic structures in coronal mass ejection-driven sheath regions, *Annales Geophysicae*, 34, 313–322, 2016.

Summary: This paper investigates planar magnetic structures (PMSs), which are solar wind structures where the IMF vectors are nearly parallel to a single plane, in CME-driven sheath regions. First, an automated algorithm for detecting PMSs using magnetic field data is presented and applied to 95 sheaths observed near Earth between 1997 and 2015. PMSs are found in 85% of the studied events, suggesting that they are common structures in CME sheaths. Successively, the sheaths are divided into groups according to their PMS occurrence and their magnetic field and plasma parameters are analysed. The results of the statistical analysis support two PMS formation mechanisms, namely compression and alignment of discontinuities at the CME shock and draping of the magnetic field about the CME ejecta. Finally, it is found that planar parts of sheaths tend to me more geoeffective than non-planar parts, as they are able to generate stronger, sustained out-of-the-ecliptic fields.
The author's contribution: Designed and coded the PMS detection algorithm, performed the analysis based on the output of the algorithm, led the interpretion of the results, wrote the manuscript.

6.2 Paper II

Palmerio, E., Kilpua, E. K. J., James A. W., Green, L. M., Pomoell, J., Isavnin, A., and Valori, G.: Determining the intrinsic CME flux rope type using remote-sensing solar disk observations, *Solar Physics*, 292:39, 2017.

Summary: The magnetic structure of CME flux ropes at the time of their onset is a crucial part of the evolutionary process of solar eruptions from the Sun to Earth. Knowledge of the "intrinsic flux rope type" can be used as input for CME propagation and space weather forecasting models, and can be used to observationally track CME evolution throughout the heliospheric domain. This paper aims to address this issue by collecting a number of techniques to apply to remote-sensing data in order to determine the magnetic structure of flux ropes at the Sun solely from solar disc observations. The parameters needed to reconstruct the intrinsic flux rope type are 1) chirality, 2) tilt of the flux rope axis, and 3) direction of the magnetic field at the axis. Chirality proxies include the analysis of magnetic tongues, sigmoids, coronal arcade skew, filaments, and other coronal and/or chromospheric features. The axis tilt is determined from the orientation of the PIL associated to the CME source region, and the direction of the magnetic field is extrapolated from the estimation of the flux rope footpoints. These remote-sensing techniques are applied to two case studies and the resulting intrinsic flux rope types are compared with measurements at 1 AU, showing good agreement between remote-sensing and in-situ observations.
The author's contribution: Selected the events to analyse, performed the remote-sensing and in-situ analysis of the events, led the interpretion of the results, wrote the manuscript.

6.3 Paper III

Palmerio, E., Kilpua, E. K. J., Möstl, C., Bothmer, V., James, A. W., Green, L. M., Isavnin, A., Davies, J. A., and Harrison, R. A.: Coronal magnetic structure of earth-bound CMEs and in situ comparison, *Space Weather*, 16, 442–460, 2018.

Summary: This work follows and expands the techniques presented in Paper II, with the aim to perform a small statistical study on flux ropes at the Sun and at Earth. 20 CMEs displaying a clear flux rope structure at 1 AU are connected to their solar counterpart and their flux rope type is estimated at both locations using the methods introduced in Paper II. One of the novelties compared to Paper II is that the dataset contains CMEs erupting from different kinds of source regions, incuding filaments on the quiet Sun. The comparison of the magnetic structure of the CMEs under study at the Sun and at Earth reveals that chirality is conserved for all events, whilst the orientation of the flux rope axis may change dramatically. It is found that the flux

rope type is maintained in only 20% of the cases, or 55% if intermediate cases (axis inclination close to 45°) are considered as a match. In 35% of the events under study, the discrepancies between on-disc and in-situ flux rope types exceed 90°. The results presented highlight the importance of determining the magnetic configuration of CMEs as they erupt from the Sun, but also remark that CME evolution has to be taken into account and estimated in order to forecast space weather events in a reliable way.
The author's contribution: Selected the events to analyse, performed the remote-sensing and in-situ analysis of the events, led the interpretion of the results, wrote the manuscript.

6.4 Paper IV

Palmerio, E., Scolini, C., Barnes, D., Magdalenić, J., West, M. J., Zhukov, A. N., Rodriguez, L., Mierla, M., Good, S. W., Morosan, D. E., Kilpua, E. K. J., Pomoell, J., and Poedts, S.: Multipoint study of successive coronal mass ejections driving moderate disturbances at 1 au, *The Astrophysical Journal*, 878:37, 2019.

Summary: The importance of forecasting space weather events is not related to extreme geomagnetic storms only. This paper aims to better understand so-called "problem storms", i.e. CMEs that are not conventional full halos erupting from close to the disc centre and that usually drive moderate space weather effects. Four successive CMEs that erupted during May 2013 and that impacted Earth and/or the STEREO-A spacecraft are investigated. The first three CMEs were limb events as seen from Earth and/or STEREO-A, whilst the fourth CME was not visible in coronagraph images from the spacecraft along the Sun–Earth line despite having erupted from close to the disc centre as seen from Earth. All the CMEs, however, caused moderate disturbances at 1 AU. The events are studied in detail through multipoint observations (in EUV, white light, and radio) and finally simulated using the EUHFORIA heliospheric model. It is demonstrated that, in the case of problematic and unclear CMEs, a multipoint and multi-instrument analysis may provide understanding of the whole heliospheric context and, consequently, help assess their geoeffectiveness.
The author's contribution: Designed the project, performed the remote-sensing and in-situ analysis, provided the input parameters for the simulation, interpreted the results, wrote most of the manuscript.

6.5 Paper V

Kilpua, E. K. J., Good, S. W., **Palmerio, E.**, Asvestari, E., Lumme, E., Ala-Lahti, M., Kalliokoski, M. M. H., Morosan, D. E., Pomoell, J., Price, D. J., Magdalenić, J., Poedts, S., and Futaana, Y.: Multipoint observations of the June 2012 interacting interplanetary flux ropes, *Frontiers in Astronomy and Space Sciences*, 6:50, 2019.

Summary: In this paper, a series of CMEs that erupted in June 2012 are analysed in terms of their propagation from the solar corona to Earth. Multipoint remote-sensing and in-situ observations are combined with heliospheric modelling in order to characterise the interplanetary evolution of the events under study. The CMEs were observed remotely on the solar disc, in coronagraphs, and in heliospheric imagers, and in situ at Venus and Earth (that were almost radially aligned during the period under study). Measurements at 0.72 and 1 AU show that the first CME arrived as a weak, complex ejecta at both locations, whilst the following two evolved significantly between the orbits of Venus and Earth. At Venus, the third CME was just about to subsume the second one, whilst at Earth the two CMEs looked like a single, coherent magnetic cloud preceded by a double shock signature. A deep analysis of in-situ data together with in-situ flux rope reconstructions reveals that the last CME had significantly compressed the preceding one, enhancing its fields and merging with it without significantly altering the magnetic structure of the two flux ropes considered separately. The results presented show that a complete understanding of CME–CME interactions may help in forecasting the geoeffectiveness of merged CMEs, as the events under study caused the highest magnetic field magnitudes reported during Solar Cycle 24.

The author's contribution: Analysed solar, coronagraph, and heliospheric remote-sensing data, analysed in-situ measurements around Venus, produced Figures 1 and 4, produced the HI movie and the Venus high-resolution plots included in Supplementary Material, contributed to deriving the input parameters for the simulation, contributed to the interpretation of the results, contributed to writing the manuscript.

References

Allen, J., Frank, L., Sauer, H., and Reiff, P. (1989). Effects of the March 1989 solar activity. *Eos Trans.*, 70:1479–1488.

Amari, T., Aly, J. J., Luciani, J. F., Mikic, Z., and Linker, J. (2011). Coronal Mass Ejection Initiation by Converging Photospheric Flows: Toward a Realistic Model. *Astrophys. J.*, 742(2):L27.

Ambastha, A. (2010). Solar Interior. *Astrophys. Space Sci. Proc.*, 18:15.

Andrews, M. D. (2001). Lasco and eit Observations of the Bastille day 2000 Solar Storm. *Solar Phys.*, 204:179–196.

Antiochos, S. K., DeVore, C. R., and Klimchuk, J. A. (1999). A Model for Solar Coronal Mass Ejections. *Astrophys. J.*, 510:485–493.

Arge, C. N., Luhmann, J. G., Odstrcil, D., Schrijver, C. J., and Li, Y. (2004). Stream structure and coronal sources of the solar wind during the May 12th, 1997 CME. *J. Atmos. Solar-Terr. Phys.*, 66:1295–1309.

Aulanier, G., Janvier, M., and Schmieder, B. (2012). The standard flare model in three dimensions. I. Strong-to-weak shear transition in post-flare loops. *Astron. Astrophys.*, 543:A110.

Benkhoff, J., van Casteren, J., Hayakawa, H., Fujimoto, M., Laakso, H., Novara, M., Ferri, P., Middleton, H. R., and Ziethe, R. (2010). BepiColombo—Comprehensive exploration of Mercury: Mission overview and science goals. *Planet. Space Sci.*, 58(1-2):2–20.

Benz, A. O. (2017). Flare Observations. *Living Rev. Sol. Phys.*, 14:2.

Berger, M. A. (2005). Magnetic Helicity Conservation. *Highlights of Astronomy*, 13:85.

Bosman, E., Bothmer, V., Nisticò, G., Vourlidas, A., Howard, R. A., and Davies, J. A. (2012). Three-Dimensional Properties of Coronal Mass Ejections from STEREO/SECCHI Observations. *Solar Phys.*, 281(1):167–185.

Bothmer, V. and Mrotzek, N. (2017). Comparison of CME and ICME Structures Derived from Remote-Sensing and In Situ Observations. *Solar Phys.*, 292:16.

Bothmer, V. and Schwenn, R. (1994). Eruptive prominences as sources of magnetic clouds in the solar wind. *Space Sci. Rev.*, 70:215–220.

Bothmer, V. and Schwenn, R. (1998). The structure and origin of magnetic clouds in the solar wind. *Ann. Geophys.*, 16:1–24.

Boudouridis, A., Zesta, E., Lyons, L. R., Anderson, P. C., and Lummerzheim, D. (2005). Enhanced solar wind geoeffectiveness after a sudden increase in dynamic pressure during southward IMF orientation. *J. Geophys. Res.*, 110(A5):A05214.

Brueckner, G. E., Howard, R. A., Koomen, M. J., Korendyke, C. M., Michels, D. J., Moses, J. D., Socker, D. G., Dere, K. P., Lamy, P. L., Llebaria, A., Bout, M. V., Schwenn, R., Simnett, G. M., Bedford, D. K., and Eyles, C. J. (1995). The Large Angle Spectroscopic

Coronagraph (LASCO). *Solar Phys.*, 162:357–402.

Burlaga, L., Sittler, E., Mariani, F., and Schwenn, R. (1981). Magnetic loop behind an interplanetary shock - Voyager, Helios, and IMP 8 observations. *J. Geophys. Res.*, 86:6673–6684.

Burlaga, L. F. (1988). Magnetic clouds and force-free fields with constant alpha. *J. Geophys. Res.*, 93:7217–7224.

Burlaga, L. F., Plunkett, S. P., and St. Cyr, O. C. (2002). Successive CMEs and complex ejecta. *J. Geophys. Res.*, 107:1266.

Burton, R. K., McPherron, R. L., and Russell, C. T. (1975). An empirical relationship between interplanetary conditions and Dst. *J. Geophys. Res.*, 80:4204.

Cade, W. B. and Chan-Park, C. (2015). The Origin of "Space Weather". *Space Weather*, 13:99–103.

Cahill, L. J. and Amazeen, P. G. (1963). The Boundary of the Geomagnetic Field. *J. Geophys. Res.*, 68:1835–1843.

Calbert, R. and Beard, D. B. (1972). The F and K Components of the Solar Corona. *Astrophys. J.*, 176:497.

Cane, H. V., Richardson, I. G., and Wibberenz, G. (1997). Helios 1 and 2 observations of particle decreases, ejecta, and magnetic clouds. *J. Geophys. Res.*, 102:7075–7086.

Carmichael, H. (1964). A Process for Flares. *NASA Special Publication*, 50:451.

Carrington, R. C. (1859). Description of a Singular Appearance seen in the Sun on September 1, 1859. *Mon. Not. Roy. Astron. Soc.*, 20:13–15.

Chae, J. (2000). The Magnetic Helicity Sign of Filament Chirality. *Astrophys. J. Lett.*, 540:L115–L118.

Charbonneau, P. (2010). Dynamo Models of the Solar Cycle. *Living Rev. Sol. Phys.*, 7(1):3.

Charbonneau, P. (2014). Solar Dynamo Theory. *Annu. Rev. Astron. Astrophys.*, 52:251–290.

Chen, P. F. (2011). Coronal Mass Ejections: Models and Their Observational Basis. *Living Rev. Sol. Phys.*, 8:1.

Cid, C., Saiz, E., Guerrero, A., Palacios, J., and Cerrato, Y. (2015). A Carrington-like geomagnetic storm observed in the 21st century. *J. Space Weather Space Clim.*, 5:A16.

Cranmer, S. R. (2009). Coronal Holes. *Living Rev. Sol. Phys.*, 6(1):3.

Cremades, H. and Bothmer, V. (2004). On the three-dimensional configuration of coronal mass ejections. *Astron. Astrophys.*, 422:307–322.

Crooker, N. U. (2000). Solar and heliospheric geoeffective disturbances. *J. Atmos. Solar-Terr. Phys.*, 62(12):1071–1085.

Dasso, S., Nakwacki, M. S., Démoulin, P., and Mandrini, C. H. (2007). Progressive Transformation of a Flux Rope to an ICME. Comparative Analysis Using the Direct and Fitted Expansion Methods. *Solar Phys.*, 244:115–137.

Davies, J. A., Harrison, R. A., Perry, C. H., Möstl, C., Lugaz, N., Rollett, T., Davis, C. J.,

Crothers, S. R., Temmer, M., Eyles, C. J., and Savani, N. P. (2012). A Self-similar Expansion Model for Use in Solar Wind Transient Propagation Studies. *Astrophys. J.*, 750:23.

Davies, J. A., Harrison, R. A., Rouillard, A. P., Sheeley, N. R., Perry, C. H., Bewsher, D., Davis, C. J., Eyles, C. J., Crothers, S. R., and Brown, D. S. (2009). A synoptic view of solar transient evolution in the inner heliosphere using the Heliospheric Imagers on STEREO. *Geophys. Res. Lett.*, 36(2):L02102.

Davies, J. A., Perry, C. H., Trines, R. M. G. M., Harrison, R. A., Lugaz, N., Möstl, C., Liu, Y. D., and Steed, K. (2013). Establishing a Stereoscopic Technique for Determining the Kinematic Properties of Solar Wind Transients based on a Generalized Self-similarly Expanding Circular Geometry. *Astrophys. J.*, 777:167.

DeForest, C. E., Howard, T. A., and McComas, D. J. (2013). Tracking Coronal Features from the Low Corona to Earth: A Quantitative Analysis of the 2008 December 12 Coronal Mass Ejection. *Astrophys. J.*, 769:43.

Del Zanna, G. and Mason, H. E. (2018). Solar UV and X-ray spectral diagnostics. *Living Rev. Sol. Phys.*, 15(1):5.

Démoulin, P., Priest, E. R., and Lonie, D. P. (1996). Three-dimensional magnetic reconnection without null points 2. Application to twisted flux tubes. *J. Geophys. Res.*, 101:7631–7646.

Dere, K. P., Brueckner, G. E., Howard, R. A., Michels, D. J., and Delaboudiniere, J. P. (1999). LASCO and EIT Observations of Helical Structure in Coronal Mass Ejections. *Astrophys. J.*, 516:465–474.

Desai, M. and Giacalone, J. (2016). Large gradual solar energetic particle events. *Living Rev. Sol. Phys.*, 13:3.

Domingo, V., Fleck, B., and Poland, A. I. (1995). The SOHO Mission: an Overview. *Solar Phys.*, 162:1–37.

Downs, C., Lionello, R., Mikić, Z., Linker, J. A., and Velli, M. (2016). Closed-field Coronal Heating Driven by Wave Turbulence. *Astrophys. J.*, 832(2):180.

Dresing, N., Gómez-Herrero, R., Klassen, A., Heber, B., Kartavykh, Y., and Dröge, W. (2012). The Large Longitudinal Spread of Solar Energetic Particles During the 17 January 2010 Solar Event. *Solar Phys.*, 281:281–300.

Dungey, J. W. (1961). Interplanetary Magnetic Field and the Auroral Zones. *Phys. Rev. Lett.*, 6:47–48.

Engvold, O. (2015). Description and Classification of Prominences. In Vial, J.-C. and Engvold, O., editors, *Solar Prominences*, volume 415 of *Astrophysics and Space Science Library*, page 31.

Eyles, C. J., Harrison, R. A., Davis, C. J., Waltham, N. R., Shaughnessy, B. M., Mapson-Menard, H. C. A., Bewsher, D., Crothers, S. R., Davies, J. A., Simnett, G. M., Howard,

R. A., Moses, J. D., Newmark, J. S., Socker, D. G., Halain, J.-P., Defise, J.-M., Mazy, E., and Rochus, P. (2009). The Heliospheric Imagers Onboard the STEREO Mission. *Solar Phys.*, 254:387–445.

Eyles, C. J., Simnett, G. M., Cooke, M. P., Jackson, B. V., Buffington, A., Hick, P. P., Waltham, N. R., King, J. M., Anderson, P. A., and Holladay, P. E. (2003). The Solar Mass Ejection Imager (Smei). *Solar Phys.*, 217:319–347.

Farrugia, C. J., Dunlop, M. W., Geurts, F., Balogh, A., Southwood, D. J., Bryant, D. A., Neugebauer, M., and Etemadi, A. (1990). An interplanetary planar magnetic structure oriented at a large ($\sim$ 80 deg) angle to the Parker spiral. *Geophys. Res. Lett.*, 17(8):1025–1028.

Farrugia, C. J., Janoo, L. A., Torbert, R. B., Quinn, J. M., Ogilvie, K. W., Lepping, R. P., Fitzenreiter, R. J., Steinberg, J. T., Lazarus, A. J., Lin, R. P., Larson, D., Dasso, S., Gratton, F. T., Lin, Y., and Berdichevsky, D. (1999). A uniform-twist magnetic flux rope in the solar wind. In Habbal, S. R., Esser, R., Hollweg, J. V., and Isenberg, P. A., editors, *American Institute of Physics Conference Series*, volume 471, pages 745–748.

Fisher, G. H., Abbett, W. P., Bercik, D. J., Kazachenko, M. D., Lynch, B. J., Welsch, B. T., Hoeksema, J. T., Hayashi, K., Liu, Y., Norton, A. A., Dalda, A. S., Sun, X., DeRosa, M. L., and Cheung, M. C. M. (2015). The Coronal Global Evolutionary Model: Using HMI Vector Magnetogram and Doppler Data to Model the Buildup of Free Magnetic Energy in the Solar Corona. *Space Weather*, 13(6):369–373.

Fisher, R. R. and Munro, R. H. (1984). Coronal transient geometry. I - The flare-associated event of 1981 March 25. *Astrophys. J.*, 280:428–439.

Forbes, T. G. (2000). A review on the genesis of coronal mass ejections. *J. Geophys. Res.*, 105:23153–23166.

Foukal, P. (1971a). Hα Fine Structure and the Chromospheric Field. *Solar Phys.*, 20:298–309.

Foukal, P. (1971b). Morphological Relationships in the Chromospheric Hα Fine Structure. *Solar Phys.*, 19:59–71.

Fox, N. J., Velli, M. C., Bale, S. D., Decker, R., Driesman, A., Howard, R. A., Kasper, J. C., Kinnison, J., Kusterer, M., Lario, D., Lockwood, M. K., McComas, D. J., Raouafi, N. E., and Szabo, A. (2016). The Solar Probe Plus Mission: Humanity's First Visit to Our Star. *Space Sci. Rev.*, 204(1-4):7–48.

Gibson, S. E., Dalmasse, K., Rachmeler, L. A., De Rosa, M. L., Tomczyk, S., de Toma, G., Burkepile, J., and Galloy, M. (2017a). Magnetic Nulls and Super-radial Expansion in the Solar Corona. *Astrophys. J.*, 840(2):L13.

Gibson, S. E., Fan, Y., Mandrini, C., Fisher, G., and Demoulin, P. (2004). Observational Consequences of a Magnetic Flux Rope Emerging into the Corona. *Astrophys. J.*, 617:600–613.

Gibson, S. E. and Low, B. C. (1998). A Time-Dependent Three-Dimensional Magnetohydro-

dynamic Model of the Coronal Mass Ejection. *Astrophys. J.*, 493(1):460–473.

Gibson, S. E., Rachmeler, L. A., and White, S. M. (2017b). Editorial: Coronal Magnetometry. *Front. Astron. Space Sci.*, 4:3.

Gibson, S. E., Vourlidas, A., Hassler, D. M., Rachmeler, L. A., Thompson, M. J., Newmark, J., Velli, M., Title, A., and McIntosh, S. W. (2018). Solar Physics from Unconventional Viewpoints. *Front. Astron. Space Sci.*, 5:32.

Goldstein, H. (1983). On the field configuration in magnetic clouds. In *NASA Conference Publication*, volume 228 of *NASA Conference Publication*.

Golub, L., Deluca, E., Austin, G., Bookbinder, J., Caldwell, D., Cheimets, P., Cirtain, J., Cosmo, M., Reid, P., Sette, A., Weber, M., Sakao, T., Kano, R., Shibasaki, K., Hara, H., Tsuneta, S., Kumagai, K., Tamura, T., Shimojo, M., McCracken, J., Carpenter, J., Haight, H., Siler, R., Wright, E., Tucker, J., Rutledge, H., Barbera, M., Peres, G., and Varisco, S. (2007). The X-Ray Telescope (XRT) for the Hinode Mission. *Solar Phys.*, 243:63–86.

Gonzalez, W. D., Echer, E., Tsurutani, B. T., Clúa de Gonzalez, A. L., and Dal Lago, A. (2011). Interplanetary Origin of Intense, Superintense and Extreme Geomagnetic Storms. *Space Sci. Rev.*, 158:69–89.

Gonzalez, W. D., Joselyn, J. A., Kamide, Y., Kroehl, H. W., Rostoker, G., Tsurutani, B. T., and Vasyliunas, V. M. (1994). What is a geomagnetic storm? *J. Geophys. Res.*, 99:5771–5792.

Gonzalez, W. D., Tsurutani, B. T., and Clúa de Gonzalez, A. L. (1999). Interplanetary origin of geomagnetic storms. *Space Sci. Rev.*, 88:529–562.

González-Esparza, J. A. and Cuevas-Cardona, M. C. (2018). Observations of Low-Latitude Red Aurora in Mexico During the 1859 Carrington Geomagnetic Storm. *Space Weather*, 16:593–600.

Good, S. W., Forsyth, R. J., Eastwood, J. P., and Möstl, C. (2018). Correlation of ICME Magnetic Fields at Radially Aligned Spacecraft. *Solar Phys.*, 293:52.

Gopalswamy, N., Mäkelä, P., Xie, H., Akiyama, S., and Yashiro, S. (2010). Solar Sources of "Driverless" Interplanetary Shocks. In Maksimovic, M., Issautier, K., Meyer-Vernet, N., Moncuquet, M., and Pantellini, F., editors, *Twelfth International Solar Wind Conference*, volume 1216 of *American Institute of Physics Conference Series*, pages 452–458.

Gopalswamy, N., Yashiro, S., Akiyama, S., and Xie, H. (2017). Estimation of Reconnection Flux Using Post-eruption Arcades and Its Relevance to Magnetic Clouds at 1 AU. *Solar Phys.*, 292(4):65.

Gosling, J. T. (1990). Coronal mass ejections and magnetic flux ropes in interplanetary space. *Geophys. Monogr. Ser.*, 58:343–364.

Gosling, J. T., Birn, J., and Hesse, M. (1995). Three-dimensional magnetic reconnection and the magnetic topology of coronal mass ejection events. *Geophys. Res. Lett.*, 22(8):869–872.

Green, J. L. and Boardsen, S. (2006). Duration and extent of the great auroral storm of 1859. *Adv. Space Res.*, 38:130–135.

Green, L. M., Kliem, B., Török, T., van Driel-Gesztelyi, L., and Attrill, G. D. R. (2007). Transient Coronal Sigmoids and Rotating Erupting Flux Ropes. *Solar Phys.*, 246:365–391.

Green, L. M., Török, T., Vršnak, B., Manchester, W., and Veronig, A. (2018). The Origin, Early Evolution and Predictability of Solar Eruptions. *Space Sci. Rev.*, 214:46.

Guo, J., Dumbović, M., Wimmer-Schweingruber, R. F., Temmer, M., Lohf, H., Wang, Y., Veronig, A., Hassler, D. M., Mays, L. M., Zeitlin, C., Ehresmann, B., Witasse, O., Freiherr von Forstner, J. L., Heber, B., Holmström, M., and Posner, A. (2018). Modeling the Evolution and Propagation of 10 September 2017 CMEs and SEPs Arriving at Mars Constrained by Remote Sensing and In Situ Measurement. *Space Weather*, 16:1156–1169.

Harrison, R. A., Davies, J. A., Biesecker, D., and Gibbs, M. (2017). The application of heliospheric imaging to space weather operations: Lessons learned from published studies. *Space Weather*, 15:985–1003.

Hathaway, D. H. (2015). The Solar Cycle. *Living Rev. Sol. Phys.*, 12(1):4.

Hayakawa, H., Ebihara, Y., Hand, D. P., Hayakawa, S., Kumar, S., Mukherjee, S., and Veenadhari, B. (2018). Low-latitude Aurorae during the Extreme Space Weather Events in 1859. *Astrophys. J.*, 869:57.

Hidalgo, M. A. and Nieves-Chinchilla, T. (2012). A Global Magnetic Topology Model for Magnetic Clouds. I. *Astrophys. J.*, 748(2):109.

Hirayama, T. (1974). Theoretical Model of Flares and Prominences. I: Evaporating Flare Model. *Solar Phys.*, 34:323–338.

Hodgson, R. (1859). On a curious Appearance seen in the Sun. *Mon. Not. Roy. Astron. Soc.*, 20:15–16.

Hood, A. W. and Priest, E. R. (1979). Kink Instability of Solar Coronal Loops as the Cause of Solar Flares. *Solar Phys.*, 64(2):303–321.

Howard, R. A., Moses, J. D., Vourlidas, A., Newmark, J. S., Socker, D. G., Plunkett, S. P., Korendyke, C. M., Cook, J. W., Hurley, A., Davila, J. M., Thompson, W. T., St Cyr, O. C., Mentzell, E., Mehalick, K., Lemen, J. R., Wuelser, J. P., Duncan, D. W., Tarbell, T. D., Wolfson, C. J., Moore, A., Harrison, R. A., Waltham, N. R., Lang, J., Davis, C. J., Eyles, C. J., Mapson-Menard, H., Simnett, G. M., Halain, J. P., Defise, J. M., Mazy, E., Rochus, P., Mercier, R., Ravet, M. F., Delmotte, F., Auchere, F., Delaboudiniere, J. P., Bothmer, V., Deutsch, W., Wang, D., Rich, N., Cooper, S., Stephens, V., Maahs, G., Baugh, R., McMullin, D., and Carter, T. (2008). Sun Earth Connection Coronal and Heliospheric Investigation (SECCHI). *Space Sci. Rev.*, 136:67–115.

Howard, T. A. and DeForest, C. E. (2012). The Thomson Surface. I. Reality and Myth. *Astrophys. J.*, 752:130.

Howard, T. A., DeForest, C. E., Schneck, U. G., and Alden, C. R. (2017). Challenging

Some Contemporary Views of Coronal Mass Ejections. II. The Case for Absent Filaments. *Astrophys. J.*, 834(1):86.

Howard, T. A., Stovall, K., Dowell, J., Taylor, G. B., and White, S. M. (2016). Measuring the Magnetic Field of Coronal Mass Ejections Near the Sun Using Pulsars. *Astrophys. J.*, 831(2):208.

Howard, T. A. and Tappin, S. J. (2009). Interplanetary Coronal Mass Ejections Observed in the Heliosphere: 1. Review of Theory. *Space Sci. Rev.*, 147(1-2):31–54.

Hudson, H. S. and Webb, D. F. (1997). Soft X-Ray Signatures of Coronal Ejections. *Coronal Mass Ejections*, pages 27–38.

Huttunen, K. and Koskinen, H. (2004). Importance of post-shock streams and sheath region as drivers of intense magnetospheric storms and high-latitude activity. *Ann. Geophys.*, 22:1729–1738.

Huttunen, K. E. J., Koskinen, H. E. J., and Schwenn, R. (2002). Variability of magnetospheric storms driven by different solar wind perturbations. *J. Geophys. Res.*, 107:1121.

Huttunen, K. E. J., Schwenn, R., Bothmer, V., and Koskinen, H. E. J. (2005). Properties and geoeffectiveness of magnetic clouds in the rising, maximum and early declining phases of solar cycle 23. *Ann. Geophys.*, 23:625–641.

Illing, R. M. E. and Hundhausen, A. J. (1985). Observation of a coronal transient from 1.2 to 6 solar radii. *J. Geophys. Res.*, 90:275–282.

Isavnin, A., Kilpua, E. K. J., and Koskinen, H. E. J. (2011). Grad-Shafranov Reconstruction of Magnetic Clouds: Overview and Improvements. *Solar Phys.*, 273:205–219.

Isavnin, A., Vourlidas, A., and Kilpua, E. K. J. (2013). Three-Dimensional Evolution of Erupted Flux Ropes from the Sun (2–20 $R_\odot$) to 1 AU. *Solar Phys.*, 284:203–215.

Isavnin, A., Vourlidas, A., and Kilpua, E. K. J. (2014). Three-Dimensional Evolution of Flux-Rope CMEs and Its Relation to the Local Orientation of the Heliospheric Current Sheet. *Solar Phys.*, 289:2141–2156.

Isenberg, P. A. and Forbes, T. G. (2007). A Three-dimensional Line-tied Magnetic Field Model for Solar Eruptions. *Astrophys. J.*, 670(2):1453–1466.

James, A. W., Valori, G., Green, L. M., Liu, Y., Cheung, M. C. M., Guo, Y., and van Driel-Gesztelyi, L. (2018). An Observationally Constrained Model of a Flux Rope that Formed in the Solar Corona. *Astrophys. J. Lett.*, 855(2):L16.

Janvier, M., Aulanier, G., Bommier, V., Schmieder, B., Démoulin, P., and Pariat, E. (2014). Electric Currents in Flare Ribbons: Observations and Three-dimensional Standard Model. *Astrophys. J.*, 788(1):60.

Janvier, M., Winslow, R. M., Good, S., Bonhomme, E., Démoulin, P., Dasso, S., Möstl, C., Lugaz, N., Amerstorfer, T., Soubrié, E., and Boakes, P. D. (2019). Generic Magnetic Field Intensity Profiles of Interplanetary Coronal Mass Ejections at Mercury, Venus, and Earth From Superposed Epoch Analyses. *J. Geophys. Res. Space Physics*, 124(2):812–836.

Jian, L., Russell, C. T., Luhmann, J. G., and Skoug, R. M. (2006a). Properties of Interplanetary Coronal Mass Ejections at One AU During 1995 – 2004. *Solar Phys.*, 239:393–436.

Jian, L., Russell, C. T., Luhmann, J. G., and Skoug, R. M. (2006b). Properties of Stream Interactions at One AU During 1995 – 2004. *Solar Phys.*, 239:337–392.

Jones, G. H., Rees, A., Balogh, A., and Forsyth, R. J. (2002). The draping of heliospheric magnetic fields upstream of coronal mass ejecta. *Geophys. Res. Lett.*, 29(11):1520.

Kahler, S. W. (2001). The correlation between solar energetic particle peak intensities and speeds of coronal mass ejections: Effects of ambient particle intensities and energy spectra. *J. Geophys. Res.*, 106:20947–20956.

Kaiser, M. L., Kucera, T. A., Davila, J. M., St. Cyr, O. C., Guhathakurta, M., and Christian, E. (2008). The STEREO Mission: An Introduction. *Space Sci. Rev.*, 136:5–16.

Kataoka, R., Watari, S., Shimada, N., Shimazu, H., and Marubashi, K. (2005). Downstream structures of interplanetary fast shocks associated with coronal mass ejections. *Geophys. Res. Lett.*, 32(12):L12103.

Kay, C., Gopalswamy, N., Reinard, A., and Opher, M. (2017). Predicting the Magnetic Field of Earth-impacting CMEs. *Astrophys. J.*, 835:117.

Kay, C., Opher, M., Colaninno, R. C., and Vourlidas, A. (2016). Using ForeCAT Deflections and Rotations to Constrain the Early Evolution of CMEs. *Astrophys. J.*, 827:70.

Kay, C., Opher, M., and Evans, R. M. (2015). Global Trends of CME Deflections Based on CME and Solar Parameters. *Astrophys. J.*, 805:168.

Kaymaz, Z. and Siscoe, G. (2006). Field-Line Draping Around ICMES. *Solar Phys.*, 239:437–448.

Kazachenko, M. D., Lynch, B. J., Welsch, B. T., and Sun, X. (2017). A Database of Flare Ribbon Properties from the Solar Dynamics Observatory. I. Reconnection Flux. *Astrophys. J.*, 845(1):49.

Kilpua, E., Koskinen, H. E. J., and Pulkkinen, T. I. (2017). Coronal mass ejections and their sheath regions in interplanetary space. *Living Rev. Sol. Phys.*, 14:5.

Kilpua, E. K. J., Jian, L. K., Li, Y., Luhmann, J. G., and Russell, C. T. (2011). Multipoint ICME encounters: Pre-STEREO and STEREO observations. *J. Atmos. Solar-Terr. Phys.*, 73:1228–1241.

Kilpua, E. K. J., Lugaz, N., Mays, M. L., and Temmer, M. (2019). Forecasting the Structure and Orientation of Earthbound Coronal Mass Ejections. *Space Weather*, 17(4):498–526.

Klein, K.-L. and Dalla, S. (2017). Acceleration and Propagation of Solar Energetic Particles. *Space Sci. Rev.*, 212:1107–1136.

Kliem, B., Lin, J., Forbes, T. G., Priest, E. R., and Török, T. (2014). Catastrophe versus Instability for the Eruption of a Toroidal Solar Magnetic Flux Rope. *Astrophys. J.*, 789(1):46.

Kliem, B. and Török, T. (2006). Torus Instability. *Phys. Rev. Lett.*, 96(25):255002.

Klimchuk, J. A. (2001). Theory of Coronal Mass Ejections. *Washington DC American Geophysical Union Geophysical Monograph Series*, 125:143.

Klimchuk, J. A. (2015). Key aspects of coronal heating. *Phil. Trans. R. Soc. London Ser. A*, 373(2042):20140256–20140256.

Knipp, D. J., Fraser, B. J., Shea, M. A., and Smart, D. F. (2018). On the Little-Known Consequences of the 4 August 1972 Ultra-Fast Coronal Mass Ejecta: Facts, Commentary, and Call to Action. *Space Weather*, 16:1635–1643.

Kopp, R. A. and Pneuman, G. W. (1976). Magnetic reconnection in the corona and the loop prominence phenomenon. *Solar Phys.*, 50:85–98.

Kosugi, T., Matsuzaki, K., Sakao, T., Shimizu, T., Sone, Y., Tachikawa, S., Hashimoto, T., Minesugi, K., Ohnishi, A., Yamada, T., Tsuneta, S., Hara, H., Ichimoto, K., Suematsu, Y., Shimojo, M., Watanabe, T., Shimada, S., Davis, J. M., Hill, L. D., Owens, J. K., Title, A. M., Culhane, J. L., Harra, L. K., Doschek, G. A., and Golub, L. (2007). The Hinode (Solar-B) Mission: An Overview. *Solar Phys.*, 243:3–17.

Lagg, A., Lites, B., Harvey, J., Gosain, S., and Centeno, R. (2017). Measurements of Photospheric and Chromospheric Magnetic Fields. *Space Sci. Rev.*, 210(1-4):37–76.

Larmor, J. (1919). How could a Rotating Body such as the Sun become a Magnet? *Rep. Brit. Assoc. Adv. Sci.*

Lee, C. O., Arge, C. N., Odstrčil, D., Millward, G., Pizzo, V., Quinn, J. M., and Henney, C. J. (2013). Ensemble Modeling of CME Propagation. *Solar Phys.*, 285(1-2):349–368.

Lee, C. O., Jakosky, B. M., Luhmann, J. G., Brain, D. A., Mays, M. L., Hassler, D. M., Holmström, M., Larson, D. E., Mitchell, D. L., Mazelle, C., and Halekas, J. S. (2018). Observations and Impacts of the 10 September 2017 Solar Events at Mars: An Overview and Synthesis of the Initial Results. *Geophys. Res. Lett.*, 45:8871–8885.

Lemen, J. R., Title, A. M., Akin, D. J., Boerner, P. F., Chou, C., Drake, J. F., Duncan, D. W., Edwards, C. G., Friedlaender, F. M., Heyman, G. F., Hurlburt, N. E., Katz, N. L., Kushner, G. D., Levay, M., Lindgren, R. W., Mathur, D. P., McFeaters, E. L., Mitchell, S., Rehse, R. A., Schrijver, C. J., Springer, L. A., Stern, R. A., Tarbell, T. D., Wuelser, J.-P., Wolfson, C. J., Yanari, C., Bookbinder, J. A., Cheimets, P. N., Caldwell, D., Deluca, E. E., Gates, R., Golub, L., Park, S., Podgorski, W. A., Bush, R. I., Scherrer, P. H., Gummin, M. A., Smith, P., Auker, G., Jerram, P., Pool, P., Soufli, R., Windt, D. L., Beardsley, S., Clapp, M., Lang, J., and Waltham, N. (2012). The Atmospheric Imaging Assembly (AIA) on the Solar Dynamics Observatory (SDO). *Solar Phys.*, 275:17–40.

Lepping, R. P., Burlaga, L. F., and Jones, J. A. (1990). Magnetic field structure of interplanetary magnetic clouds at 1 AU. *J. Geophys. Res.*, 95:11957–11965.

Linker, J. A., Lionello, R., Mikić, Z., and Amari, T. (2001). Magnetohydrodynamic modeling of prominence formation within a helmet streamer. *J. Geophys. Res.*, 106(A11):25165–25176.

Linker, J. A. and Mikic, Z. (1995). Disruption of a Helmet Streamer by Photospheric Shear. *Astrophys. J.*, 438:L45.

Linker, J. A., Mikić, Z., Lionello, R., Riley, P., Amari, T., and Odstrcil, D. (2003). Flux cancellation and coronal mass ejections. *Phys. Plasmas*, 10(5):1971–1978.

Liu, Y., Manchester, W. B., Richardson, J. D., Luhmann, J. G., Lin, R. P., and Bale, S. D. (2008). Deflection flows ahead of ICMEs as an indicator of curvature and geoeffectiveness. *J. Geophys. Res.*, 113(A9):A00B03.

Liu, Y. D., Luhmann, J. G., Kajdič, P., Kilpua, E. K. J., Lugaz, N., Nitta, N. V., Möstl, C., Lavraud, B., Bale, S. D., Farrugia, C. J., and Galvin, A. B. (2014). Observations of an extreme storm in interplanetary space caused by successive coronal mass ejections. *Nat. Commun.*, 5:3481.

Lopez, R. E., Baker, D. N., and Allen, J. (2004). Sun Unleashes Halloween Storm. *Eos Trans.*, 85:105–108.

López Fuentes, M. C., Demoulin, P., Mandrini, C. H., and van Driel-Gesztelyi, L. (2000). The Counterkink Rotation of a Non-Hale Active Region. *Astrophys. J.*, 544:540–549.

Lugaz, N., Farrugia, C. J., Davies, J. A., Möstl, C., Davis, C. J., Roussev, I. I., and Temmer, M. (2012). The Deflection of the Two Interacting Coronal Mass Ejections of 2010 May 23-24 as Revealed by Combined in Situ Measurements and Heliospheric Imaging. *Astrophys. J.*, 759:68.

Lugaz, N., Farrugia, C. J., Manchester, W. B., I., and Schwadron, N. (2013). The Interaction of Two Coronal Mass Ejections: Influence of Relative Orientation. *Astrophys. J.*, 778(1):20.

Lugaz, N., Farrugia, C. J., Winslow, R. M., Al-Haddad, N., Galvin, A. B., Nieves-Chinchilla, T., Lee, C. O., and Janvier, M. (2018). On the Spatial Coherence of Magnetic Ejecta: Measurements of Coronal Mass Ejections by Multiple Spacecraft Longitudinally Separated by 0.01 au. *Astrophys. J. Lett.*, 864(1):L7.

Lugaz, N., Farrugia, C. J., Winslow, R. M., Al-Haddad, N., Kilpua, E. K. J., and Riley, P. (2016). Factors affecting the geoeffectiveness of shocks and sheaths at 1 AU. *J. Geophys. Res. Space Physics*, 121(11):10,861–10,879.

Lugaz, N., Manchester, W. B., I., and Gombosi, T. I. (2005). The Evolution of Coronal Mass Ejection Density Structures. *Astrophys. J.*, 627:1019–1030.

Lugaz, N., Temmer, M., Wang, Y., and Farrugia, C. J. (2017). The Interaction of Successive Coronal Mass Ejections: A Review. *Solar Phys.*, 292:64.

Luoni, M. L., Démoulin, P., Mandrini, C. H., and van Driel-Gesztelyi, L. (2011). Twisted Flux Tube Emergence Evidenced in Longitudinal Magnetograms: Magnetic Tongues. *Solar Phys.*, 270:45–74.

Lynch, B. J., Antiochos, S. K., DeVore, C. R., Luhmann, J. G., and Zurbuchen, T. H. (2008). Topological Evolution of a Fast Magnetic Breakout CME in Three Dimensions. *Astrophys.*

J., 683:1192–1206.

Lynch, B. J., Antiochos, S. K., Li, Y., Luhmann, J. G., and DeVore, C. R. (2009). Rotation of Coronal Mass Ejections during Eruption. *Astrophys. J.*, 697:1918–1927.

Lynch, B. J., Antiochos, S. K., MacNeice, P. J., Zurbuchen, T. H., and Fisk, L. A. (2004). Observable Properties of the Breakout Model for Coronal Mass Ejections. *Astrophys. J.*, 617:589–599.

Lynch, B. J. and Edmondson, J. K. (2013). Sympathetic Magnetic Breakout Coronal Mass Ejections from Pseudostreamers. *Astrophys. J.*, 764:87.

Lyot, B. (1931). L'Etude de la Couronne Solaire en Dehors des Eclipses. *L'Astronomie*, 45:248–253.

Magdalenić, J., Marqué, C., Zhukov, A. N., Vršnak, B., and Žic, T. (2010). Origin of Coronal Shock Waves Associated with Slow Coronal Mass Ejections. *Astrophys. J.*, 718:266–278.

Malandraki, O. E. and Crosby, N. B. (2018). Solar Energetic Particles and Space Weather: Science and Applications. In Malandraki, O. E. and Crosby, N. B., editors, *Solar Particle Radiation Storms Forecasting and Analysis*, volume 444, pages 1–26.

Manchester, Ward B., I., Vourlidas, A., Tóth, G., Lugaz, N., Roussev, I. I., Sokolov, I. V., Gombosi, T. I., De Zeeuw, D. L., and Opher, M. (2008). Three-dimensional MHD Simulation of the 2003 October 28 Coronal Mass Ejection: Comparison with LASCO Coronagraph Observations. *Astrophys. J.*, 684:1448–1460.

Manchester, W., Kilpua, E. K. J., Liu, Y. D., Lugaz, N., Riley, P., Török, T., and Vršnak, B. (2017). The Physical Processes of CME/ICME Evolution. *Space Sci. Rev.*.

Martin, S. F. (1998a). Conditions for the Formation and Maintenance of Filaments (Invited Review). *Solar Phys.*, 182(1):107–137.

Martin, S. F. (1998b). Filament Chirality: A Link Between Fine-Scale and Global Patterns (Review). In Webb, D. F., Schmieder, B., and Rust, D. M., editors, *IAU Colloq. 167: New Perspectives on Solar Prominences*, volume 150 of *Astron. Soc. Pacific C.S.*, page 419.

Martin, S. F., Marquette, W. H., and Bilimoria, R. (1992). The Solar Cycle Pattern in the Direction of the Magnetic Field along the Long Axes of Polar Filaments. In Harvey, K. L., editor, *The Solar Cycle*, volume 27 of *Astronomical Society of the Pacific Conference Series*, page 53.

Martin, S. F. and McAllister, A. H. (1996). The Skew of X-ray Coronal Loops Overlying H alpha Filaments. In Uchida, Y., Kosugi, T., and Hudson, H. S., editors, *IAU Colloq. 153: Magnetodynamic Phenomena in the Solar Atmosphere - Prototypes of Stellar Magnetic Activity*, page 497.

Marubashi, K., Akiyama, S., Yashiro, S., Gopalswamy, N., Cho, K.-S., and Park, Y.-D. (2015). Geometrical Relationship Between Interplanetary Flux Ropes and Their Solar Sources. *Solar Phys.*, 290:1371–1397.

Maunder, E. W. (1904). Note on the Distribution of Sun-spots in Heliographic Latitude,

1874-1902. *Mon. Not. Roy. Astron. Soc.*, 64:747–761.

Mays, M. L., Thompson, B. J., Jian, L. K., Colaninno, R. C., Odstrcil, D., Möstl, C., Temmer, M., Savani, N. P., Collinson, G., Taktakishvili, A., MacNeice, P. J., and Zheng, Y. (2015). Propagation of the 7 January 2014 CME and Resulting Geomagnetic Non-event. *Astrophys. J.*, 812:145.

McAllister, A. H., Hundhausen, A. J., Mackay, D., and Priest, E. (1998). The Skew of Polar Crown X-ray Arcades. In Webb, D. F., Schmieder, B., and Rust, D. M., editors, *IAU Colloq. 167: New Perspectives on Solar Prominences*, volume 150 of *Astron. Soc. Pacific C.S.*, page 430.

McComas, D. J., Ebert, R. W., Elliott, H. A., Goldstein, B. E., Gosling, J. T., Schwadron, N. A., and Skoug, R. M. (2008). Weaker solar wind from the polar coronal holes and the whole Sun. *Geophys. Res. Lett.*, 35:L18103.

Mitalas, R. and Sills, K. R. (1992). On the Photon Diffusion Time Scale for the Sun. *Astrophys. J.*, 401:759.

Moore, R. L., Sterling, A. C., Hudson, H. S., and Lemen, J. R. (2001). Onset of the Magnetic Explosion in Solar Flares and Coronal Mass Ejections. *Astrophys. J.*, 552:833–848.

Moreno Cárdenas, F., Cristancho Sánchez, S., and Vargas Domínguez, S. (2016). The grand aurorae borealis seen in Colombia in 1859. *Adv. Space Res.*, 57:257–267.

Möstl, C., Amla, K., Hall, J. R., Liewer, P. C., De Jong, E. M., Colaninno, R. C., Veronig, A. M., Rollett, T., Temmer, M., Peinhart, V., Davies, J. A., Lugaz, N., Liu, Y. D., Farrugia, C. J., Luhmann, J. G., Vršnak, B., Harrison, R. A., and Galvin, A. B. (2014). Connecting Speeds, Directions and Arrival Times of 22 Coronal Mass Ejections from the Sun to 1 AU. *Astrophys. J.*, 787:119.

Möstl, C., Farrugia, C. J., Kilpua, E. K. J., Jian, L. K., Liu, Y., Eastwood, J. P., Harrison, R. A., Webb, D. F., Temmer, M., Odstrcil, D., Davies, J. A., Rollett, T., Luhmann, J. G., Nitta, N., Mulligan, T., Jensen, E. A., Forsyth, R., Lavraud, B., de Koning, C. A., Veronig, A. M., Galvin, A. B., Zhang, T. L., and Anderson, B. J. (2012). Multi-point Shock and Flux Rope Analysis of Multiple Interplanetary Coronal Mass Ejections around 2010 August 1 in the Inner Heliosphere. *Astrophys. J.*, 758:10.

Möstl, C., Miklenic, C., Farrugia, C. J., Temmer, M., Veronig, A., Galvin, A. B., Vršnak, B., and Biernat, H. K. (2008). Two-spacecraft reconstruction of a magnetic cloud and comparison to its solar source. *Ann. Geophys.*, 26:3139–3152.

Müller, D., Marsden, R. G., St. Cyr, O. C., and Gilbert, H. R. (2013). Solar Orbiter . Exploring the Sun-Heliosphere Connection. *Solar Phys.*, 285(1-2):25–70.

Mulligan, T., Russell, C. T., and Luhmann, J. G. (1998). Solar cycle evolution of the structure of magnetic clouds in the inner heliosphere. *Geophys. Res. Lett.*, 25:2959–2962.

Munro, R. H., Gosling, J. T., Hildner, E., MacQueen, R. M., Poland, A. I., and Ross, C. L. (1979). The association of coronal mass ejection transients with other forms of solar

activity. *Solar Phys.*, 61(1):201–215.

Musk, E. (2017). Making Humans a Multi-Planetary Species. *New Space*, 5:46–61.

Musk, E. (2018). Making Life Multi-Planetary. *New Space*, 6:2–11.

Musmann, G., Neubauer, F. M., Maier, A., and Lammers, E. (1975). Das Förstersonden–Magetfeldexperiment (E2). *Raumfahrtforschung*, 19:232–237.

Nakagawa, T. (1993). Solar Source of the Interplanetary Planar Magnetic Structures. *Solar Phys.*, 147(1):169–197.

Nakagawa, T., Nishida, A., and Saito, T. (1989). Planar magnetic structures in the solar wind. *J. Geophys. Res.*, 94(A9):11761–11775.

Ness, N. F., Scearce, C. S., and Cantarano, S. C. (1967). Probable Observations of the Geomagnetic Tail at 10^3 Earth Radii by Pioneer 7. *J. Geophys. Res.*, 72:3769.

Nieves-Chinchilla, T., Vourlidas, A., Raymond, J. C., Linton, M. G., Al-haddad, N., Savani, N. P., Szabo, A., and Hidalgo, M. A. (2018). Understanding the Internal Magnetic Field Configurations of ICMEs Using More than 20 Years of Wind Observations. *Solar Phys.*, 293:25.

O'Brien, T. P. and McPherron, R. L. (2000). An empirical phase space analysis of ring current dynamics: Solar wind control of injection and decay. *J. Geophys. Res.*, 105:7707–7720.

Odstrcil, D. (2003). Modeling 3-D solar wind structure. *Adv. Space Res.*, 32:497–506.

Odstrcil, D. and Pizzo, V. J. (1999). Distortion of the interplanetary magnetic field by three-dimensional propagation of coronal mass ejections in a structured solar wind. *J. Geophys. Res.*, 104:28225–28240.

Ogilvie, K. W. and Desch, M. D. (1997). The wind spacecraft and its early scientific results. *Adv. Space Res.*, 20:559–568.

Owens, M. J. (2008). Combining remote and in situ observations of coronal mass ejections to better constrain magnetic cloud reconstruction. *J. Geophys. Res.*, 113(A12):A12102.

Owens, M. J. and Forsyth, R. J. (2013). The Heliospheric Magnetic Field. *Living Rev. Sol. Phys.*, 10(1):5.

Owens, M. J., Lockwood, M., and Barnard, L. A. (2017). Coronal mass ejections are not coherent magnetohydrodynamic structures. *Sci. Rep.*, 7:4152.

Owens, M. J., Merkin, V. G., and Riley, P. (2006). A kinematically distorted flux rope model for magnetic clouds. *J. Geophys. Res.*, 111(A3):A03104.

Parenti, S. (2014). Solar Prominences: Observations. *Living Rev. Sol. Phys.*, 11(1):1.

Parker, E. N. (1958). Dynamics of the Interplanetary Gas and Magnetic Fields. *Astrophys. J.*, 128:664.

Parnell, C. E. and De Moortel, I. (2012). A contemporary view of coronal heating. *Phil. Trans. R. Soc. London Ser. A*, 370(1970):3217–3240.

Pesnell, W. D., Thompson, B. J., and Chamberlin, P. C. (2012). The Solar Dynamics Observatory (SDO). *Solar Phys.*, 275:3–15.

Pevtsov, A. A. and Balasubramaniam, K. S. (2003). Helicity patterns on the sun. *Adv. Space Res.*, 32:1867–1874.

Pevtsov, A. A., Berger, M. A., Nindos, A., Norton, A. A., and van Driel-Gesztelyi, L. (2014). Magnetic Helicity, Tilt, and Twist. *Space Sci. Rev.*, 186:285–324.

Pizzo, V. (1978). A three-deminsional model of corotating streams in the solar wind 1. Theoretical foundations. *J. Geophys. Res.*, 83:5563–5572.

Pomoell, J., Lumme, E., and Kilpua, E. (2019). Time-dependent Data-driven Modeling of Active Region Evolution Using Energy-optimized Photospheric Electric Fields. *Solar Phys.*, 294(4):41.

Pomoell, J. and Poedts, S. (2018). EUHFORIA: European heliospheric forecasting information asset. *J. Space Weather Space Clim.*, 8:A35.

Pulkkinen, T. (2007). Space Weather: Terrestrial Perspective. *Living Rev. Sol. Phys.*, 4:1.

Raeder, J., Wang, Y. L., Fuller-Rowell, T. J., and Singer, H. J. (2001). Global Simulation of Magnetospheric Space Weather Effects of the Bastille Day Storm. *Solar Phys.*, 204:323–337.

Reale, F. (2014). Coronal Loops: Observations and Modeling of Confined Plasma. *Living Rev. Sol. Phys.*, 11(1):4.

Rice, W. K. M., Zank, G. P., and Li, G. (2003). Particle acceleration and coronal mass ejection driven shocks: Shocks of arbitrary strength. *J. Geophys. Res.*, 108:1369.

Richardson, I. G. (2018). Solar wind stream interaction regions throughout the heliosphere. *Living Rev. Sol. Phys.*, 15:1.

Richardson, I. G. and Cane, H. V. (2004). Identification of interplanetary coronal mass ejections at 1 AU using multiple solar wind plasma composition anomalies. *J. Geophys. Res.*, 109:A09104.

Richardson, I. G. and Cane, H. V. (2012). Solar wind drivers of geomagnetic storms during more than four solar cycles. *J. Space Weather Space Clim.*, 2:A01.

Richardson, J. D., Liu, Y., Wang, C., and Burlaga, L. F. (2006). ICMES at very large distances. *Adv. Space Res.*, 38(3):528–534.

Riley, P., Mays, M. L., Andries, J., Amerstorfer, T., Biesecker, D., Delouille, V., Dumbović, M., Feng, X., Henley, E., Linker, J. A., Möstl, C., Nuñez, M., Pizzo, V., Temmer, M., Tobiska, W. K., Verbeke, C., West, M. J., and Zhao, X. (2018). Forecasting the Arrival Time of Coronal Mass Ejections: Analysis of the CCMC CME Scoreboard. *Space Weather*, 16:1245–1260.

Rodriguez, L., Masías-Meza, J. J., Dasso, S., Démoulin, P., Zhukov, A. N., Gulisano, A. M., Mierla, M., Kilpua, E., West, M., Lacatus, D., Paraschiv, A., and Janvier, M. (2016). Typical Profiles and Distributions of Plasma and Magnetic Field Parameters in Magnetic Clouds at 1 AU. *Solar Phys.*, 291:2145–2163.

Rollett, T., Möstl, C., Isavnin, A., Davies, J. A., Kubicka, M., Amerstorfer, U. V., and

Harrison, R. A. (2016). ElEvoHI: A Novel CME Prediction Tool for Heliospheric Imaging Combining an Elliptical Front with Drag-based Model Fitting. *Astrophys. J.*, 824:131.

Rostoker, G. (1972). Geomagnetic indices. *Rev. Geophys. Space Phys.*, 10:935–950.

Ruffenach, A., Lavraud, B., Owens, M. J., Sauvaud, J.-A., Savani, N. P., Rouillard, A. P., Démoulin, P., Foullon, C., Opitz, A., Fedorov, A., Jacquey, C. J., Génot, V., Louarn, P., Luhmann, J. G., Russell, C. T., Farrugia, C. J., and Galvin, A. B. (2012). Multispacecraft observation of magnetic cloud erosion by magnetic reconnection during propagation. *J. Geophys. Res.*, 117:A09101.

Rust, D. M. and Kumar, A. (1996). Evidence for Helically Kinked Magnetic Flux Ropes in Solar Eruptions. *Astrophys. J. Lett.*, 464:L199.

Savani, N. P., Davies, J. A., Davis, C. J., Shiota, D., Rouillard, A. P., Owens, M. J., Kusano, K., Bothmer, V., Bamford, S. P., Lintott, C. J., and Smith, A. (2012). Observational Tracking of the 2D Structure of Coronal Mass Ejections Between the Sun and 1 AU. *Solar Phys.*, 279(2):517–535.

Savani, N. P., Owens, M. J., Rouillard, A. P., Forsyth, R. J., and Davies, J. A. (2010). Observational Evidence of a Coronal Mass Ejection Distortion Directly Attributable to a Structured Solar Wind. *Astrophys. J. Lett.*, 714:L128–L132.

Savani, N. P., Owens, M. J., Rouillard, A. P., Forsyth, R. J., Kusano, K., Shiota, D., Kataoka, R., Jian, L., and Bothmer, V. (2011). Evolution of Coronal Mass Ejection Morphology with Increasing Heliocentric Distance. II. In Situ Observations. *Astrophys. J.*, 732(2):117.

Savani, N. P., Vourlidas, A., Richardson, I. G., Szabo, A., Thompson, B. J., Pulkkinen, A., Mays, M. L., Nieves-Chinchilla, T., and Bothmer, V. (2017). Predicting the magnetic vectors within coronal mass ejections arriving at Earth: 2. Geomagnetic response. *Space Weather*, 15:441–461.

Savani, N. P., Vourlidas, A., Szabo, A., Mays, M. L., Richardson, I. G., Thompson, B. J., Pulkkinen, A., Evans, R., and Nieves-Chinchilla, T. (2015). Predicting the magnetic vectors within coronal mass ejections arriving at Earth: 1. Initial architecture. *Space Weather*, 13:374–385.

Scherrer, P. H., Bogart, R. S., Bush, R. I., Hoeksema, J. T., Kosovichev, A. G., Schou, J., Rosenberg, W., Springer, L., Tarbell, T. D., Title, A., Wolfson, C. J., Zayer, I., and MDI Engineering Team (1995). The Solar Oscillations Investigation - Michelson Doppler Imager. *Solar Phys.*, 162(1-2):129–188.

Scherrer, P. H., Schou, J., Bush, R. I., Kosovichev, A. G., Bogart, R. S., Hoeksema, J. T., Liu, Y., Duvall, T. L., Zhao, J., Title, A. M., Schrijver, C. J., Tarbell, T. D., and Tomczyk, S. (2012). The Helioseismic and Magnetic Imager (HMI) Investigation for the Solar Dynamics Observatory (SDO). *Solar Phys.*, 275:207–227.

Schmidt, J. and Cargill, P. (2004). A numerical study of two interacting coronal mass ejections. *Ann. Geophys.*, 22(6):2245–2254.

Schwabe, S. H. (1843). Die Sonne. *Astron. Nachr.*, 20(17):283.

Schwenn, R., Rosenbauer, H., and Miggenrieder, H. (1975). Das Plasmaexperiment auf Helios (E1). *Raumfahrtforschung*, 19:226–232.

Scolini, C., Rodriguez, L., Mierla, M., Pomoell, J., and Poedts, S. (2019). Observation-based modelling of magnetised coronal mass ejections with euhforia. *Astron. Astrophys.*, in press.

Scolini, C., Verbeke, C., Poedts, S., Chané, E., Pomoell, J., and Zuccarello, F. P. (2018). Effect of the Initial Shape of Coronal Mass Ejections on 3-D MHD Simulations and Geoeffectiveness Predictions. *Space Weather*, 16:754–771.

Sheeley, Jr., N. R., Herbst, A. D., Palatchi, C. A., Wang, Y.-M., Howard, R. A., Moses, J. D., Vourlidas, A., Newmark, J. S., Socker, D. G., Plunkett, S. P., Korendyke, C. M., Burlaga, L. F., Davila, J. M., Thompson, W. T., St Cyr, O. C., Harrison, R. A., Davis, C. J., Eyles, C. J., Halain, J. P., Wang, D., Rich, N. B., Battams, K., Esfandiari, E., and Stenborg, G. (2008). Heliospheric Images of the Solar Wind at Earth. *Astrophys. J.*, 675:853–862.

Shiota, D. and Kataoka, R. (2016). Magnetohydrodynamic simulation of interplanetary propagation of multiple coronal mass ejections with internal magnetic flux rope (SUSANOO-CME). *Space Weather*, 14:56–75.

Siscoe, G. and Odstrcil, D. (2008). Ways in which ICME sheaths differ from magnetosheaths. *J. Geophys. Res.*, 113:A00B07.

Solomon, S. C., McNutt, R. L., Gold, R. E., and Domingue, D. L. (2007). MESSENGER Mission Overview. *Space Sci. Rev.*, 131:3–39.

Srivastava, N., Mishra, W., and Chakrabarty, D. (2018). Interplanetary and Geomagnetic Consequences of Interacting CMEs of 13 - 14 June 2012. *Solar Phys.*, 293:5.

Stone, E. C., Frandsen, A. M., Mewaldt, R. A., Christian, E. R., Margolies, D., Ormes, J. F., and Snow, F. (1998). The Advanced Composition Explorer. *Space Sci. Rev.*, 86:1–22.

Sturrock, P. A. (1966). Model of the High-Energy Phase of Solar Flares. *Nature*, 211:695–697.

Svedhem, H., Titov, D. V., McCoy, D., Lebreton, J. P., Barabash, S., Bertaux, J. L., Drossart, P., Formisano, V., Häusler, B., Korablev, O., Markiewicz, W. J., Nevejans, D., Pätzold, M., Piccioni, G., Zhang, T. L., Taylor, F. W., Lellouch, E., Koschny, D., Witasse, O., Eggel, H., Warhaut, M., Accomazzo, A., Rodriguez- Canabal, J., Fabrega, J., Schirmann, T., Clochet, A., and Coradini, M. (2007). Venus Express—The first European mission to Venus. *Planet. Space Sci.*, 55:1636–1652.

Temerin, M. and Li, X. (2002). A new model for the prediction of Dst on the basis of the solar wind. *J. Geophys. Res.*, 107:1472.

Temmer, M. and Nitta, N. V. (2015). Interplanetary Propagation Behavior of the Fast Coronal Mass Ejection on 23 July 2012. *Solar Phys.*, 290:919–932.

Thernisien, A. (2011). Implementation of the Graduated Cylindrical Shell Model for the Three-dimensional Reconstruction of Coronal Mass Ejections. *Astrophys. J. Suppl.*, 194:33.

Thernisien, A., Vourlidas, A., and Howard, R. A. (2009). Forward Modeling of Coronal Mass Ejections Using STEREO/SECCHI Data. *Solar Phys.*, 256:111–130.

Thernisien, A. F. R., Howard, R. A., and Vourlidas, A. (2006). Modeling of Flux Rope Coronal Mass Ejections. *Astrophys. J.*, 652:763–773.

Thompson, B. J., Cliver, E. W., Nitta, N., Delannée, C., and Delaboudinière, J.-P. (2000). Coronal dimmings and energetic CMEs in April-May 1998. *Geophys. Res. Lett.*, 27:1431–1434.

Thompson, M. J., Toomre, J., Anderson, E. R., Antia, H. M., Berthomieu, G., Burtonclay, D., Chitre, S. M., Christensen-Dalsgaard, J., Corbard, T., De Rosa, M., Genovese, C. R., Gough, D. O., Haber, D. A., Harvey, J. W., Hill, F., Howe, R., Korzennik, S. G., Kosovichev, A. G., Leibacher, J. W., Pijpers, F. P., Provost, J., Rhodes, E. J., J., Schou, J., Sekii, T., Stark, P. B., and Wilson, P. R. (1996). Differential Rotation and Dynamics of the Solar Interior. *Science*, 272(5266):1300–1305.

Titov, V. S. and Démoulin, P. (1999). Basic topology of twisted magnetic configurations in solar flares. *Astron. Astrophys.*, 351:707–720.

Török, T., Downs, C., Linker, J. A., Lionello, R., Titov, V. S., Mikić, Z., Riley, P., Caplan, R. M., and Wijaya, J. (2018). Sun-to-Earth MHD Simulation of the 2000 July 14 "Bastille Day" Eruption. *Astrophys. J.*, 856:75.

Török, T. and Kliem, B. (2005). Confined and Ejective Eruptions of Kink-unstable Flux Ropes. *Astrophys. J.*, 630:L97–L100.

Török, T., Kliem, B., and Titov, V. S. (2004). Ideal kink instability of a magnetic loop equilibrium. *Astron. Astrophys.*, 413:L27–L30.

Török, T., Panasenco, O., Titov, V. S., Mikić, Z., Reeves, K. K., Velli, M., Linker, J. A., and De Toma, G. (2011). A Model for Magnetically Coupled Sympathetic Eruptions. *Astrophys. J.*, 739:L63.

Tsurutani, B. T., Smith, E. J., Gonzalez, W. D., Tang, F., and Akasofu, S. I. (1988). Origin of interplanetary southward magnetic fields responsible for major magnetic storms near solar maximum (1978-1979). *J. Geophys. Res.*, 93:8519–8531.

van Ballegooijen, A. A. and Martens, P. C. H. (1989). Formation and Eruption of Solar Prominences. *Astrophys. J.*, 343:971.

van Driel-Gesztelyi, L. and Green, L. M. (2015). Evolution of Active Regions. *Living Rev. Sol. Phys.*, 12:1.

Verbeke, C., Pomoell, J., and Poedts, S. (2019). The evolution of coronal mass ejections in the inner heliosphere: implementing the spheromak model with euhforia. *Astron. Astrophys.*, in press.

Vourlidas, A. (2015). Mission to the Sun-Earth L_5 Lagrangian Point: An Optimal Platform for Space Weather Research. *Space Weather*, 13:197–201.

Vourlidas, A., Balmaceda, L. A., Stenborg, G., and Dal Lago, A. (2017). Multi-viewpoint

Coronal Mass Ejection Catalog Based on STEREO COR2 Observations. *Astrophys. J.*, 838:141.

Vourlidas, A., Colaninno, R., Nieves-Chinchilla, T., and Stenborg, G. (2011). The First Observation of a Rapidly Rotating Coronal Mass Ejection in the Middle Corona. *Astrophys. J. Lett.*, 733:L23.

Vourlidas, A., Howard, R. A., Esfandiari, E., Patsourakos, S., Yashiro, S., and Michalek, G. (2010). Comprehensive Analysis of Coronal Mass Ejection Mass and Energy Properties Over a Full Solar Cycle. *Astrophys. J.*, 722:1522–1538.

Vourlidas, A., Lynch, B. J., Howard, R. A., and Li, Y. (2013). How Many CMEs Have Flux Ropes? Deciphering the Signatures of Shocks, Flux Ropes, and Prominences in Coronagraph Observations of CMEs. *Solar Phys.*, 284:179–201.

Vourlidas, A., Wu, S. T., Wang, A. H., Subramanian, P., and Howard, R. A. (2003). Direct Detection of a Coronal Mass Ejection-Associated Shock in Large Angle and Spectrometric Coronagraph Experiment White-Light Images. *Astrophys. J.*, 598(2):1392–1402.

Vršnak, B. and Cliver, E. W. (2008). Origin of Coronal Shock Waves. Invited Review. *Solar Phys.*, 253:215–235.

Vršnak, B., Žic, T., Vrbanec, D., Temmer, M., Rollett, T., Möstl, C., Veronig, A., Čalogović, J., Dumbović, M., Lulić, S., Moon, Y. J., and Shanmugaraju, A. (2013). Propagation of Interplanetary Coronal Mass Ejections: The Drag-Based Model. *Solar Phys.*, 285:295–315.

Wang, Y., Wang, B., Shen, C., Shen, F., and Lugaz, N. (2014). Deflected propagation of a coronal mass ejection from the corona to interplanetary space. *J. Geophys. Res. Space Physics*, 119:5117–5132.

Wang, Y. M., Sheeley, N. R., J., and Rich, N. B. (2007). Coronal Pseudostreamers. *Astrophys. J.*, 658(2):1340–1348.

Wang, Y. M., Sheeley, N. R., Socker, D. G., Howard, R. A., and Rich, N. B. (2000). The dynamical nature of coronal streamers. *J. Geophys. Res.*, 105(A11):25133–25142.

Webb, D. F. and Howard, R. A. (1994). The solar cycle variation of coronal mass ejections and the solar wind mass flux. *J. Geophys. Res.*, 99(A3):4201–4220.

Webb, D. F. and Howard, T. A. (2012). Coronal Mass Ejections: Observations. *Living Rev. Sol. Phys.*, 9(1):3.

Welsch, B. T. (2018). Flux Accretion and Coronal Mass Ejection Dynamics. *Solar Phys.*, 293(7):113.

Wiegelmann, T. (2008). Nonlinear force-free modeling of the solar coronal magnetic field. *J. Geophys. Res.*, 113(A3):A03S02.

Wiegelmann, T., Petrie, G. J. D., and Riley, P. (2017). Coronal Magnetic Field Models. *Space Sci. Rev.*, 210(1-4):249–274.

Witasse, O., Sánchez-Cano, B., Mays, M. L., Kajdič, P., Opgenoorth, H., Elliott, H. A., Richardson, I. G., Zouganelis, I., Zender, J., Wimmer-Schweingruber, R. F., Turc, L.,

Taylor, M. G. G. T., Roussos, E., Rouillard, A., Richter, I., Richardson, J. D., Ramstad, R., Provan, G., Posner, A., Plaut, J. J., Odstrcil, D., Nilsson, H., Niemenen, P., Milan, S. E., Mandt, K., Lohf, H., Lester, M., Lebreton, J.-P., Kuulkers, E., Krupp, N., Koenders, C., James, M. K., Intzekara, D., Holmstrom, M., Hassler, D. M., Hall, B. E. S., Guo, J., Goldstein, R., Goetz, C., Glassmeier, K. H., Génot, V., Evans, H., Espley, J., Edberg, N. J. T., Dougherty, M., Cowley, S. W. H., Burch, J., Behar, E., Barabash, S., Andrews, D. J., and Altobelli, N. (2017). Interplanetary coronal mass ejection observed at STEREO-A, Mars, comet 67P/Churyumov-Gerasimenko, Saturn, and New Horizons en route to Pluto: Comparison of its Forbush decreases at 1.4, 3.1, and 9.9 AU. *J. Geophys. Res. Space Physics*, 122:7865–7890.

Wold, A. M., Mays, M. L., Taktakishvili, A. r., Jian, L. K., Odstrcil, D., and MacNeice, P. (2018). Verification of real-time WSA-ENLIL+Cone simulations of CME arrival-time at the CCMC from 2010 to 2016. *J. Space Weather Space Clim.*, 8:A17.

Woltjer, L. (1958). A Theorem on Force-Free Magnetic Fields. *Proceedings of the National Academy of Science*, 44:489–491.

Wood, B. E., Wu, C. C., Rouillard, A. P., Howard, R. A., and Socker, D. G. (2012). A Coronal Hole's Effects on Coronal Mass Ejection Shock Morphology in the Inner Heliosphere. *Astrophys. J.*, 755:43.

Yashiro, S., Gopalswamy, N., Michalek, G., St. Cyr, O. C., Plunkett, S. P., Rich, N. B., and Howard, R. A. (2004). A catalog of white light coronal mass ejections observed by the SOHO spacecraft. *J. Geophys. Res.*, 109:A07105.

Yurchyshyn, V. (2008). Relationship between EIT Posteruption Arcades, Coronal Mass Ejections, the Coronal Neutral Line, and Magnetic Clouds. *Astrophys. J. Lett.*, 675:L49.

Yurchyshyn, V., Yashiro, S., Abramenko, V., Wang, H., and Gopalswamy, N. (2005). Statistical Distributions of Speeds of Coronal Mass Ejections. *Astrophys. J.*, 619:599–603.

Zhang, J., Richardson, I. G., Webb, D. F., Gopalswamy, N., Huttunen, E., Kasper, J. C., Nitta, N. V., Poomvises, W., Thompson, B. J., Wu, C. C., Yashiro, S., and Zhukov, A. N. (2007). Solar and interplanetary sources of major geomagnetic storms (Dst $\leq$ -100 nT) during 1996-2005. *J. Geophys. Res.*, 112:A10102.

Zirker, J. B. (1977). Coronal holes and high-speed wind streams. *Rev. Geophys. Space Phys.*, 15:257–269.